# Multi-scale FEM-DEM model for granular materials : micro-scale boundary conditions, statics and dynamics

***Citation for published version (APA):***
Liu, J. (2018). *Multi-scale FEM-DEM model for granular materials : micro-scale boundary conditions, statics and dynamics*. [Phd Thesis 1 (Research TU/e / Graduation TU/e), Built Environment]. Technische Universiteit Eindhoven.

***Document status and date:***
Published: 20/12/2018

***Document Version:***
Publisher’s PDF, also known as Version of Record (includes final page, issue and volume numbers)

***Please check the document version of this publication:***

• A submitted manuscript is the version of the article upon submission and before peer-review. There can be important differences between the submitted version and the official published version of record. People interested in the research are advised to contact the author for the final version of the publication, or visit the DOI to the publisher's website.
• The final author version and the galley proof are versions of the publication after peer review.
• The final published version features the final layout of the paper including the volume, issue and page numbers.

Link to publication

***General rights***
Copyright and moral rights for the publications made accessible in the public portal are retained by the authors and/or other copyright owners and it is a condition of accessing publications that users recognise and abide by the legal requirements associated with these rights.

- Users may download and print one copy of any publication from the public portal for the purpose of private study or research.
- You may not further distribute the material or use it for any profit-making activity or commercial gain
- You may freely distribute the URL identifying the publication in the public portal.

If the publication is distributed under the terms of Article 25fa of the Dutch Copyright Act, indicated by the “Taverne” license above, please follow below link for the End User Agreement:

www.tue.nl/taverne

***Take down policy***
If you believe that this document breaches copyright please contact us at:

openaccess@tue.nl

providing details and we will investigate your claim.

Download date: 05. Oct. 2023

# Multi-scale FEM-DEM Model for Granular Materials:
## Micro-scale boundary conditions, Statics and Dynamics

PROEFSCHRIFT

ter verkrijging van de graad van doctor aan de Technische Universiteit Eindhoven, op
gezag van de rector magnificus, prof.dr.ir. F.P.T. Baaijens, voor een commissie
aangewezen door het College voor Promoties in het openbaar te verdedigen op
donderdag 20 december 2018 om 11:00 uur

door

**Jiadun Liu**

geboren te Shandong, China

Dit proefschrift is goedgekeurd door de promotoren en de samenstelling van de promotiecommissie is als volgt:

| | |
|---|---|
| voorzitter: | prof.ir. E.S.M. Nelissen |
| promotor: | prof.dr.ir. A.S.J. Suiker |
| co-promotor: | dr.ir. E. Bosco |
| leden: | prof.dr.rer.-nat. S. Luding (Universiteit Twente) |
| | prof.dr.ir. L.J. Sluys (Technische Universiteit Delft) |
| | prof.dr.ir. T.A.M. Salet |
| | prof.dr. M.A. Hicks (Technische Universiteit Delft) |
| | dr.ir. V. Kouznetsova |

# Multi-scale FEM-DEM Model for Granular Materials:
## Micro-scale boundary conditions, Statics and Dynamics

A catalogue record is available from the Eindhoven University of Technology Library

ISBN 978-90-386-4621-3
NUR 929

Cover design by Jiadun Liu

Printed by the Eindhoven University Press, Eindhoven, The Netherlands
Published as issue 254 in de Bouwstenen series of the faculty of Built Environment
of the Eindhoven University of Technology

To my parents

# Acknowledgements

Almost five years have past since I started my PhD journey on the 3rd of September 2013. In retrospect, I have enjoyed this journey despite the many difficulties I met. The reasons are as follows. When there were obstacles in my research, there was guidance, encouragement and help from many individuals. These contributions were of crucial importance for the completion of my PhD.

First of all, I would like to express my sincere gratitude to my supervisor, Prof. Akke Suiker, for giving me a chance to study under his supervision. He always gave me proper advice on what to study and how to study. I still remember that after our first meeting in the morning of 4th September 2013, he suggested me to read two relevant papers: lecture notes on continuum mechanics and a book chapter on nonlinear continuum mechanics. When I found out it was not easy to prepare a periodic random packing, he referred me to a paper that mentions a proper method to solve this problem, etc. The research skills I learned from him have benefited me and will continue to benefit me in my future career.

I would also like to gratefully acknowledge my co-supervisor, Dr. Emanuela Bosco, for helping me to solve many problems in my research. Without the direct and indirect help from her, I would never have completed my PhD.

In addition, I would like to thank Dr. Ning Guo (Carleton University, Ottawa, Canada) and Dr. Lutz Gross (University of Queensland, Brisbane, Australia) for the fruitful discussions on the use of ESyS-Escript. I am also grateful to Prof. Stefan Luding (University of Twente, Netherlands) for the useful interactions on DEM modeling. I appreciate the feedback provided by Dr. Steffen Abe (Institute for Geothermal Resources Managment, Mainz, Germany), by Dr. Dion Weatherley (University of Queensland, Brisbane, Australia) and by Joran Jessurun (Eindhoven University of Technology, Netherlands) on numerical implementation issues within the ESyS-Particle code.

The Netherlands Organization for Scientific Research (NWO) is acknowledged for providing access to the supercomputer facilities; the multi-scale simulations were performed under NWO-Project 15421 and NWO-Project 16345 *Multi-scale*

*modeling of granular materials*, within the funding scheme.

The financial support provided by the China Scholarship Council (CSC) is gratefully acknowledged. Regarding this aspect, I would like to direct my heartfelt thanks to Prof. Hongwei Zhou for his support in my application for the CSC scholarship when I was a first-year PhD student in his research group. I am very grateful to Jie Qin and Hu Jiang for their trust in my ability to perform a PhD study in the Netherlands.

I would like to direct my sincere thanks to my friends for their company and understanding. The times that we traveled, went to the sports center, or celebrated festivals, will reside in my mind forever.

Finally, I would like to thank my parents, my sister and my brother-in-law for their encouragement and support.

# Summary

Granular materials are abundantly present in nature and engineering. Their mechanical behavior at the macroscopic scale is determined by the deformation and failure mechanisms occurring at the particle scale. Such coupling effects are accounted for in the hierarchical multi-scale FEM-DEM framework developed in this thesis work. The modeling framework may be used to study the effects of mechanical and geometrical properties at the particle scale on the macroscopic response of granular materials subjected to arbitrary loading conditions. Accordingly, the three main aims of this thesis are: (1) to provide novel algorithms for the implementation of micro-scale boundary conditions required for numerical homogenization using finite deformation theory, (2) to incorporate the novel numerical algorithm in a multi-scale FEM-DEM framework, and use this framework for analyzing the influence of micro-structural characteristics on the quasi-static, macroscopic response of large-scale granular structures, and (3) to apply the homogenization framework to dynamic problems, whereby the effects of wave dispersion, the type of contact model and the packing polydispersity on the multi-scale dynamic response are explored.

Firstly, a servo-control methodology is adopted to establish numerical algorithms for the three types of classical, micro-scale boundary conditions, which are: (1) a homogeneous deformation and zero particle rotation (D), (2) a periodic particle displacement and rotation (P), and (3) a uniform particle force and free particle rotation (T). The algorithms can be straightforwardly combined with commercially available discrete element codes, thereby enabling the determination of the solution of boundary-value problems at the micro-scale only, or at multiple scales via a micro-to-macro coupling with a finite element model. The performance of the algorithms is tested by means of discrete element method simulations on regular monodisperse packings and irregular polydisperse packings composed of frictional particles, which were subjected to various loading paths. Subsequently, a homogenization framework is derived for the implementation of mixed (D)-(P)-(T) boundary conditions that satisfy the Hill-Mandel micro-

heterogeneity condition on energy consistency at the micro- and macro-scales of the granular system. The numerical algorithm for the mixed boundary conditions is developed and tested for the case of an infinite layer subjected to a vertical compressive stress and a horizontal shear deformation, whereby the response computed for a layer of cohesive particles is compared against that for a layer of frictional particles.

Secondly, a hierarchical multi-scale model for the analysis of granular systems is proposed, which combines the principles of a coupled FEM-DEM approach with the novel servo-control methodology for the implementation of appropriate micro-scale boundary conditions. A mesh convergence study is performed, whereby the results of a quasi-static biaxial compression test are compared with those obtained by direct numerical simulations. The comparison demonstrates the capability of the multi-scale method to realistically capture the macro-scale response, even for macroscopic domains characterized by a relatively coarse mesh; this makes it possible to accurately analyze large-scale granular systems in a computationally efficient manner. The multi-scale framework is applied to study in a systematic manner the role of individual micro-structural characteristics on the effective macro-scale response. The effect of particle contact friction, particle rotation, and initial fabric anisotropy on the overall response is considered, as measured in terms of the evolution of the effective stress, the volumetric deformation, the average coordination number and the induced anisotropy. The trends observed are in accordance with notions from physics, and observations from experiments and other DEM simulations presented in the literature.

Finally, the applicability and limitations of the first-order hierarchical multi-scale framework are studied for dynamic wave propagation problems in granular materials. The study considers the effects on the response by regular and polydisperse packings, wave dispersion, the type of particle contact law, and the size of the representative volume used at the micro scale. The numerical results obtained by the coupled FEM-DEM framework are compared against those following from direct numerical simulations (DEM), which provides detailed information on the applicability of the multi-scale framework.

# Contents

# List of Figures

# List of Tables

# Chapter 1

# Introduction

## 1.1 Scales of observation for granular materials

The development of adequate models for simulating the mechanical behavior of granular materials, such as sand, clay and peat, is important for many geotechnical applications in building, civil, mining and petroleum engineering. Examples of such applications are the design of foundations for buildings, bridges, roads and railroads, the stability of slopes, deposits, reservoirs, excavations and boreholes, the construction of drainage systems and irrigation systems, and the design of buildings and other large engineering structures against earthquakes. A study of the mechanical behavior of granular materials may be performed at different levels of observation. Firstly, there is the micro-level, at which the individual grains are identified and modeled as separate discrete objects, experiencing displacements and rotations as a result of contact force and contact moment interactions with neighboring grains. Secondly, there is the macro-level (or engineering level), at which no internal material structure can be recognized anymore, and the granular material behaves as a continuum. The effective constitutive behavior at this level of observation is described by a stress-strain relationship, which, in the classical sense, assumes the material to respond homogeneously. Although the distinction between the above two levels of observation is unequivocal, the transition from the micro-scale to the macro-scale is far from abrupt. In fact, there is a large class of problems for which the specific discrete, micro-level behavior may lead to a heterogeneous material response at the macro-level. The heterogeneities may originate from strong *time variations* in the displacement/rotation fields characterizing the micro-scale response, i.e., high-frequency wave propagation with wavelengths in the order of as small as only a few times the particle size, or by strong *spatial variations* in the response, i.e. shear failure, rupture, faulting and local particle crushing across localized bands of a width equal to a few times the particle size. Discrete models indeed have the potential to describe such phenomena in an accurate fashion, see e.g., (Herrmann and Luding, 1998; Kun and Herrmann, 1996; Ting et al., 1993; Borja and Wren, 1995; Suiker and Fleck, 2004; Luding, 2004; Luding and Suiker, 2008; Singh et al., 2014; Potyondy and Cundall, 2004; Wellmann et al., 2008), but their applicability to large-scale engineering problems is prohibitory expensive due to the enormous computational costs involved when simulating the response of each particle individually. To circumvent this problem, multi-scale techniques have been developed (Kaneko et al., 2003; Meier et al., 2008; Miehe et al., 2010; Nguyen et al., 2013; Li et al., 2010a,b, 2011, 2014; Guo and Zhao, 2014; Liu et al., 2016), where the mechanical responses at small and large length scales are efficiently combined in a consistent manner. In a two-scale approach, which distinguishes between the macro and micro scales, $l_k$ can be defined as the characteristic length of a micro-scale heterogeneity, which for granular materials typically may be in the order of $10$ to $20$ times the average grain size, and $L$ is a macroscopic length scale, reflecting the size of the macroscopic granular sample or a wavelength in the macroscopic deformation field. If the difference between the micro and macro length scales is an order of magnitude or more, i.e.,

$$l_k \ll L \qquad \forall k = 1, 2, ..., N \tag{1.1}$$

where $N$ is the total number of micro-scale heterogeneities in the macroscopic volume, then the scales may be assumed to be separated, allowing for the application of a *first-order (or classical) homogenization scheme*. With the assumption given by Eq.(1.1), which covers a wide range of practical situations, the influences of boundary-layer effects and other localized phenomena may be assumed small, and therefore are ignored. For example, in the work of (Miehe et al., 2010), a hierarchical *computational homogenization framework* for granular materials subjected to the requirement given by Eq.(1.1) was proposed for three types of boundary conditions, namely *i)* linear displacements (D), *ii)* uniform stress (T), and *iii)* periodic boundary conditions (P). Basic ingredients and concepts for such a multi-scale approach can be found in earlier works by (Suquet, 1985; Guedes and Kikuchi, 1990; Ghosh et al., 1995, 1996; Miehe et al., 1999a,b; Miehe and Bayreuther, 2007) for composite materials. The homogenization framework of (Miehe et al., 2010) simulates frictional contact interactions between particles by means of a Coulomb-type contact law, and accounts for finite deformations by using the macroscopic deformation gradient $\bar{\boldsymbol{F}}$ as the governing parameter in the formulation of the boundary conditions at the micro scale. Accordingly, a deformation-driven, non-linear, computational homogenization framework is established, whereby the *macro-scale*, engineering problem is simulated by means of the Finite Element Method (FEM), and the micro-scale behaviour of the particle assembly is simulated with the Discrete Element Method (DEM). At each material point at the macro scale, the solution of the micro-scale boundary value problem following from the application of the corresponding deformation gradient $\bar{\boldsymbol{F}}$ provides the updated *micro-scale particle forces and positions*. This information can

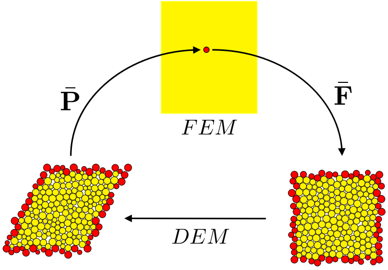

**Figure 1.1:** Computational homogenization scheme for granular materials

be used to compute the effective material stress $\bar{\boldsymbol{P}}$ (i.e., the $1^{st}$ Piola-Kirchhoff stress), see Figure 1.1. Hence, with this approach it is not necessary to explicitly formulate a (phenomenological) constitutive law between the stress $\bar{\boldsymbol{P}}$ and the deformation gradient $\bar{\boldsymbol{F}}$ at the macro scale, as is commonly done in (single-scale) finite element models; instead, the constitutive behavior of the granular assembly automatically follows from computing the average stress $\bar{\boldsymbol{P}}$ after subjecting the discrete granular microstructure to a specific deformation gradient $\bar{\boldsymbol{F}}$ by means of appropriate (D, P or S) boundary conditions. In contrast to *analytical homogenisation schemes*, such as the asymptotic homogenization scheme (Bensoussan et al., 1978; Torquato, 2002), homogenization schemes based on Hashin-Shtrikman variational principles (Hashin and Shtrikman, 1963; Willis, 1981), or the so-called microstructural approach for granular materials (Chang and Gao, 1995, 1997; Suiker et al., 2001a,b; Suiker and de Borst, 2005), the above *computational* homogenization scheme allows for the simulation of complex path-dependent, non-linear material responses of evolving granular microstructures subjected to arbitrary loading paths.

## 1.2 Types of computational homogenization

Computational homogenization may be generally classified into two categories, i.e. the *hierarchical methods*, of which the model of (Miehe et al., 2010) discussed above is an illustrative example, and the *concurrent methods*. The differences between the two methods are illustrated below by highlighting several features, and indicating some practical applications.

### 1.2.1 Concurrent methods

In concurrent methods the model domain is decomposed into two parts. A DEM model is used for simulating the part in which the deformation varies substantially, and is strongly characterized by the micro-scale features of the particle packing. The other, remaining part of the domain is simulated by a FEM model, in which the deformation varies mildly and can be characterized by average, macro-scale quantities (Frangin et al., 2006; Rojek and Oñate, 2007; Wellmann and Wriggers, 2012; Li and Wan, 2011; Wagner and Liu, 2003; Xiao and Belytschko, 2004). Accordingly, an important challenge in concurrent methods is to properly couple the kinematic and kinetic conditions at the interface between the FEM and DEM domains. In (Frangin et al., 2006) this was done by adopting a linear combination of discrete and continuum Hamiltonians at the FEM-DEM interface. The constraints at the interface can be implemented by using Lagrange multipliers or penalty functions (Rojek and Oñate, 2007). Additionally, the Arlequin method has been suggested for this purpose, which uses reliable energy partition functions and coupling operators to concurrently connect the FEM and DEM models within a coupling zone (Wellmann and Wriggers, 2012). Another approach is the so-called bridging scale technique, whereby the coarse and fine scales are simulated with FEM and DEM, respectively, and high frequency waves emitted from the fine scale are eliminated by means of lattice impedance techniques (Frangin et al., 2006; Li and Wan, 2011).

### 1.2.2 Hierarchical methods

As already indicated above, in hierarchical methods the macro-scale problem is simulated over the *whole domain* by using FEM, whereby at each material point (or integration point) the effective stress response due to the imposed deformation is obtained as a volume average over a representative granular packing modeled by DEM. When an implicit time integration scheme is used at the macro-scale, in addition to the effective stress, the effective tangential stiffness of the granular packing needs to be computed. In the following, some representative works of hierarchical methods are briefly summarized. A small-strain, first-order homogenization scheme for granular materials was proposed in (Kaneko et al., 2003) to simulate a biaxial compression test for frictional granular materials and a bending test for cohesive granular materials. A slope stability problem was analyzed in (Meier et al., 2008) by applying a hierarchical scheme based upon imposing affine deformation on the representative DEM sample, whereby the effective tangent operator required for the implicit update scheme adopted was determined in an analytical fashion. In (Nitka et al., 2011) a perturbation method was used to numerically calculate the tangent operator. The relation between the arrangement of RVEs at the different Gauss points and the emergence of shear bands was analyzed in (Shahin et al., 2016). Biaxial compression and cyclic shear were studied in (Guo and Zhao, 2014) by using a hierarchical multi-scale method whereby periodic boundary conditions were applied on the representative DEM sample and the constitutive tangent operator was computed analytically. Multi-scale effects of inherent anisotropy in granular packings and macro-scale boundary conditions on the formation of shear bands were explored in (Zhao and Guo, 2015). Other problems examined in a multi-scale fashion are retaining wall and footing problem (Guo and Zhao, 2016b), shear failure of thick-walled hollow cylinder in dry sand (Guo et al., 2016), triaxial compression and extension tests on cubical and cylindrical specimens (Guo and Zhao, 2016a), and compaction bands in high-porosity sandstones (Wu et al., 2018a), and borehole instabilities in high-porosity sandstones (Wu et al., 2018b).

The use of enhanced methods to avoid mesh-dependency during strain localization has been explored in multi-scale approaches based on a nonlocal strain formulation (Liu et al., 2016), a second-gradient formulation (Desrues et al., 2017), and micro-polar (e.g., Cosserat) continuum models (Li et al., 2010a, 2011, 2010b, 2014). For more extensive reviews on hierarchical FEM-DEM modeling of granular materials the reader is referred to (Li et al., 2016; Zhao, 2017).

## 1.3 Objectives and Scope

Specific aspects that deserve more attention in hierarchical FEM-DEM homogenization methods, but often are neglected for reasons of simplicity, refer to (1) the Hill-Mandel micro-heterogeneity condition, which enforces consistency of energy at the micro- and macro-scales, (2) the effect of particle rotations in the formulation of micro-to-macro scale-transitions, and (3) a rigorous generalization of the multi-scale approach within the theory of large deformations. The computational homogenization framework presented in (Miehe et al., 2010) does include the three aspects mentioned above, and calculates the micro-scale response of a granular packing with a DEM model equipped with a frame of boundary particles at which the finite deformation following from the macro-scale is imposed. However, the numerical implementation of the micro-scale boundary conditions in (Miehe et al., 2010) is done via a penalty method, where the violation of the boundary conditions is punished by increasing the total virtual work of the particle packing, through the introduction of additional forces and moments on the frame of boundary particles. Due to the nature of the penalty method the expression for the homogenized stress of the particle packing becomes explicitly dependent on the value of the penalty parameter, and thereby looses its physical interpretation. In addition, in DEM models the penalty parameter may be difficult to control and must be chosen sufficiently large in order for the penalty function to be effective, which may induce numerical instabilities (Dussault, 1995; Gunaratne and Wu, 2011). Another characteristic of the penalty method is that it requires the constraint equations to be satisfied approximately instead of exactly, whereby the accuracy of the approximation is determined by the magnitude of the penalty parameter. As a consequence, the limit case at which the boundary conditions are met exactly is not rigorously retrieved from the formulation, since the homogenized stress of the particle packing then vanishes, see expression (44) in (Miehe et al., 2010).

In order to improve on the algorithmic drawbacks mentioned above, the first aim of this thesis work is to develop an alternative numerical algorithm for the implementation of the homogenization framework presented in (Miehe et al., 2010). This algorithm is based on a servo-control methodology, using a feedback principle comparable to that of algorithms commonly applied within control theory of dynamic systems (Åström and Murray, 2008). A strong point of this approach is that it is relatively simple to implement, and only affects the interface communicating information between the macro-scale FEM and micro-scale DEM models. In addition to its simplicity, the servo-control algorithm preserves the physical interpretation of the homogenized stress measure derived for the particle packing, and furnishes a realistic value for the stress in the limit case at which the micro-scale boundary condition is met exactly. The second aim of this thesis work is to incorporate the novel numerical algorithm in a multi-scale FEM-DEM framework, and use this framework for analyzing the influence of micro-structural characteristics (e.g., particle contact friction, particle rotation, initial fabric anisotropy) on the quasi-static, macroscopic response of large-scale granular structures. In addition, the potential of the framework for applications related to dynamic loading need to be explored, whereby the effects by wave dispersion, the type of contact model and the packing polydispersity on the multi-scale dynamic response must be clarified. An adequate way of doing this is to critically compare the results of the FEM-DEM multi-scale analyses to those obtained by direct numerical simulations (DEM); for some reasons such a comparison is regularly lacking in other works on hierarchical computational homogenization of granular materials.

## 1.4 Outline

The outline of this thesis is as follows. Chapter 2 presents a review of the numerical homogenization framework for particle aggregates, and outlines the formulations of the micro-scale (D), (P) and (T) boundary conditions proposed in (Miehe et al., 2010). The numerical implementation of the micro-scale boundary conditions is discussed, where for the (P) and (T) boundary conditions two different servo-control algorithms are presented, which include or not an initial prediction of the displacements of the boundary particles based on their positions calculated at the previous loading step. Subsequently, the performance of the numerical algorithms is tested on monodisperse and polydisperse frictional packings subjected to various loading paths. Additionally, a formulation for mixed boundary conditions is provided, and its numerical performance is demonstrated for the cases of infinite frictional and cohesive granular layers loaded by a vertical compressive stress, and subsequently subjected to a horizontal shear deformation.

Chapter 3 presents the numerical homogenization framework for particle aggregates by defining the macro-scale and micro-scale models and the scale transition relations. Numerical implementation aspects are discussed, and the explicit time integration scheme adopted for the macro-scale problem is outlined. Furthermore, details are provided on the dynamic relaxation procedure applied for satisfying the equilibrium conditions, and on the servo-control algorithm used for defining the boundary conditions at the micro scale. The coupled FEM-DEM solution algorithm is presented, and its accuracy is explored by simulating a biaxial compression test and comparing the computational results to those obtained by direct numerical simulations. A mesh convergence study is performed, and the role of several micro-structural parameters on the macroscopic response is studied.

In Chapter 4 the applicability and limitations of the first-order hierarchical multi-scale framework are studied for dynamic wave propagation problems in granular materials. The study considers the effects on the response by regular and polydisperse packings, wave dispersion, the type of particle contact law, and the size of the representative volume used at the micro scale. The numerical results obtained by the coupled FEM-DEM framework are compared against those following from direct numerical simulations (DEM), which provides detailed information on the applicability of the multi-scale framework.

Finally, in Chapter 5 the main conclusions of the thesis work are summarized, and some recommendations for future research on the hierarchical, multi-scale modelling of granular materials are provided.

# Chapter 2

# Micro-scale boundary conditions[1]

Novel numerical algorithms are presented for the implementation of micro-scale boundary conditions of particle aggregates modelled with the discrete element method. The algorithms are based on a servo-control methodology, using a feedback principle comparable to that of algorithms commonly applied within the control theory of dynamic systems. The boundary conditions are defined in accordance with the large deformation theory, and are imposed on a frame of boundary particles surrounding the interior granular micro-structure. Following the formulation presented in Miehe et al., (2010), *Int. J. Num. Meth. Engng.* **83**, pp. 1206-1236, first three types of classical boundary conditions are considered, in accordance with i) a homogeneous deformation and zero particle rotation (D), ii) a periodic particle displacement and rotation (P), and iii) a uniform particle force and free particle rotation (T). The algorithms can be straightforwardly combined with commercially available discrete element codes, thereby enabling the determination of the solution of boundary-value problems at the micro-scale only, or at multiple scales via a micro-to-macro coupling with a finite element model. The performance of the algorithms is tested by means of discrete element method simulations on regular monodisperse packings and irregular polydisperse packings composed of frictional particles, which were subjected to various loading paths. The simulations provide responses with the typical stiff and soft bounds for the (D) and (T) boundary conditions, respectively, and illustrate for the (P) boundary condition a relatively fast convergence of the apparent macroscopic properties under an increasing packing size. Finally, a homogenization framework

---

[1] Based on Liu, J., Bosco, E. and Suiker, A.S.J. , 2017. Formulation and numerical implementation of micro-scale boundary conditions for particle aggregates. Granular Matter, 19(4), 72.

is derived for the implementation of mixed (D)-(P)-(T) boundary conditions that satisfy the Hill-Mandel micro-heterogeneity condition on energy consistency at the micro- and macro-scales of the granular system. The numerical algorithm for the mixed boundary conditions is developed and tested for the case of an infinite layer subjected to a vertical compressive stress and a horizontal shear deformation, whereby the response computed for a layer of cohesive particles is compared against that for a layer of frictional particles.

## 2.1 Introduction

The accurate computation of the non-linear failure and deformation behavior of heterogeneous granular systems commonly requires a resolution of the complex mechanical interactions and deformation mechanisms at the particle scale, which can be adequately accounted for by using the discrete element method (DEM), see e.g., (Cundall and Strack, 1979; Herrmann and Luding, 1998; Kun and Herrmann, 1996; Ting et al., 1993; Borja and Wren, 1995; Suiker and Fleck, 2004; Luding, 2004; Luding and Suiker, 2008; Wellmann et al., 2008; Guo and Zhao, 2013; Singh et al., 2014; Nitka and Tejchman, 2015; Zhu et al., 2016; Huang et al., 2017; Zhao et al., 2018) and references therein. For practical granular systems composed of a vast number of particles, however, it is infeasible to simulate each particle as an individual discrete object, since this leads to DEM models with an enormously large number of degrees of freedom, and consequently, to impractical computation times. To circumvent this problem, advanced multi-scale frameworks have been developed, where the mechanical responses at the particle micro-scale and the structural macro-scale are hierarchically coupled in an computationally economical fashion. This is accomplished by simulating the macro-scale problem under consideration with the finite element method (FEM), whereby in every integration point the response to the corresponding deformation is calculated by means of a DEM model that accurately and efficiently represents the complex particle behavior at the micro-scale. Examples of coupled FEM-DEM approaches for granular materials can be found in (Kaneko et al., 2003; Nguyen et al., 2013; Guo and Zhao, 2014; Shahin et al., 2016; Guo and Zhao, 2016b; Wu et al., 2018a,b; Li et al., 2010a, 2011, 2010b, 2014), illustrating the use of various averaging theorems for relating force and displacement measures at the particle micro-scale to stress and strain measures at the structural macro-scale. Specific aspects that should deserve more attention in FEM-DEM homogenization methods, but often are neglected for reasons of simplicity, refer to i) the Hill-Mandel micro-heterogeneity condition, which enforces consistency of energy at the micro- and macro-scales, ii) the effect of particle rotations in the formulation of micro-to-macro scale-transitions, and iii) a rigorous generalization of the multi-scale approach within the theory of large deformations.

The computational homogenization framework presented in (Miehe et al., 2010) does include the three aspects mentioned above, and calculates the micro-scale response of a granular packing with a DEM model equipped with a frame of boundary particles at which the finite deformation following from the macro-scale is imposed. The formulation considers three types of micro-scale boundary conditions for the boundary particles, namely i) homogeneous deformation and zero particle rotation (D), ii) periodic particle displacements and rotations (P), and iii) uniform particle force and free particle rotation (T), where the abbreviations (D), (P) and (T) are adopted from analogous, classical boundary conditions used in continuum homogenization theories, referring to the displacement, periodic and traction boundary conditions, respectively. The numerical implementation of the boundary conditions in (Miehe et al., 2010) is done via a penalty method, where the violation of the boundary conditions is punished by increasing the total virtual work of the particle packing, through the introduction of additional forces and moments on the frame of boundary particles. Although the algorithm presented in (Miehe et al., 2010) has been nicely generalized for the three types of boundary conditions in a mathematically elegant and transparent fashion, due to the nature of the penalty method the expression for the homogenized stress of the particle packing becomes explicitly dependent on the value of the penalty parameter, and thereby looses its physical interpretation. In addition, in DEM models the penalty parameter may be difficult to control and must be chosen sufficiently large in order for the penalty function to be effective, which may induce numerical instabilities (Dussault, 1995; Gunaratne and Wu, 2011). Another characteristic of the penalty method is that it requires the constraint equations to be satisfied “approximately” instead of “exactly”, whereby the accuracy of the approximation is determined by the magnitude of the penalty parameter. As a consequence, the limit case at which the boundary conditions are met exactly is not rigorously retrieved from the formulation, since the homogenized stress of the particle packing then vanishes, see expression (44) in (Miehe et al., 2010).

In order to improve on the algorithmic drawbacks mentioned above, in this chapter an alternative numerical algorithm is proposed for the implementation of the homogenization framework presented in (Miehe et al., 2010). This algorithm is based on a servo-control methodology, using a feedback principle comparable to that of algorithms commonly applied within control theory of dynamic systems (Åström and Murray, 2008). Accordingly, the displacements and rotations of the particles of the boundary frame are iteratively adapted from a gradually diminishing discrepancy between the measured and desired values of the micro-scale boundary condition. A strong point of this approach is that it is relatively simple to implement, and only affects the interface communicating information between the macro-scale FEM and micro-scale DEM models. In other words, it does not require internal modifications of the FEM and DEM source codes, so that the approach also can be combined with commercially available software for which the user typically has no access to the source code. In addition to its simplicity, the servo-control algorithm preserves the physical interpretation of the homogenized stress measure derived for the particle packing, and furnishes a realistic value for the stress in the limit case at which the micro-scale boundary condition is met exactly. It is noted that the algorithm only considers the (P) and (T) boundary conditions, since for a macro-scale problem discretized with a displacement-based

DEM code, the (D) boundary condition can be implemented in a straightforward fashion, without the use of iterations.

Apart from providing servo-control algorithms for the individual (P) and (T) boundary conditions, a novel formulation for *mixed* (D)-(P)-(T) *boundary conditions* is derived, and subsequently cast into a numerical formalism. The formulation is proven to satisfy the Hill-Mandel micro-heterogeneity condition, and therefore is very useful for i) a consistent derivation of macro-scale constitutive relations from standard material tests on particle aggregates subjected to any combination of (D)-, (P)- and/or (T)-type boundary conditions, and ii) the efficient computation of the homogenized response of large-scale particle aggregates characterized by a spatial periodicity in one or two directions, i.e., granular layers exposed to uniform (D) and/or (T) boundary conditions at their top and bottom surfaces. It will be demonstrated that the formulation allows to impose the (D) and (T) boundary conditions both at separate and identical parts of the layer boundary, where in the latter case the (D) and (T) contributions obviously need to be applied along different orthonormal directions.

The performance of the servo-control algorithms developed for the various micro-scale boundary conditions is tested by using monodisperse and polydisperse frictional and cohesive packings composed of two-dimensional, circular particles and subjected to various loading paths. These examples illustrate the basic features of each of the boundary conditions in full detail. Despite the focus on two-dimensional particle systems, it should be mentioned that the extension of the present framework towards three-dimensional granular systems is trivial, and can be made without the introduction of additional prerequisites.

This chapter is organized as follows. Section 2.2 presents a review of the numerical homogenization framework for particle aggregates, and outlines the formulations of the micro-scale (D), (P) and (T) boundary conditions proposed in (Miehe et al., 2010). Section 2.3 discusses the numerical implementation of the micro-scale boundary conditions, where for the (P) and (T) boundary conditions two different servo-control algorithms are presented, which include or not an initial prediction of the displacements of the boundary particles based on their positions calculated at the previous loading step. In Section 2.4 the performance of the numerical algorithms is tested on monodisperse and polydisperse frictional packings subjected to various loading paths. The numerical results clearly illustrate the characteristic differences in response for the three types of boundary conditions, and show their response convergence behavior under increasing sample size. Section 2.5 presents the formulation for the mixed boundary conditions, and provides the details of the servo-control algorithm and its numerical performance for the cases of infinite frictional and cohesive granular layers loaded by a vertical compressive stress, and subsequently subjected to a horizontal shear deformation. Some concluding remarks are provided in Section 2.6.

In terms of notations, the cross product and dyadic product of two vectors are, respectively, designated as $\mathbf{a} \times \mathbf{b} = e_{ijk} a_i b_j \mathbf{e}_k$ and $\mathbf{a} \otimes \mathbf{b} = a_i b_j \mathbf{e}_i \otimes \mathbf{e}_j$, where $e_{ijk}$ is the permutation symbol, $\mathbf{e}_i$, $\mathbf{e}_j$ and $\mathbf{e}_k$ are unit vectors in a Cartesian vector basis, and Einstein's summation convention is used on repeated tensor indices.

The inner product between two vectors is given by $\mathbf{a} \cdot \mathbf{b} = a_i b_i$, and between two second-order tensors by $\mathbf{A} : \mathbf{B} = A_{ij} B_{ij}$. The action of a second-order tensor on a vector is indicated as $\mathbf{A} \cdot \mathbf{b} = A_{ij} b_j \mathbf{e}_i$. The superscript $T$ is used to indicate the transpose of a vector or a tensor. Further, $\mathbf{I} = \delta_{ij} \mathbf{e}_i \otimes \mathbf{e}_j$ denotes the second-order identity tensor, with $\delta_{ij}$ the Kronecker delta symbol.

Since the present study focuses on two-dimensional particle aggregates, throughout this chapter the dimensions related to volume, area, stress and mass density are consistently presented in their reduced form as length$^2$, length, force/length and mass/length$^2$, respectively.

## 2.2 Micro-macro transitions for particle aggregates

### 2.2.1 Micro-scale geometry

The initial micro-scale granular system is characterized by a two-dimensional square domain of $P + Q$ rigid particles, which are partitioned into $P$ inner particles $\mathcal{P}_p$, with $p = 1, .., P$, and $Q$ boundary particles $\mathcal{P}_q$, with $q = 1, .., Q$, colored in yellow and red in Figure 2.1(a), respectively. The boundary particles can be further split into corner particles $\mathcal{P}_c$ with $c = 1, .., 4$ and the remaining edge particles $\mathcal{P}_e$ with $e = 1, .., E = Q - 4$. The initial interior domain $V$ comprises the inner particles with their center points as $\mathbf{X}_p \in \mathcal{P}_p$ with $p = 1, .., P$. The boundary $\partial V$ is defined by the boundary particles, whose center points in the initial configuration are $\mathbf{X}_q \in \mathcal{P}_q$ with $q = 1, .., Q$. The macroscopic deformation of the granular micro-structure is imposed via the frame of boundary particles $\mathcal{P}_q$, as a result of which the center points of the inner and boundary particles become located at $\mathbf{x}_p$ and $\mathbf{x}_q$, respectively, see Figure 2.1(b). In the current configuration, the boundary particles $\mathcal{P}_q$ are subjected to boundary forces $\mathbf{a}_q$, boundary moments $\mathbf{m}_q$, and particle contact forces $\mathbf{f}_q^c$, see Figure 2.1(c), while the inner particles $\mathcal{P}_p$ are subjected to particle contact forces $\mathbf{f}_p^c$, see Figure 2.1(d), with the superscript $c$ denoting a contact with a neighbour particle.

The macroscopic response of a granular assembly is derived by transforming relevant principles used in first-order homogenization theories (Suquet, 1985; Terada et al., 2000; Kouznetsova et al., 2001; Miehe et al., 2002) from a continuous setting to a discrete setting. Accordingly, at the centroids of the boundary particles $\mathcal{P}_q$ the finite area vectors $\mathbf{A}_q$ and forces $\mathbf{a}_q$ are derived from infinitesimal area vectors and forces, respectively,

$$\int_{\partial V} \mathbf{N} ds \rightarrow \mathbf{A}_q \qquad \text{and} \qquad \int_{\partial V} \mathbf{t}\, ds \rightarrow \mathbf{a}_q \qquad \text{for} \quad q = 1..., Q\,, \tag{2.1}$$

with $\mathbf{N}$ the vector pointing in the outward normal direction of the boundary $\partial V$ of the initial particle volume $V$, $\mathbf{t}$ being the boundary traction, and $ds$ indicating an infinitesimal part of the boundary surface. Various expressions for $\mathbf{A}_q$ have been presented in the literature, see e.g., (Miehe and Koch, 2002; Dettmar, 2006). In the present chapter the initial area vector is computed by accounting for the

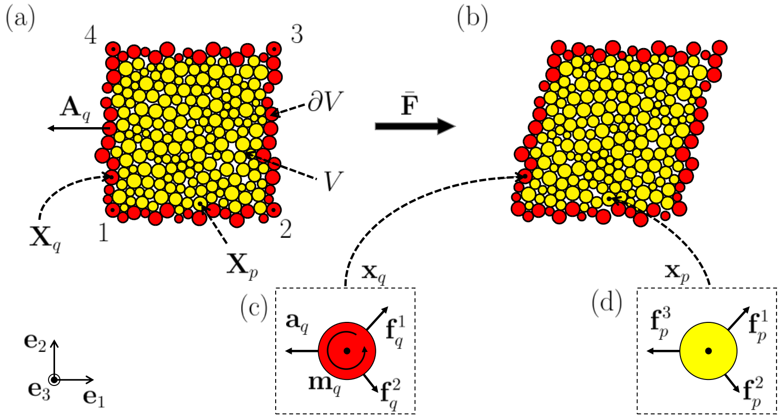

**Figure 2.1:** (a) Two-dimensional particle aggregate of initial volume $V$ and boundary $\partial V$. Yellow and red colors refer to inner $\mathcal{P}_p$ and boundary $\mathcal{P}_q$ particles, respectively; (b) Particle aggregate in the current configuration; (c) Boundary forces $\mathbf{a}_q$, boundary moments $\mathbf{m}_q$, and particle contact forces $\mathbf{f}_q^c$ acting on the boundary particles $\mathcal{P}_q$; (d) Particle contact forces $\mathbf{f}_p^c$ acting on the inner particles $\mathcal{P}_p$.

different radii of the boundary particles:

$$\mathbf{A}_q = \frac{R_q}{R_q + R_{q-1}}(\mathbf{X}_q - \mathbf{X}_{q-1}) \times \mathbf{e}_3 + \frac{R_q}{R_q + R_{q+1}}(\mathbf{X}_{q+1} - \mathbf{X}_q) \times \boldsymbol{e}_3 \,, \tag{2.2}$$

where $R_{q+1}$, $R_q$ and $R_{q-1}$ are the radii of adjacent boundary particles $q+1$, $q$ and $q-1$, respectively. Further, $\boldsymbol{e}_3$ represents the unit vector in the out-of-plane direction of the two-dimensional particle structure, see also Figure 2.1(a). Note that in (2.2) the boundary particles must be numbered in the anti-clockwise direction in order to obtain an area vector pointing in the outward normal direction of the boundary.

It is remarked that the formulation of the proposed homogenization scheme in principle is independent of the chosen shape of the micro-scale particle system, see also (Miehe et al., 2010); however, a slightly different implementation strategy may be required when considering non-rectangular particle systems.

### 2.2.2 Micro-scale governing equations

In what follows, firstly, equilibrium definitions for a granular micro-structure, an inner particle and a boundary particle are presented. Secondly, particle contact laws describing the interaction between two contacting particles are outlined. Thirdly, the dynamic relaxation procedure is introduced whereby the kinetic energy is dissipated out.

#### 2.2.2.1 Equilibrium conditions

In the absence of body forces, the mechanical equilibrium of a granular microstructure can be formulated in terms of the boundary forces $\mathbf{a}_q$ and moments $\mathbf{m}_q$ acting on the boundary particles $\mathcal{P}_q$:

$$\sum_{q=1}^{Q} \mathbf{a}_q = \mathbf{0} \qquad \text{and} \qquad \sum_{q=1}^{Q} (\mathbf{x}_q \times \mathbf{a}_q + \mathbf{m}_q) = \mathbf{0} \qquad \text{for} \qquad q = 1..., Q\,, \tag{2.3}$$

with $\mathbf{x}_q$ the current position vector of the boundary particles. The boundary forces $\mathbf{a}_q$ and moments $\mathbf{m}_q$ thus drive the overall, macroscopic deformation of the granular system via the frame of boundary particles.

Note that, besides global equilibrium (2.3), local equilibrium conditions may be formulated for each of the inner particles $\mathcal{P}_p$, which interact through contact forces $\mathbf{f}_p^c$ at discrete contact points $\mathbf{x}_p^c$ on the particle surfaces:

$$\sum_{c=1}^{N_p^c} \mathbf{f}_p^c = \mathbf{0} \qquad \text{and} \qquad \sum_{c=1}^{N_p^c} (\mathbf{x}_p^c - \mathbf{x}_p) \times \mathbf{f}_p^c = \mathbf{0} \qquad \text{for} \qquad p = 1..., P\,, \tag{2.4}$$

with the superscript $c$ referring to a particle contact, $N_p^c$ being the number of contact forces related to particle $p$ and $\mathbf{x}_p$ is the current position vector of the inner particle. Analogous conditions may be written for the boundary particles $\mathcal{P}_q$, for which discrete contact forces $\mathbf{f}_q^c$ act at contact points $\mathbf{x}_q^c$ on the particle surfaces. The frame of boundary particles is driven by boundary forces $\mathbf{a}_q$ and boundary moments $\mathbf{m}_q$,

$$\begin{aligned} &\sum_{c=1}^{N_q^c} \mathbf{f}_q^c = -\mathbf{a}_q \qquad \text{and} \\ &\qquad \sum_{q=1}^{N_q^c} (\mathbf{x}_q^c - \mathbf{x}_q) \times \mathbf{f}_q^c = -\mathbf{m}_q \qquad \text{for} \qquad q = 1..., Q\,, \end{aligned} \tag{2.5}$$

where $N_q^c$ is the number of contact forces for particle $q$. Note that the combination of expressions (2.4) and (2.5) is in correspondence with relation (2.3).

#### 2.2.2.2 Particle contact laws

In order to solve the micro-scale problem, the constitutive response of the granular assembly needs to be defined through a relation between the contact forces $\mathbf{f}_i^c$ (or contact moments $\mathbf{m}_i^c$), with $i = 1, ..., P + Q$, and the corresponding contact displacements $\Delta\mathbf{u}_i^c$ (or contact rotations $\Delta\boldsymbol{\theta}_i^c$). For the sake of clarity, in the following the superscript $c$ and subscript $i$ will be dropped. Two types of particle contact interactions will be considered, which are referred to as *frictional contact* and *cohesive contact*.

In accordance with (Cundall and Strack, 1979), in the *frictional contact* law the normal particle contact force $f_n$ is proportional to the normal overlap $\Delta u_n$ between two particles in contact via a multiplication by the normal contact stiffness $k_n$. The tangential particle contact force $f_s$ is proportional to the relative tangential displacement $\Delta u_s$ at the particle contact via a multiplication by the tangential contact stiffness $k_s$, up to a limit value at which frictional sliding starts, as defined by the normal force multiplied by the friction coefficient $\mu$. The contact law is thus expressed as

$$f_n = k_n \Delta u_n \qquad \text{and} \qquad f_s = \begin{cases} k_s \Delta u_s & \text{if} \quad |f_s| < -\mu f_n \,, \\ \mu f_n & \text{otherwise}\,. \end{cases} \tag{2.6}$$

For the *cohesive contact* law, two particles in contact are assumed to be initially bonded according to the constitutive model presented in (Wang and Mora, 2008; Wang, 2009), which proposes a linear relation between the force (or moment) and the corresponding relative displacement (or rotation) at the particle contact:

$$f_n^b = k_n^b \Delta u_n \qquad \text{and} \qquad f_s^b = k_s^b \Delta u_s \qquad \text{and} \qquad m_\theta^b = k_\theta^b \Delta \theta^b \,, \tag{2.7}$$

where the superscript $b$ refers to "bond". In specific, the relative displacements between two particles in the normal and tangential directions of the contact, $\Delta u_n$ and $\Delta u_s$, are, respectively, related to the normal and tangential bond forces $f_n^b$ and $f_s^b$ through a multiplication by the bond stiffnesses $k_n^b$ and $k_s^b$, respectively. Similarly, the relative angular rotation $\Delta\theta^b$ is related to the contact moment $m_\theta^b$ through a multiplication by the bond bending stiffness $k_\theta^b$. The bond between two particles is considered as broken when the following failure criterion is met:

$$\frac{f_n^b}{f_n^{b,u}} + \frac{|f_s^b|}{f_s^{b,u}} + \frac{|m_\theta^b|}{m_\theta^{b,u}} = 1 \,, \tag{2.8}$$

where $f_n^{b,u}$ is the (ultimate) tensile strength, $f_s^{b,u}$ is the shear strength and $m_\theta^{b,u}$ is the bending strength. After breakage of the contact the particle interaction is described by the frictional contact law presented in expression (2.6).

#### 2.2.2.3 Dynamic relaxation

The equilibrium conditions described by equations (2.3) to (2.5) are solved by applying a dynamic relaxation method, in which the kinetic energy activated by the applied deformation is dissipated to arrive at the equilibrium state. For each particle $i$, where $i = 1,..,P+Q$, a vector of generalized coordinates is defined as $\mathbf{d}_i = [\mathbf{x}_i,\ \boldsymbol{\theta}_i \cdot \mathbf{e}_3]^T$, which includes the particle center location $\mathbf{x}_i$ and rotation $\boldsymbol{\theta}_i$. In addition, a generalized force vector is introduced, $\mathbf{p}_i = [\mathbf{f}_i,\ \mathbf{m}_i \cdot \mathbf{e}_3]^T$, which contains the forces and moments acting on the particle. Accordingly, the generalized equation of motion of particle $i$ can be expressed as

$$\mathbf{M}_i\ddot{\mathbf{d}}_i = (\mathbf{p}_r + \mathbf{p}_d)_i \qquad \text{for} \qquad i = 1..., P+Q\,, \tag{2.9}$$

where the mass matrix $\mathbf{M}_i = \mathrm{diag}\,[M_i, I_i]$ includes the particle mass $M_i$ and particle mass moment of inertia $I_i = 1/2\ M_i R_i^2$, with $R_i$ the particle radius. The term $\ddot{\mathbf{d}}_i$ represents the generalized acceleration vector, with a superimposed dot indicating a derivative with respect to time. The vector $\mathbf{p}_r$ is the generalized force vector composed of the resultant force $\mathbf{f}_r$ and moment $\mathbf{m}_r$ acting on particle $i$, and $\mathbf{p}_d = [\mathbf{f}_d,\ \mathbf{m}_d \cdot \mathbf{e}_3]^T$ is the vector containing the resulting particle force and moment following from the artificial dissipation applied in the simulations to improve the convergence rate towards the equilibrium state. Following (Potyondy and Cundall, 2004), the artificial dissipative force $\boldsymbol{f}_d$ and moment $\boldsymbol{m}_d$ are here defined as

$$\mathbf{f}_d = -\alpha|\mathbf{f}_r|\,\mathrm{sign}(\dot{\mathbf{x}}_i) \qquad \text{and} \qquad \mathbf{m}_d = -\beta|\mathbf{m}_r|\,\mathrm{sign}(\dot{\boldsymbol{\theta}}_i)\,, \tag{2.10}$$

where $\alpha$ and $\beta$ are damping values related to (signum functions of) the particle translational velocity $\dot{\mathbf{x}}_i$ and rotational velocity $\dot{\boldsymbol{\theta}}_i$, respectively. Further, $|.|$ refers to the absolute values of the components of the corresponding vector.

The time integration of the governing equations is performed by applying an explicit, first-order finite difference scheme, which, for each time step $t_{h+1}$, with the time increment given by $\Delta t = t_{h+1} - t_h$, allows for an explicit update of the particle acceleration, velocity and displacement, see (Weatherley et al., 2014) for more details. The dynamic relaxation process is considered to be converged towards the equilibrium state when the ratio between the kinetic energy $E_k$ of the inner particles in the aggregate and their potential energy $E_p$ is lower than a prescribed tolerance (Imole et al., 2013), i.e.,

$$E_k/E_p \leq \mathrm{tol}_E\,, \tag{2.11}$$

in accordance with the following definitions

$$\begin{aligned} E_k &= \sum_{i=1}^{P} \frac{1}{2}\dot{\mathbf{d}}_i^T \mathbf{M}_i \dot{\mathbf{d}}_i \qquad \text{and} \\ E_p &= \sum_{c=1}^{N^c} \frac{1}{2}\left(k_n\,(\Delta u_n^c)^2 + k_s\,(\Delta u_s^c)^2\right)\,, \end{aligned} \tag{2.12}$$

where $\Delta u_n^c$ and $\Delta u_s^c$ are the relative displacements in the normal and tangential direction of particle contact $c$ and $N^c$ is the total number of particle contacts. Note that for the cohesive contact law given by equations (2.7) and (2.8) the potential energy in (2.12) needs to be extended with the rotational term $k_\theta(\Delta\theta^c)^2/2$.

Obviously, for deriving the solution of a boundary value problem, the equation of motion (2.9) and the constitutive response of the particles (2.6) and (2.7) should be complemented by the appropriate boundary conditions. As mentioned in the introduction, the numerical implementation of the micro-scale boundary conditions is based on the formulation presented in (Miehe et al., 2010), and the main equations are summarized in Section 2.2.3 for the sake of clarity.

### 2.2.3 Micro-scale kinematics and boundary conditions

Consider a rigid particle $i$ within a granular assembly. The current location $\mathbf{x}$ of an arbitrary material point, located within the initial particle volume at $\mathbf{X}$, is defined through the non-linear deformation map $\mathbf{x} = \boldsymbol{\psi}_i(\mathbf{X})$, with $\boldsymbol{\psi}_i$ as

$$\boldsymbol{\psi}_i(\mathbf{X}) = \mathbf{x}_i + \mathbf{Q}_i \cdot (\mathbf{X} - \mathbf{X}_i) \qquad \text{for} \quad i = 1..., P+Q\,, \tag{2.13}$$

where $\mathbf{x}_i$ and $\mathbf{X}_i$ are the current and original positions of the center of particle $i$, and $\mathbf{Q}_i$ is the second-order particle transformation tensor. For plane problems defined with respect to the orthonormal tensor basis $\{\mathbf{e}_k \otimes \mathbf{e}_l\}^2_{k,l=1,2}$, the transformation tensor of particle $i$ can be expressed as $\mathbf{Q}_i = \cos\theta_i \mathbf{e}_1 \otimes \mathbf{e}_1 - \sin\theta_i \mathbf{e}_1 \otimes \mathbf{e}_2 + \sin\theta_i \mathbf{e}_2 \otimes \mathbf{e}_1 + \cos\theta_i \mathbf{e}_2 \otimes \mathbf{e}_2$, with $\theta_i$ the magnitude of the particle center rotation $\boldsymbol{\theta}_i = \theta_i \boldsymbol{e}_3$, where $\boldsymbol{e}_3$ is the unit vector normal to the plane. In addition, the current position of the particle center $\mathbf{x}_i$ can be expressed as the sum of a contribution affine to the macroscopic deformation gradient $\bar{\boldsymbol{F}}$ and a local, micro-scale fluctuation $\mathbf{w}_i$:

$$\mathbf{x}_i = \bar{\boldsymbol{F}} \cdot \mathbf{X}_i + \mathbf{w}_i \qquad \text{for} \quad i = 1..., P+Q\,. \tag{2.14}$$

In homogenization schemes for continuous media, the macro-to-micro scale transition is enforced by requiring the macro-scale deformation gradient to be equal to the volume average of the micro-scale deformation gradient. In a discrete setting, this is equivalent to the condition

$$\bar{\boldsymbol{F}} = \frac{1}{V} \sum_{q=1}^{Q} \mathbf{x}_q \otimes \boldsymbol{A}_q\,. \tag{2.15}$$

Relation (2.15) can be derived by transforming the volume average of the micro-scale deformation into a surface integral

$$\bar{\boldsymbol{F}} = \frac{1}{V}\int_V \boldsymbol{F} dv = \frac{1}{V}\int_V \nabla \boldsymbol{x} dv = \frac{1}{V}\int_{\partial V} \boldsymbol{x} \otimes \boldsymbol{N} ds\,, \tag{2.16}$$

with $\boldsymbol{N}$ the vector normal to the outer boundary of the original particle volume, and subsequently performing the transition from a continuous to a discrete setting with the aid of $(2.1)_1$.

Equation (2.15) needs to be satisfied by applying specific boundary conditions to the boundary particles of the granular micro-structure. For continuous media, this goal is typically accomplished by applying one of the three classical types of boundary conditions, namely i) a homogeneous deformation, also known as the displacement boundary condition and thus abbreviated as (D), ii) periodic displacements (P), and iii) a uniform traction (T), see, e.g., (Kouznetsova et al., 2001; Terada et al., 2000; Miehe et al., 2002). For discrete particle structures, however, additional conditions need to be imposed on the rotations or moments of the boundary particles. Correspondingly, along the lines of (Miehe et al., 2010), the three boundary conditions mentioned above are extended as i) homogeneous deformation and zero rotation (D), ii) periodic displacement and periodic rotation (P), and iii) uniform force and free rotation (T), of which the formulations are presented below. The abbreviations (D), (P) and (T), although typically used in continuum homogenization theories, are maintained here for reasons of consistency. In addition to the three classical boundary conditions, a novel combination of these boundary conditions has been derived, which will be referred to as "mixed boundary conditions". The corresponding formulation is proven to satisfy the consistency of energy between the microscopic and macroscopic scales of observation, known as the Hill-Mandel micro-heterogeneity condition, and the details are provided in Section 2.5.

#### 2.2.3.1 Homogeneous deformation and zero rotation (D)

In accordance with this boundary condition, all the boundary particles $\mathcal{P}_q$ are prescribed to have zero micro-scale displacement fluctuations and zero rotations:

$$\mathbf{x}_q = \bar{\boldsymbol{F}} \cdot \boldsymbol{X}_q \qquad \text{and} \qquad \mathbf{Q}_q = \boldsymbol{I} \qquad \text{on} \qquad \partial V\,, \tag{2.17}$$

where the first expression follows from (2.14) with the displacement fluctuations as $\mathbf{w}_q = \mathbf{0}$. Due to the second condition in (2.17) the boundary moments do not vanish, i.e.,

$$\mathbf{m}_q \neq \mathbf{0} \qquad \text{on} \qquad \partial V\,. \tag{2.18}$$

The homogeneous deformation and zero rotation boundary condition is expected to result in a relatively stiff macroscopic response of the particle aggregate.

#### 2.2.3.2 Periodic displacement and periodic rotation (P)

For this boundary condition, both the displacements and rotations of the boundary particles $\mathcal{P}_q$ are related by periodicity requirements:

$$\mathbf{x}_q^+ - \mathbf{x}_q^- = \bar{\boldsymbol{F}} \cdot (\mathbf{X}_q^+ - \mathbf{X}_q^-) \qquad \text{and} \qquad \mathbf{Q}_q^+ - \mathbf{Q}_q^- = \mathbf{0} \qquad \text{on} \qquad \partial V\,, \tag{2.19}$$

where the superscripts $^+$ and $^-$ refer to corresponding particles on opposite boundaries of the granular assembly. From the viewpoint of equilibrium, the forces and moments on opposite boundaries need to be anti-periodic, thus satisfying the relations

$$\mathbf{a}_q^+ + \mathbf{a}_q^- = \mathbf{0} \qquad \text{and} \qquad \mathbf{m}_q^+ + \mathbf{m}_q^- = \mathbf{0} \qquad \text{on} \qquad \partial V\,. \tag{2.20}$$

#### 2.2.3.3 Uniform force and free rotation (T)

The boundary forces $\mathbf{a}_q$ of the boundary particles $\mathcal{P}_q$ are here determined from the product of the macroscopic first Piola-Kirchhoff stress $\bar{\boldsymbol{P}}$ and the discrete area vectors $\mathbf{A}_q$ introduced in equation $(2.1)_1$:

$$\mathbf{a}_q = \bar{\boldsymbol{P}} \cdot \boldsymbol{A}_q \qquad \text{on} \qquad \partial V\,. \tag{2.21}$$

In addition, no constraint is applied to the boundary rotations, so that the boundary moments vanish:

$$\mathbf{m}_q = \mathbf{0} \qquad \text{on} \qquad \partial V \,. \tag{2.22}$$

The uniform force and free rotation boundary condition is expected to provide a relatively soft macroscopic response of the particle aggregate.

### 2.2.4 Macro-scale stress and Hill-Mandel condition

The first Piola-Kirchhoff stress at the macro scale is defined in terms of the boundary forces $\mathbf{a}_q$ acting on the particle aggregate:

$$\bar{\boldsymbol{P}} = \frac{1}{V} \sum_{q=1}^{Q} \mathbf{a}_q \otimes \boldsymbol{X}_q \,. \tag{2.23}$$

The Hill-Mandel micro-heterogeneity condition expresses the equality between the volume average of the virtual work applied at the boundaries of the microstructure and the virtual work of a macroscopic material point (Hill, 1963). For a discrete particle system this condition specifies

$$\bar{\boldsymbol{P}} : \delta \bar{\boldsymbol{F}} = \frac{1}{V} \sum_{q=1}^{Q} \mathbf{a}_q \cdot \delta \mathbf{x}_q \,. \tag{2.24}$$

The macroscopic stress $\bar{\boldsymbol{P}}$ given by (2.23) must satisfy the energy consistency between the two scales. Accordingly, considering definition (2.15), the following identity holds

$$\bar{\boldsymbol{P}} : \delta \bar{\boldsymbol{F}} = \bar{\boldsymbol{P}} : \frac{1}{V} \sum_{q=1}^{Q} \delta \mathbf{x}_q \otimes \mathbf{A}_q = \frac{1}{V} \sum_{q=1}^{Q} \left( \bar{\boldsymbol{P}} \cdot \mathbf{A}_q \right) \cdot \delta \mathbf{x}_q \,. \tag{2.25}$$

Alternatively, by making use of the definition of the macro-scale stress (2.23), the inner product $\bar{\boldsymbol{P}} : \delta \bar{\boldsymbol{F}}$ can be expanded as

$$\bar{\boldsymbol{P}} : \delta \bar{\boldsymbol{F}} = \frac{1}{V} \sum_{q=1}^{Q} \mathbf{a}_q \otimes \mathbf{X}_q : \delta \bar{\boldsymbol{F}} = \frac{1}{V} \sum_{q=1}^{Q} \mathbf{a}_q \cdot \left( \delta \bar{\boldsymbol{F}} \cdot \mathbf{X}_q \right) . \tag{2.26}$$

Subsequently, reformulating equation (2.24) as

$$\frac{1}{V} \sum_{q=1}^{Q} \mathbf{a}_q \cdot \delta \mathbf{x}_q - \bar{\boldsymbol{P}} : \delta \bar{\boldsymbol{F}} - \bar{\boldsymbol{P}} : \delta \bar{\boldsymbol{F}} + \bar{\boldsymbol{P}} : \delta \bar{\boldsymbol{F}} = 0 \,, \tag{2.27}$$

substituting equations (2.25) and (2.26), and keeping in mind that

$$\begin{aligned}\bar{\boldsymbol{P}} : \delta\bar{\boldsymbol{F}} &= \bar{\boldsymbol{P}} : \left(\delta\bar{\boldsymbol{F}} \cdot \frac{1}{V}\sum_{q=1}^{Q} \mathbf{X}_q \otimes \mathbf{A}_q\right) \\ &= \bar{\boldsymbol{P}} : \left(\frac{1}{V}\sum_{q=1}^{Q} \delta\bar{\boldsymbol{F}} \cdot \mathbf{X}_q \otimes \mathbf{A}_q\right) \\ &= \frac{1}{V}\sum_{q=1}^{Q}(\bar{\boldsymbol{P}} \cdot \mathbf{A}_q) \cdot (\delta\bar{\boldsymbol{F}} \cdot \mathbf{X}_q),\end{aligned} \tag{2.28}$$

leads to

$$\frac{1}{V}\sum_{q=1}^{Q} \left(\mathbf{a}_q - \bar{\boldsymbol{P}} \cdot \mathbf{A}_q\right) \cdot \left(\delta\mathbf{x}_q - \delta\bar{\boldsymbol{F}} \cdot \mathbf{X}_q\right) = 0\,. \tag{2.29}$$

Invoking the micro-scale displacement fluctuations in accordance with relation (2.14) turns expression (2.29) finally into

$$\frac{1}{V}\sum_{q=1}^{Q} \left(\mathbf{a}_q - \bar{\boldsymbol{P}} \cdot \mathbf{A}_q\right) \cdot \delta\mathbf{w}_q = 0\,. \tag{2.30}$$

Note that the recast form (2.30) of the Hill-Mandel condition is satisfied for all three types of boundary conditions introduced above: For the (D) boundary condition, the combination of equations (2.14) and (2.17) results in $\delta\mathbf{w}_q = \mathbf{0}$. For the (P) boundary condition, the periodicity of the micro-fluctuations of the boundary displacements $\mathbf{w}_q^+ = \mathbf{w}_q^-$ and the anti-periodicity of the boundary forces $\mathbf{a}_q^+ = -\mathbf{a}_q^-$, following from equations (2.19) and (2.20), respectively, make their products in expression (2.30) vanish for opposite boundaries. For the (T) boundary condition, relation (2.21) leads to $\mathbf{a}_q - \bar{\boldsymbol{P}} \cdot \mathbf{A}_q = \mathbf{0}$.

It should be mentioned that the Hill-Mandel condition elaborated above only accounts for the influence of contact forces acting on boundary particles, and does not include the effect of contact moments. This is consistent with the assumption of a standard (Boltzmann) continuum at the macro scale, which contains displacement degrees of freedom but does not consider rotations. This assumption is satisfied for the frictional contact law, in which the contact moments are absent, see expression (2.6). For the cohesive contact law, the contact moments contribute both to the elastic behavior and the strength criterion, see expressions (2.7) and (2.8), respectively. The extension of a contact law with a contact moment contribution formally introduces a couple stress in the macroscopic response of the particle aggregate, which is energetically conjugated to the gradient of the overall rotation, see e.g., (Mühlhaus and Vardoulakis, 1987; Chang and Liao, 1990; Chang and Ma, 1992; Suiker et al., 2001a,b; Suiker and de Borst, 2005). These higher-order stress and deformation measures correspond to higher-order natural and essential boundary data (Suiker and de Borst, 2005), which are known to be difficult to measure in experiments, and commonly are (substantially) lower in magnitude than the classical boundary data. For these reasons, and from the fact that the cohesive contact law defined by equations (2.7) and (2.8) is used only for one example discussed at the end of this chapter, see Section 2.5.3, an extension of the Hill-Mandel condition with the effect of a contact moments is omitted here, but may be considered as a topic for future research. Correspondingly, for the cohesive contact law a consistency in energy between the micro- and macro-scales of a particle aggregate can only be warranted in an approximate fashion.

In Sections 2.4 and 2.5, the results of the DEM analyses will be presented in terms of components of the macro-scale Cauchy stress tensor $\bar{\boldsymbol{\sigma}}$. This stress measure can be derived from the first Piola-Kirchhoff stress $\bar{\boldsymbol{P}}$ computed through (2.23) by using the common transformation rule:

$$\bar{\boldsymbol{\sigma}} = \frac{1}{\det\left(\bar{\boldsymbol{F}}\right)} \bar{\boldsymbol{P}} \cdot \bar{\boldsymbol{F}}^T . \tag{2.31}$$

## 2.3 Numerical implementation of micro-scale boundary conditions

The micro-scale boundary conditions outlined above were implemented by using the open-source discrete element code ESyS-Particle (Virgo et al., 2013; Guo and Zhao, 2013). The numerical algorithms developed for this purpose are described below.

### 2.3.1 Homogeneous deformation and zero rotation (D)

The homogeneous deformation and zero rotation boundary condition (D) given by equation (2.17) can be implemented straightforwardly by imposing this condition in an incremental fashion on the boundary particles $\mathcal{P}_q$. After moving the boundary particles in accordance with the incremental update of the deformation $\bar{\boldsymbol{F}}$, dynamic relaxation is applied to reach the equilibrium state of the particle aggregate, during which the displacements imposed on the boundary particles remain fixed. The particle configuration corresponding to the equilibrium state is stored, and the next deformation increment is applied. This process is repeated until the total number of deformation increments $i_{tot}$ is reached. The details of the algorithm are summarized in Table 2.1.

**Table 2.1:** Algorithm for the (D) boundary condition.

```
1. DEM simulation. Increments $0 \leq i \leq i_{tot}$
        1.1 Apply updated boundary conditions
                $\mathbf{x}_q = \bar{\boldsymbol{F}}\mathbf{X}_q$    and  $\mathbf{Q}_q = \mathbf{I}$    for  $q = 1..., Q$
        1.2 Dynamic relaxation until equation (2.11) is satisfied
        1.3 Save current configuration and go to 1 (next increment $i + 1$)
```

### 2.3.2 Periodic displacement/periodic rotation (P) and uniform force/free rotation (T)

The periodic displacement and periodic rotation boundary condition (P) and the uniform force and free rotation boundary condition (T) were numerically implemented by means of a servo-control algorithm, which uses a feedback principle similar to that of algorithms commonly applied within control theory of dynamic systems (Åström and Murray, 2008). More specifically, the algorithms iteratively correct the boundary particle displacements and rotations from a gradually diminishing discrepancy between the measured and the required values of the boundary condition.

For the periodic displacement and periodic rotation boundary condition (P), the boundary forces and boundary moments should satisfy the anti-periodicity conditions presented in equation (2.20). Accordingly, the corresponding residuals for the edge particles are

$$\Delta \mathbf{a}_e = \mathbf{a}_e^+ + \mathbf{a}_e^- , \quad \Delta m_e = (\mathbf{m}_e^+ + \mathbf{m}_e^-) \cdot \mathbf{e}_3 \quad \text{for } e = 1..., E/2 . \qquad (2.32)$$

Multiplying the residuals by corresponding gain parameters $g_a^p$ and $g_m^p$ results into the following displacement and rotation corrections for the edge particles:

$$\Delta \mathbf{u}_e^+ = \Delta \mathbf{u}_e^- = g_a^p \Delta \mathbf{a}_e , \quad \Delta \theta_e^+ = \Delta \theta_e^- = g_m^p \Delta m_e \quad \text{for } e = 1..., E/2 , \qquad (2.33)$$

which are added to the particle locations and rotations from the previous iteration. Note that the four corner particles straightforwardly follow the macroscopic deformation $\bar{\boldsymbol{F}}$, by prescribing their displacements in accordance with equation (2.17). Hence, for these particles no displacement correction is needed. The rotations of the four corner particles will be updated similarly to (2.33), using the corrections

$$\Delta \theta_c^+ = \Delta \theta_c^- = g_m^p \Delta m_c \quad \text{with} \quad \Delta m_c = \sum_{c=1}^{4} \boldsymbol{m}_c \cdot \boldsymbol{e}_3 . \qquad (2.34)$$

For the uniform force/free rotation boundary condition (T), the boundary forces ensue from the applied macroscopic stress through expression (2.21). However, since the solution procedure is deformation-driven, the constraint given by (2.21) cannot be enforced directly on the micro-scale particle structure. Correspondingly, an additional condition that depends explicitly on the macroscopic deformation $\bar{\boldsymbol{F}}$ should be used. This condition is given by expression (2.15), which represents the weak counterpart of expression (2.21), see also (Miehe et al., 2010). Hence, the two corresponding residuals are formulated as

$$\Delta \mathbf{a}_q = \bar{\boldsymbol{P}} \cdot \mathbf{A}_q - \mathbf{a}_q , \quad \Delta \bar{\boldsymbol{F}}_q = V \bar{\boldsymbol{F}} \cdot \mathbf{A}_q - \sum_{r=1}^{Q} (\mathbf{A}_q \cdot \mathbf{A}_r) \, \mathbf{x}_r \quad \text{for } q = 1..., Q . \qquad (2.35)$$

The correction for the displacement of the boundary particles is derived by multiplying the force and deformation residuals in (2.35) by the gain parameters $g_a^t$

and $g_F^t$, respectively, leading to

$$\Delta \mathbf{u}_q = g_a^t \Delta \mathbf{a}_q + g_F^t \Delta \bar{\boldsymbol{F}}_q \qquad \text{for } q = 1..., Q\,. \tag{2.36}$$

When performing numerical simulations, the specific values of the gain parameters $g_a^p$, $g_m^p$, $g_a^t$, $g_F^t$ need to be fine-tuned from accuracy and stability considerations of preliminary numerical benchmark tests.

The corrections for the displacement and rotation of the boundary particles were implemented by means of two different algorithms, which consider or not an initial prediction of the position of the boundary particles based on their positions calculated at the previous loading step. These algorithms are therefore given the labels “with initial displacement prediction” and “without initial displacement prediction”. The algorithms are discussed below, and their effect on the computational results will be investigated in Section 2.4. The specific parts of the algorithms that refer to the periodic displacement and periodic rotation boundary condition will be denoted by the symbol (P), while the symbol (T) indicates the uniform force and free rotation boundary condition. Finally, the residuals defined in expressions (2.32) and (2.35), which relate to the particle force, particle moment and macroscopic deformation gradient, are evaluated at each iteration by subjecting their dimensionless form to a convergence check. The dimensionless forms are obtained through, respectively, a normalization by the following parameters:

$$\tilde{a}_k = \frac{M_k R_k}{\Delta t^2}, \qquad \tilde{m}_k = \frac{M_k R_k^2}{\Delta t^2}, \qquad \tilde{F}_k = R_k^3\,, \tag{2.37}$$

with $k = c, e, q$ referring to corner, edge, and boundary particles, respectively. In (2.37), $M_k$ is the mass of particle $k$, $R_k$ is its radius and $\Delta t$ is the time increment used in the dynamic relaxation procedure.

#### 2.3.2.1 Algorithm with initial displacement prediction

The macroscopic deformation is imposed in $i_{tot}$ steps on the boundary particles $\mathcal{P}_q$ via the incrementally updated deformation gradient $\bar{\boldsymbol{F}}$. In correspondence with the algorithm presented in Table 2.2, in the initialization step, $i = 0$, the boundary particles are moved in accordance with a homogeneous deformation, and for the periodic boundary also a zero rotation, similar to equation (2.17). Subsequently, the granular assembly is dynamically relaxed to the equilibrium state, keeping the translational and, for the periodic boundary, rotational degrees of freedom of the boundary particles fixed. The iterative loop is entered, and the actual values of the forces and moments of the boundary particles are recorded. For the (P) boundary condition, the corrections for obtaining periodic particle translations and rotations at the boundary are calculated for the corner and edge particles separately, in accordance with relations (2.32)-(2.34). For the (T) boundary condition, the boundary moments vanish and the displacement corrections are computed via (2.35)-(2.36). The residuals are computed and compared with prescribed tolerances. For the (P) boundary condition, the residual is based on boundary forces and moments. For the (T) boundary condition, two residuals are calculated, which are based on the boundary forces and on the imposed macroscopic deformation. If the norm of the residual(s) is(are) smaller than the tolerance(s) (referred to as $\epsilon_a$ for the force criterion and $\epsilon_F$ for the deformation criterion), the iterative loop is terminated and the next loading step is applied. If the convergence criterion is not satisfied, the corrections are computed again and the residual is iteratively re-examined, until convergence is reached.

After the initialization step is concluded, the responses for subsequent increments, $1 \leq i \leq i_{tot}$, are calculated, see Table 2.2. For the (P) boundary condition, the corner nodes are moved by straightforwardly imposing the updated macro-scale deformation in accordance with relation (2.17). For the edge particles, their current position is determined from a prediction based on the particle position in the previous loading step $i-1$. More specifically, this prediction is a function of the position a particle would have in case of a homogeneous deformation (using the displacement boundary condition (2.17)), plus the difference, multiplied by an inheritance factor $n_f$, between the final particle position at the previous increment and the position the particle would have at the previous increment under a homogeneous deformation. The inheritance factor lies between 0 and 1, and its optimal value (in terms of computational efficiency) depends on the loading conditions applied and the characteristics of the particle assembly. For the (T) boundary condition, the prediction occurs in an analogous fashion and is applied to all the boundary particles. After the boundary particles are translated in accordance with the predicted values of their positions, the granular assembly is dynamically relaxed to its equilibrium state defined by equation (2.11). Subsequently, the iterative loop is entered, which invokes the previously described correction procedure of the displacements and rotations, in correspondence with the servo-control methodology.

#### 2.3.2.2 Algorithm without initial displacement prediction

Similar to the algorithm with initial displacement prediction, for the algorithm without initial displacement prediction the macroscopic deformation is imposed in $i_{tot}$ steps to the boundary particles $\mathcal{P}_q$. However, as pointed out in Table 2.3, all increments are now treated in the same fashion. The boundary particles are initially moved in accordance with the updated homogeneous macroscopic deformation $\bar{\boldsymbol{F}}$, similar to expression (2.17), after which the particle assembly is dynamically relaxed to its equilibrium state. The iterative loop is started, in which the corrections for the displacement and rotation of the boundary particles are calculated based on the servo-control methodology. For the (P) boundary condition, the boundary is partitioned into corner and edge particles, whereby relations (2.32)-(2.34) are applied. For the (T) boundary condition, equations (2.35)-(2.36) are employed. Subsequently, the particle system is relaxed to the equilibrium state, and the current values of the boundary forces and moments are recorded and used to compute the residuals. If the norms of the residuals are smaller than the corresponding tolerances adopted, the iterative loop is termi-

**Table 2.2:** Algorithm for the (P) and (T) boundary conditions *with* initial displacement prediction.

**Algorithm with initial displacement prediction**

```
1. Initialization DEM simulation. Increment $i = 0$
    1.1 Initialize boundary conditions by applying updated macro-scale deformation homogeneously
        1.1.A if (P) $\Longrightarrow \mathbf{x}_q = \bar{\boldsymbol{F}}\mathbf{X}_q$ and $\mathbf{Q}_q = \mathbf{I}$ for $q = 1..., Q$
        1.1.B if (T) $\Longrightarrow \mathbf{x}_q = \bar{\boldsymbol{F}}\mathbf{X}_q$ and $\boldsymbol{m}_q = \mathbf{0}$ for $q = 1..., Q$
    1.2 Dynamic relaxation until equation (2.11) is reached. Obtain boundary forces and moments.
    1.3 Update particle configuration
        1.3.A if (P) $\Longrightarrow$ Partition the boundary into corner c and edge e particles
            Calculate edge particles displacement $\Delta\mathbf{u}_e$ and rotation $\Delta\theta_e$ corrections via (2.32)-(2.33)
            and corner particles rotation corrections $\Delta\theta_c$ via (2.34)
        1.3.B if (T) $\Longrightarrow$ Calculate boundary particles displacement correction $\Delta\mathbf{u}_q$ via (2.35)-(2.36)
    1.4 Dynamic relaxation until equation (2.11) is satisfied. Obtain boundary forces and moments.
    1.5 Calculate residual(s)
        1.5.A if (P) $\Longrightarrow r_a = \sqrt{\sum_{e=1}^{E/2}(\Delta\mathbf{a}_e \cdot \Delta\mathbf{a}_e/\tilde{a}_e^2 + (\Delta m_e/\tilde{m}_e)^2) + (\Delta m_c/\tilde{m}_c)^2}$
        1.5.B if (T) $\Longrightarrow r_a = \sqrt{\sum_{q=1}^{Q} \Delta\mathbf{a}_q \cdot \Delta\mathbf{a}_q/\tilde{a}_q^2}$ and $r_F = \sqrt{\sum_{q=1}^{Q} \Delta\bar{\boldsymbol{F}}_q \cdot \Delta\bar{\boldsymbol{F}}_q/\tilde{F}_q^2}$
    1.6 Check for convergence: $r_a \leq \epsilon_a$ for (P); $r_a \leq \epsilon_a$ and $r_F \leq \epsilon_F$ for (T)
        1.6.A if converged $\Longrightarrow$ Save current configuration and go to 2
        1.6.B if not converged $\Longrightarrow$ Return to 1.3

2. Subsequent increments $1 \leq i \leq i_{tot}$
    2.1 Apply updated boundary conditions
        2.1.A if (P) $\Longrightarrow$
            Impose updated macro-scale deformation on corner nodes: $\mathbf{x}_c = \bar{\boldsymbol{F}}\mathbf{X}_c$ and $\mathbf{Q}_q = \mathbf{I}$
            Prediction of the positions of edge particles:
            $\mathbf{x}_e^i = \mathbf{x}_e^{i,(\mathrm{D})} + n_f \left(\mathbf{x}_e^{i-1} - \mathbf{x}_e^{i-1,(\mathrm{D})}\right)$ for $e = 1...E/2$
            with $\mathbf{x}_e^{(\mathrm{D})} = \bar{\boldsymbol{F}}\mathbf{X}_e$ and the inheritance factor $0 < n_f \leq 1$
        2.1.B if (T) $\Longrightarrow$
            Prediction of the positions of boundary particles:
            $\mathbf{x}_q^i = \mathbf{x}_q^{i,(\mathrm{D})} + n_f \left(\mathbf{x}_q^{i-1} - \mathbf{x}_q^{i-1,(\mathrm{D})}\right)$ for $q = 1..., Q$
            with $\mathbf{x}_q^{(\mathrm{D})} = \bar{\boldsymbol{F}}\mathbf{X}_q$ and the inheritance factor $0 < n_f \leq 1$
    2.2 Translate particles according to predictions 2.1.A, or 2.1.B
    2.3 Dynamic relaxation until equation (2.12) is satisfied. Obtain boundary forces and moments.
    2.4 Update particle configuration with displacement and rotation corrections $\Delta\mathbf{u}$ and $\Delta\theta$
        2.4.A if (P) $\Longrightarrow$ Refer to 1.3.A
        2.4.B if (T) $\Longrightarrow$ Refer to 1.3.B
    2.5 Dynamic relaxation until equation (2.11) is satisfied. Obtain boundary forces and moments.
    2.6 Calculate residual(s)
        2.6.A if (P) $\Longrightarrow$ Refer to 1.5.A
        2.6.B if (T) $\Longrightarrow$ Refer to 1.5.B
    2.7 Check for convergence: $r_a \leq \epsilon_a$ for (P); $r_a \leq \epsilon_a$ and $r_F \leq \epsilon_F$ for (T)
        2.7.A if converged $\Longrightarrow$ Save current configuration and go to 2 (next increment $i + 1$)
        2.7.A if not converged $\Longrightarrow$ Return to 2.4
```

nated and the next loading step is applied. It can be confirmed that the algorithm without displacement prediction can be obtained as a limit case of the algorithm with initial displacement prediction by setting the inheritance factor equal to zero, $n_f = 0$, whereby the algorithmic structure provided in Table 2.2 reduces to the more compact and simpler algorithmic structure presented in Table 2.3.

**Table 2.3:** Algorithm for the (P) and (T) boundary conditions *without* initial displacement prediction.

```
Algorithm without initial displacement prediction

1. DEM simulation. Increments $0 \leq i \leq i_{tot}$
    1.1 Initialize boundary conditions by applying updated macro-scale deformation homogeneously
        1.1.A if (P) $\Longrightarrow \mathbf{x}_q = \bar{\boldsymbol{F}}\mathbf{X}_q$   and $\mathbf{Q}_q = \mathbf{I}$   for $q = 1..., Q$
        1.1.B if (T) $\Longrightarrow \mathbf{x}_q = \bar{\boldsymbol{F}}\mathbf{X}_q$   and $\boldsymbol{m}_q = \mathbf{0}$   for $q = 1..., Q$
    1.2 Dynamic relaxation until equation (2.11) is satisfied. Obtain boundary forces and moments.
    1.3 Update particle configuration
        1.3.A if (P) $\Longrightarrow$ Partition the boundary into corner c and edge e particles
            Calculate edge particles displacement $\Delta\mathbf{u}_e$ and rotation $\Delta\theta_e$ corrections via (2.32)-(2.33)
            and corner particles rotation corrections $\Delta\theta_c$ via (2.34)
        1.3.B if (T) $\Longrightarrow$ Calculate boundary particles displacement correction $\Delta\mathbf{u}_q$ via (2.35)-(2.36)
    1.4 Dynamic relaxation until equation (2.11) is satisfied. Obtain boundary forces and moments.
    1.5 Calculate residual(s)
        1.5.A if (P) $\Longrightarrow r_a = \sqrt{\sum_{e=1}^{E/2}(\Delta\mathbf{a}_e \cdot \Delta\mathbf{a}_e/\tilde{a}_e^2 + (\Delta m_e/\tilde{m}_e)^2) + (\Delta m_c/\tilde{m}_c)^2}$
        1.5.B if (T) $\Longrightarrow r_a = \sqrt{\sum_{q=1}^{Q} \Delta\mathbf{a}_q \cdot \Delta\mathbf{a}_q/\tilde{a}_q^2}$ and $r_F = \sqrt{\sum_{q=1}^{Q} \Delta\bar{\boldsymbol{F}}_q \cdot \Delta\bar{\boldsymbol{F}}_q/\tilde{F}_q^2}$
    1.6 Check for convergence: $r_a \leq \epsilon_a$ for (P); $r_a \leq \epsilon_a$ and $r_F \leq \epsilon_F$ for (T)
        1.6.A if converged $\Longrightarrow$ Save current configuration and go to 1 (next increment $i + 1$)
        1.6.B if not converged $\Longrightarrow$ Return to 1.3
```

## 2.4 Computational results for regular and irregular packings

The algorithms proposed above for the implementation of the micro-scale boundary conditions are tested on a series of DEM simulations on regular, monodisperse and irregular, polydisperse particle packings.

### 2.4.1 Regular monodisperse packing

In this section the responses of three different regular, monodisperse particle packings are considered, which consist of circular particles of radius $R = 1.02$ mm, where the centroids of two particles in contact initially are at a distance of $2.0$ mm. The initial volumes of the packings are $V = [64, 324, 784]$ mm$^2$, which are calculated from the locations of the centroids of the four corner particles. The number of particles of the three packings are equal to $n_p = [25, 100, 225]$. The particle volume fraction related to initial volume occupied by the inner particles is $\mathfrak{v} = 0.785$. The corresponding coordination number, which reflects the average number of contacts of the inner particles, equals 4.

**Table 2.4:** Physical and algorithmic model parameters.

| Parameter | Value | Unit |
|---|---|---|
| Elastic normal stiffness $k_n$ | $1 \times 10^4$ | N/m |
| Elastic tangential stiffness $k_s$ | $2 \times 10^3$ | N/m |
| Friction coefficient $\mu$ | $0.4$ | - |
| Density $\rho$ | $2 \times 10^3$ | kg/m$^2$ |
| Translational damping $\alpha$ | $0.7$ | - |
| Rotational damping $\beta$ | $0.7$ | - |
| Time increment $\Delta t$ | $10^{-6}$ | s |
| Tolerance force (P), (T) $\epsilon_a$ | $10^{-4}$ | - |
| Tolerance deformation (T) $\epsilon_F$ | $10^{-2}$ | - |
| Gain force (P) $g_a^p M/\Delta t^2$ | $1 \times 10^2$ | - |
| Gain moment (P) $g_m^p MR^2/\Delta t^2$ | $2 \times 10^2$ | - |
| Gain force (T) $g_a^t M/\Delta t^2$ | $1 \times 10^2$ | - |
| Gain deformation (T) $g_F^t R^2$ | $2 \times 10^{-5}$ | - |
| Tolerance dynamic relaxation $\mathrm{tol}_E$ | $10^{-3}$ | - |

The particles obey a frictional contact law, in correspondence with relation (2.6). Assuming relatively soft particles, the normal and tangential stiffnesses are chosen as $k_n = 10^4$ N/m and $k_s = 2 \cdot 10^3$ N/m, and the friction coefficient equals $\mu = 0.4$. The density of the particles is $\rho = 2 \cdot 10^3$ kg/m$^2$. The translational and rotational damping factors used in the dynamic relaxation procedure are $\alpha = \beta = 0.7$. The packings are subjected to a combined biaxial compression-true shear deformation

$$\bar{\boldsymbol{F}} = \mathbf{I} + \bar{F}_{11}\, \boldsymbol{e}_1 \otimes \boldsymbol{e}_1 + \bar{F}_{12}\, \boldsymbol{e}_1 \otimes \boldsymbol{e}_2 + \bar{F}_{21}\, \boldsymbol{e}_2 \otimes \boldsymbol{e}_1 + \bar{F}_{22}\, \boldsymbol{e}_2 \otimes \boldsymbol{e}_2 \,, \tag{2.38}$$

with $\bar{F}_{11} = \bar{F}_{22} = -0.03$ and $\bar{F}_{12} = \bar{F}_{21} = -0.3$, which is applied in $i_{tot} = 300$ loading steps. For reaching the equilibrium state at each loading step, the particle system is subjected to dynamic relaxation steps of constant time increments $\Delta t = 10^{-6}$s. The gain parameters (in dimensionless form) used for the correct application of the boundary conditions are: for (P) $g_a^p M/\Delta t^2 = 1 \cdot 10^2$ and $g_m^p MR^2/\Delta t^2 = 2 \cdot 10^2$; for (T) $g_a^t M/\Delta t^2 = 1 \cdot 10^2$ and $g_F^t R^2 = 2 \cdot 10^{-5}$, with $M = \rho \pi R^2$ representing the mass of the particles. The force and deformation tolerances are taken as $\epsilon_a = 10^{-4}$ and $\epsilon_F = 10^{-2}$, respectively. For the dynamic relaxation process, a value of $10^{-3}$ is adopted for $\mathrm{tol}_E$, whereby equation (2.11) must be minimally satisfied for a pre-defined, continuous period of $20\Delta t$, in order to ensure a rigorous dynamic relaxation to the equilibrium state. An overview of the model parameters is given in Table 2.4.

#### 2.4.1.1 Responses for algorithms with and without initial displacement prediction

In order to investigate the performance of the two algorithms presented in Tables 2.2 and 2.3, the packing of 25 particles is considered first. The stress responses under the combined biaxial compression-true shear loading were computed with

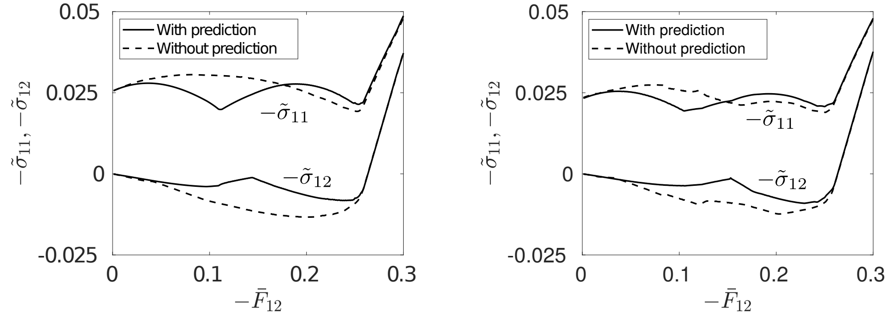

(a) (P) boundary condition (b) (T) boundary condition

**Figure 2.2:** Combined biaxial compression-true shear deformation: Normalized macroscopic Cauchy stresses $-\tilde{\sigma}_{11}$ and $-\tilde{\sigma}_{12}$ versus the shear deformation $-\bar{F}_{12}$ for (a) periodic displacement/periodic rotation boundary condition (P) and (b) uniform force/free rotation boundary condition (T). The responses relate to a regular monodisperse packing of 25 particles in a square array, and were computed by the algorithms with (solid line) and without (dot-dashed line) initial displacement predictions.

Eq.(2.31), and plotted as a function of the applied macroscopic shear deformation $\bar{F}_{12}$. Figures 2.2(a) and (b) show the results for the algorithms with (solid line) and without (dot-dashed line) an initial displacement prediction for the (P) and (T) boundary conditions, respectively. The normal and shear components of the Cauchy stress are normalized as $\tilde{\sigma}_{11} = \bar{\sigma}_{11}/k_n$ and $\tilde{\sigma}_{12} = \bar{\sigma}_{12}/k_n$, respectively, where $\bar{\sigma}_{11}$ and $\bar{\sigma}_{12}$ are the macroscopic normal and shear Cauchy stresses of the particle aggregate. For the periodic boundary conditions (P), Figure 2.3 illustrates the packing structures at specific macroscopic shear deformations $\bar{F}_{12} = -0.01$ (a), $\bar{F}_{12} = -0.113$ (b), and $\bar{F}_{12} = -0.28$ (c). The red lines plotted in the deformed particle aggregates indicate the network of normal contact forces between the particles.

For the algorithm with initial displacement prediction, the local minimum of the normal stress $\tilde{\sigma}_{11}$ near $\bar{F}_{12} = -0.113$, as shown in Figure 2.2(a) for the periodic boundary conditions (P), can be ascribed to a joint localized sliding of all the boundary particles, see Figure 2.3(b), top.

This localization mechanism does not arise for the algorithm without initial displacement prediction, which furnishes a shear response that is much more homogeneous, see Figure 2.3(b), bottom. It may be therefore concluded that the response of the packings is rather sensitive to bifurcations in the equilibrium path followed, which here become evident due to the relatively low number of particles present in the packing. Under continuing deformation towards $\bar{F}_{12} = -0.28$, the inner particles of the aggregate also develop substantial sliding, such that for both algorithms the particle structure gradually reaches its densest packing structure, at which the deformation as well as the normal contact force network

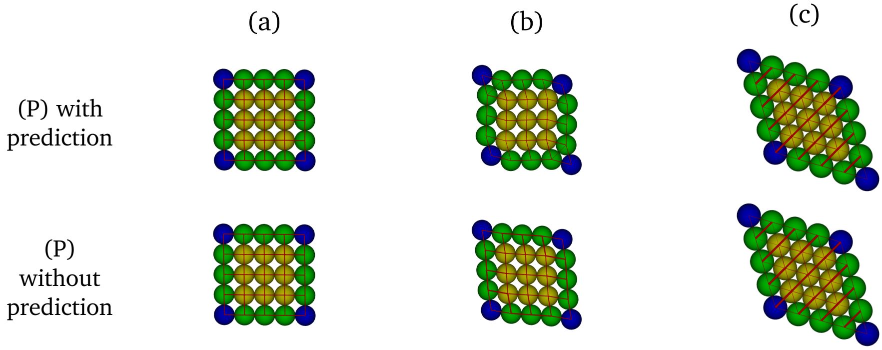

**Figure 2.3:** Combined biaxial compression-true shear deformation: Deformed configurations of a regular packing of 25 particles with (P) boundary conditions evaluated at three different deformation states: (a) $\bar{F}_{12} = -0.01$, (b) $\bar{F}_{12} = -0.113$, (c) $\bar{F}_{12} = -0.28$. The particle configurations were computed with the algorithms with (top) and without (bottom) initial displacement prediction. The red lines indicate the normal contact force network of the particles.

become strongly homogeneous. Both for the normal and shear stress components the responses computed by the two algorithms at this stage have coalesced, and steadily grow under further increasing deformation.

A similar trend can be observed for the normal and shear stress responses of the particle aggregates with the (T) boundary condition, see Figure 2.2(b). The discrepancies in the responses computed by the two algorithms appears to be less than for the (P) boundary condition.

In the simulations discussed above the two proposed algorithms have demonstrated a comparable numerical efficiency and robustness. Additional analyses not presented here nevertheless have illustrated that the performance of the algorithm with initial displacement prediction may be computationally more efficient for a well-calibrated choice of the inheritance parameter. However, if the value of the inheritance factor becomes relatively large, convergence problems may arise. Hence, for reasons of simplicity and numerical robustness, the forthcoming DEM results were computed with the algorithm without initial displacement prediction.

#### 2.4.1.2 Responses for the (D), (P) and (T) boundary conditions

The influence of the choice of the boundary condition on the overall packing response is illustrated in Figure 2.4(a). The (normalized) normal stress $\tilde{\sigma}_{11}$ is shown as a function of the applied shear deformation $\bar{F}_{12}$ for the displacement/zero rotation boundary condition (D) with a solid line, for the periodic displacement/periodic rotation boundary condition (P) with a dot-dashed line, and for the uniform force/free rotation boundary condition (T) with a dashed line. The stress response computed for the (P) boundary condition is bounded by the stiffer and softer responses measured for the (D) and (T) boundary conditions, respectively, a result that is in agreement with the numerical studies performed in (Miehe et al., 2010). It may be observed that the initial stress value corresponding to the (T) boundary condition is somewhat smaller than the value computed for the other two boundary conditions. This is, because after the sample preparation procedure was finished, the boundary forces generated by a 4% particle overlap do not exactly satisfy equation (2.21), and therefore in the first loading increment are slightly relaxed by the algorithm in order to meet this condition.

Consider the average normalized particle overlap $\Delta\bar{u}_n$, defined as

$$\Delta\bar{u}_n = \frac{1}{N^c}\sum_{c=1}^{N^c}\frac{\Delta u_n^c}{\bar{R}^c}\,, \tag{2.39}$$

where $N^c$ is total number of particle contacts, $\bar{R}^c$ is the average radius at contact $c$ and $\Delta u_n^c$ is the particle overlap at contact $c$. Figure 2.4(b) depicts $\Delta\bar{u}_n$ as a function of the applied shear deformation $-\bar{F}_{12}$. Observe that the trend for the average particle overlap is similar to that for the macroscopic normal stress in Figure 2.4(a). This can be explained as follows: The macroscopic stress is represented by the volume average of all contact forces generated within the granular micro-structure. Since the assumed normal contact stiffness is larger than the shear contact stiffness, $k_n > k_s$, see Table 2.4, the normal contact forces $f_n^c$, which are proportional to contact overlaps $\Delta u_n^c$, see expression (2.6), provide the main contribution to the macroscopic stress response, which is consistent with the statement that the load bearing capacity of a granular assembly mainly comes from the normal force between contacting particles (Rothenburg et al., 1989).

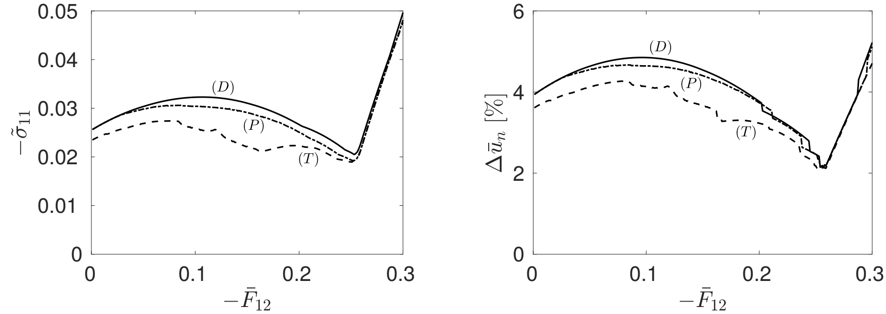

(a) Normalized Cauchy stress $-\tilde{\sigma}_{11}$ (b) Average particle overlap $\Delta\bar{u}_n$

**Figure 2.4:** Combined biaxial compression-true shear deformation: (a) Normalized homogenized Cauchy stress $-\tilde{\sigma}_{11}$ and (b) average particle overlap $\Delta\bar{u}_n$ versus the shear deformation $-\bar{F}_{12}$ for the three types of boundary conditions (D),(P) and (T).

#### 2.4.1.3 Responses for different sample sizes

The effect of the sample size on the macroscopic stress response is considered by plotting the computational results for packings composed of 25, 100 and 225 particles for the (D), (P) and (T) boundary conditions in Figures 2.5(a), (b) and (c), respectively. Generally, for a larger sample the normal stress $\tilde{\sigma}_{11}$ decreases. The (D) and (P) boundary conditions show a close resemblance in the responses for 100 and 225 particles, from which it may be concluded that for a sample of about 225 particles the stress response has more or less converged. Conversely, for the (T) boundary condition the stress for a sample of 225 particles shows a substantial relative lower value up to a deformation of $\bar{F}_{12} \approx 0.20$. This softening behavior appears to be governed by strongly localized deformations emerging at the boundaries of the particle system, a phenomenon that also has been reported for continuum homogenization methods equipped with this relatively soft boundary condition, see (Coenen et al., 2012).

### 2.4.2 Irregular polydisperse packing

The irregular polydisperse packings analyzed in this section are composed of circular particles, with the particle radii arbitrarily taken from a uniform size distribution with polydispersity $R_{max}/R_{min} = 2$, where $R_{min} = 0.67$ mm. A collision-driven molecular dynamics code described in (Donev et al., 2005) is used to randomly generate irregular packings with the initial number of particles equal to $n_p^0 = [25, 100, 200, 400, 600]$, as shown in Figure 2.6(a). Subsequently, these packings are reconstructed into geometrically periodic packings by copying each of the boundary particles intersecting with the edges of the square particle volume to corresponding positions at the opposite boundaries. This results into the packing geometries shown in Figure 2.6(b), with the final particle numbers as $n_p = [37, 120, 228, 444, 650]$. The initial volumes of the particle aggregates are equal to $V = [100, 400, 818, 1462, 2156]$ mm$^2$, respectively. The rose diagrams of the particle assemblies are sketched in Figure 2.6(c), clearly indicating that the packings become more isotropic when the particle number increases. The particle volume fraction of the packings varies in the range $\mathfrak{v} \in [0.833, 0.850]$, where the smallest and highest values correspond to the packings with the smallest and highest number of particles, respectively. The corresponding coordination numbers lie in between 2.97 and 3.47.

The particle packings are subjected to a simple shear macroscopic deformation

$$\bar{\boldsymbol{F}} = \mathbf{I} + \bar{F}_{12}\, \boldsymbol{e}_1 \otimes \boldsymbol{e}_2 \,, \tag{2.40}$$

with $\bar{F}_{12} = 0.5$, which is applied in $i_{tot} = 100$ loading steps. A step size variation study not presented here has shown that this loading step is sufficiently small for reaching a converged, pre-peak response of the micro-structural particle assembly, irrespective of the type of boundary condition applied. However, after passage of the peak load localization may occur, during which the macroscopic stress response softens; due to the appearance of numerous bifurcations

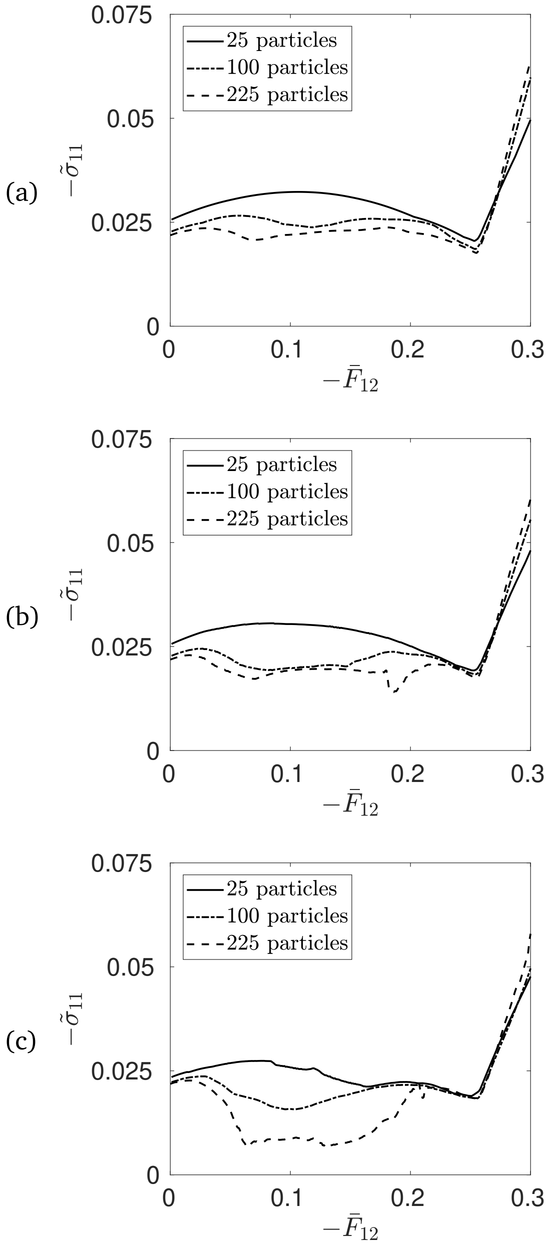

**Figure 2.5:** Combined biaxial compression-true shear deformation: Normalized macroscopic Cauchy stress $-\tilde{\sigma}_{11}$ versus the shear deformation $-\bar{F}_{12}$ for three different sample sizes of 25, 100 and 225 particles, for the (a) (D) boundary condition, (b) (P) boundary condition, and (c) (T) boundary condition.

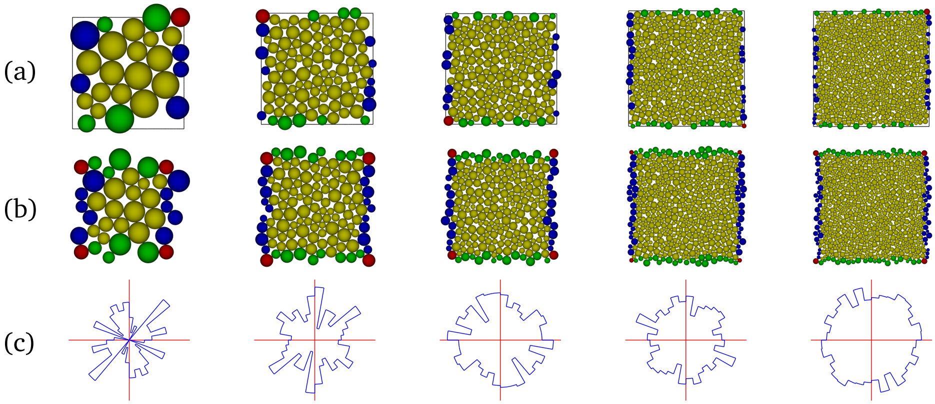

**Figure 2.6:** Characteristics of the five different irregular polydisperse packings studied: (a) Initial packings generated by a collision-driven molecular dynamics code (Donev et al., 2005), (b) geometrically periodic packings with the number of particles equal to $n_p = [37, 120, 228, 444, 650]$, and (c) the rose diagrams. It's noted that in (a) and (b) color red refers to corner particles, color blue refers to left and right boundary particles, color green refers to top and bottom boundary particles, and yellow refers to inner particles.

the equilibrium path to be followed then becomes sensitive to small physical and numerical perturbations of the particle system, such as round-off errors in the numerical scheme. Accordingly, different load step sizes may trigger different equilibrium paths and therefore can induce differences in the post-peak response computed. For the irregular packings the same physical and algorithmic parameters are used as for the regular packings, see Table 2.4, except for the tolerance $\epsilon_F = 10^{-1}$ and the two gain values for the (T) boundary condition, which here relate to $g_a^t M_i / \Delta t^2 = 5$ and $g_F^t R_i^2 = 2 \cdot 10^{-6}$, with $M_i = \rho \pi R_i^2$ being the mass of particle $i$ and $R_i$ its radius. Note that for an irregular polydisperse packing the specific gain values depend on the characteristics of the actual particle $i$.

#### 2.4.2.1 Responses for the (D), (P) and (T) boundary conditions

The response of a packing with 228 particles is considered first. The normalized macroscopic stresses $\tilde{\sigma}_{11} = \bar{\sigma}_{11}/k_n$ and $\tilde{\sigma}_{22} = \bar{\sigma}_{22}/k_n$ are shown in Figure 2.7 as a function of the applied macroscopic shear deformation $\bar{F}_{12}$. The solid, dot-dashed and dashed lines refer to the (D), (P) and (T) boundary conditions, respectively. Since for the packing of 228 particles the particle structure is rather isotropic, see Figure 2.6(c), it can be confirmed that the responses for the two normal stresses $\tilde{\sigma}_{11}$ and $\tilde{\sigma}_{22}$ indeed are similar. As for the regular monodisperse packing, the (D) and (T) boundary conditions provide the upper (stiffest) and lower (softest) bounds for the particle system response, and thereby encapsulate the response calculated for the (P) boundary condition. Although not depicted here, the responses for the normalized shear stress $\tilde{\sigma}_{12} = \bar{\sigma}_{12}/k_n$ under the (D), (P) and (T) boundary conditions follow similar trends as observed for the normal stresses $\tilde{\sigma}_{11}$ and $\tilde{\sigma}_{22}$, with the magnitude of the shear stress being about one third of that of the normal stresses.

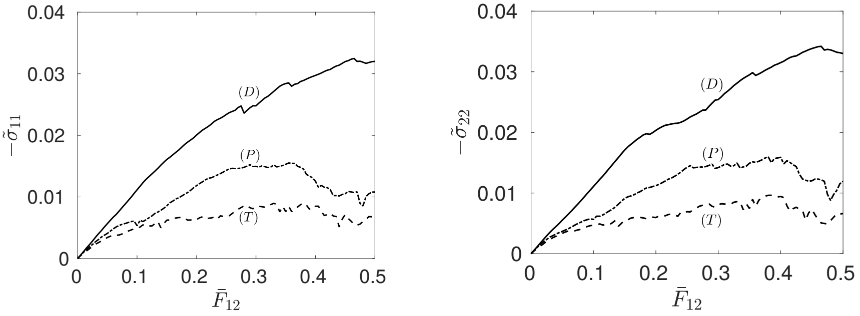

(a) Stress component $-\tilde{\sigma}_{11}$ (b) Stress component $-\tilde{\sigma}_{22}$

**Figure 2.7:** Simple shear deformation: Normalized homogenized Cauchy stresses versus the shear deformation $\bar{F}_{12}$ for packings of 228 particles, subjected to the boundary conditions (D), (P) and (T). (a) Stress component $-\tilde{\sigma}_{11}$, (b) stress component $-\tilde{\sigma}_{22}$.

Figure 2.8 shows the deformed structure of the granular aggregates for the three types of boundary conditions at four different deformation levels, namely (a) $\bar{F}_{12} = 0.05$, (b) $\bar{F}_{12} = 0.1$, (c) $\bar{F}_{12} = 0.3$ and (d) $\bar{F}_{12} = 0.5$. The local distribution of particles develops differently for the three boundary conditions, leading to differences in the network of normal contact forces represented by the red lines: The (D) and (T) boundary conditions experience the highest and lowest contact forces, respectively, as indicated by the relatively thick and thin red lines. Obviously, this is in correspondence with the largest and smallest stress levels for the (D) and (T) boundary conditions, as depicted in Figure 2.7.

Figure 2.9 illustrates the average normalized particle overlap $\Delta\bar{u}_n$, defined by relation (2.39), and the average particle rotation

$$\bar{\theta} = \frac{\sum_{i=1}^{P+Q} |\theta_i|}{P+Q}, \tag{2.41}$$

both as a function of the applied macroscopic shear deformation $\bar{F}_{12}$. As for the regular monodisperse packings, the average normalized particle overlap is the largest for the (D) boundary condition and the smallest for the (T) boundary condition, and shows a similar evolution as observed for the normal stresses, see Figure 2.7. As expected, the average rotation shows the opposite trend, being the largest for the soft (T) boundary condition and the smallest for the stiff (D) boundary condition.

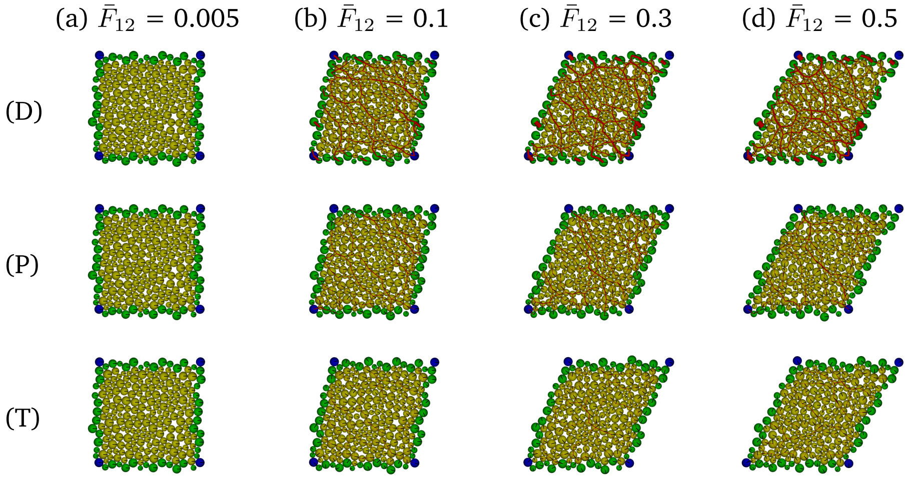

**Figure 2.8:** Simple shear deformation: Deformed configurations of an irregular packing of 228 particles evaluated at four different deformation states. (a) $\bar{F}_{12} = 0.05$, (b) $\bar{F}_{12} = 0.1$, (c) $\bar{F}_{12} = 0.3$, and (d) $\bar{F}_{12} = 0.5$, for the (D), (P) and (T) boundary conditions. The red lines indicate the normal contact force network of the particles.

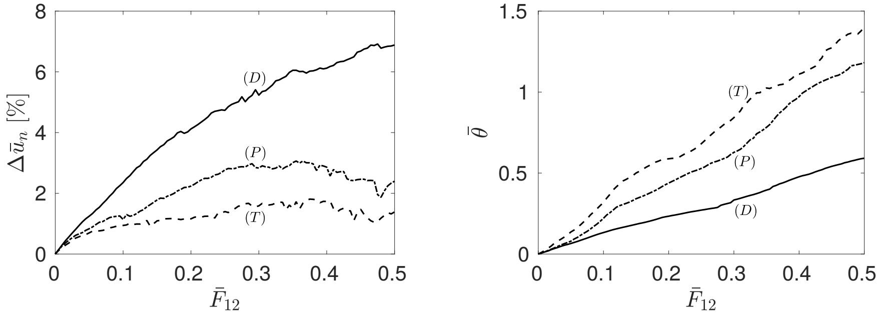

(a) Particle overlap $\Delta\bar{u}_n$ (b) Particle rotation $\bar{\theta}$

**Figure 2.9:** Simple shear deformation: (a) Average normalized particle overlap $\Delta\bar{u}_n$ and (b) average particle rotation $\bar{\theta}$ versus the shear deformation $\bar{F}_{12}$ for a packing of 228 particles subjected to the (D), (P) and (T) boundary conditions.

#### 2.4.2.2 Convergence behavior of macroscopic response under increasing sample size

The convergence behavior of the apparent macroscopic response of the particle aggregate towards its effective response under increasing sample size is studied by subjecting the five micro-structures depicted in Figure 2.6(b) to a simple shear deformation given by (2.40). In convergence studies, this type of loading condition occasionally is characterized as "critical", because of a relatively slow convergence behavior towards a representative volume element (RVE). The convergence behavior is evaluated here by means of the $L_2$-norm of the normalized, homogenized Cauchy stress tensor $\tilde{\boldsymbol{\sigma}}$, integrated along the entire deformation path

$$\|\tilde{\sigma}\|_{L_2} = \left( \sum_{ij=11,22,12,21} \int_{\bar{F}_{12}=0}^{\bar{F}_{12}=0.5} \tilde{\sigma}_{ij}^2 \mathrm{d}\bar{F}_{12} \right)^{1/2} . \tag{2.42}$$

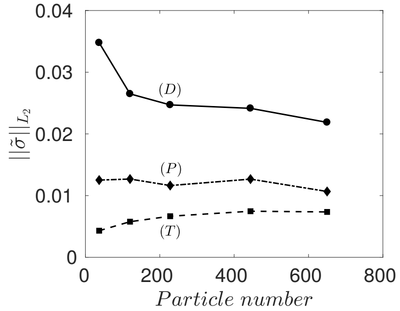

**Figure 2.10:** Stress norm $\|\tilde{\sigma}\|_{L_2}$ versus particle number for irregular polydisperse particle packings subjected to (D), (P) and (T) boundary conditions, in accordance with a macroscopic simple shear deformation $\bar{F}_{12} = 0.5$.

Figure 2.10 illustrates the stress norm $\|\tilde{\sigma}\|_{L_2}$ as a function of the sample size, expressed in terms of the number of particles. It can be observed that for the stiff (D) and soft (T) boundary conditions the stress norm, respectively, decreases and increases with increasing sample size, while for the periodic (P) boundary condition it remains approximately constant. These trends are typical for a change in apparent properties under increasing sample size, see e.g., (Kouznetsova et al., 2001). However, to define the minimal RVE the curves for the (D) (P) and (T) boundary conditions must coincide (Hill, 1963), which indeed is not the case for the largest sample of 650 particles. As already indicated above, the minimum size of RVE depends on the type of loading condition applied, which is known to be relatively large under a macroscopic shear deformation. From the approximately constant stress value observed in Figure 2.10 for the (P) boundary condition, it may be expected that the stress response of the RVE will be close to $\|\tilde{\sigma}\|_{L_2} \approx 0.011$. Hence, in multi-scale simulations on granular materials the computational costs can be kept manageable by adopting the (P) boundary condition for a relatively small (and thus not rigorously "representative") micro-structural sample. Its effective response in fact is comparable to that of the minimal RVE, which thus is typically characterized by a much larger size.

## 2.5 Mixed boundary conditions

In this section the formulation and numerical implementation of *mixed* (D)-(P)-(T) *boundary conditions* is presented. Despite that the classical boundary conditions accurately represent the response of granular assemblies for the specific conditions under which they apply, for simulating more generally the effect of a macroscopic deformation on the particle micro-structure and to accurately represent the loading conditions in particular experimental set-ups, a combination of the classical boundary conditions may be needed. The homogenization framework proposed here satisfies the Hill-Mandel micro-heterogeneity condition, and thus can be used for i) a consistent derivation of macro-scale constitutive relations from standard material tests on micro-scale particle aggregates subjected to any combination of (D)-, (P)- and/or (T)-type boundary conditions, and ii) the efficient computation of the homogenized response of large-scale particle aggregates characterized by a spatial periodicity in one or two directions, i.e., granular layers exposed to uniform (D) and/or (T) boundary conditions at their top and bottom surfaces. To the best of the authors' knowledge, the formulation presented is novel in the field of granular materials.

### 2.5.1 Formulation

For the formulation of the mixed boundary conditions, the basic particle configuration sketched in Figure 2.1 is considered, with the boundary being split up into the top part $\partial V_t$, the bottom part $\partial V_b$, the left part $\partial V_l$ and the right part $\partial V_r$. It is emphasized that the main concepts of the mixed formulation are general, and can be applied to arbitrary boundary value problems. The concepts are elaborated here for the specific case of an infinite horizontal layer of particles loaded by a constant vertical pressure, $\bar{P}_{22} = \bar{P}^*_{22}$, and subsequently subjected to a shear deformation $\bar{F}_{12}$ in the horizontal direction. The reason for choosing this boundary value problem is that it includes all the three (D), (P) and (T) boundary conditions discussed previously, with their combinations entering the formulation both at *separate* and *identical* parts of the layer boundary. This allows for highlighting the characteristics of the mixed formulation in full detail. Accordingly, the macroscopic deformation of the particle aggregate is imposed via a *combined* (D)-(T) condition

$$x_{q,1} = \bar{F}_{12} X_{q,2} + X_{q,1} \qquad \text{and} \qquad a_{q,2} = \bar{P}_{21} A_{q,1} + \bar{P}^*_{22} A_{q,2}\,, \tag{2.43}$$

in which the macroscopic shear stress $\bar{P}_{21}$ is measured from the response of the particle assembly. Note that $(2.43)_1$ implicitly accounts for the condition

$$\bar{F}_{11} = 1\,. \tag{2.44}$$

Furthermore, the first contribution in the right-hand side of $(2.43)_2$ typically is relatively small, since most particles $q$ at the top boundary $\partial V_t$ are characterized by $A_{q,1} << A_{q,2}$, with $A_{q,1}$ vanishing for the specific case of an ideally horizontal boundary composed of identical particles. Since the shear deformation $\bar{F}_{12}$ is imposed *after* the application of the vertical stress $\bar{P}^*_{22}$, in $(2.43)_1$ the reference positions $\boldsymbol{X}_q$ of the boundary particles relate to the particle configuration obtained after the vertical stress has been applied. In summary, the boundary conditions for the particle aggregate are specified as follows:

- For the particles that are part of the bottom boundary, $q \in \partial V_b$, the homogeneous deformation and zero rotation boundary condition (D) is applied in accordance with expression (2.17). The vertical boundary displacements are constrained to construct a rigid support for the layer, and the horizontal boundary displacements follow the shear deformation given by expression $(2.43)_1$.

- For the particles that are part of the left and right boundaries, $q \in \partial V_l \cup \partial V_r$, the periodic displacement and periodic rotation boundary condition (P) is applied, as given by expression (2.19). This boundary condition reflects the horizontal confinement of the particles within the infinite layer.

- For the particles that are part of the top boundary, $q \in \partial V_t$, free rotations are assumed, in correspondence with the (T) boundary condition[2]. For the description of the particle displacements, the boundary is split up along the two orthonormal directions $\mathbf{e}_1$ and $\mathbf{e}_2$ indicated in Figure 2.1. Along the $\mathbf{e}_1$-direction, the (D) boundary condition $(2.43)_1$ is applied to simulate the horizontal macroscopic shear deformation. Along the $\mathbf{e}_2$-direction, a constant macroscopic pressure $\bar{P}^*_{22}$ is imposed via the (T) boundary condition $(2.43)_2$, for which the corresponding components of the macroscopic deformation gradient, $\bar{F}_{21}$ and $\bar{F}_{22}$, in accordance with the general form (2.15), turn into

  $$\bar{F}_{21} = \frac{1}{V}\sum_{q=1}^{Q} x_{q,2}A_{q,1} \quad \text{and} \quad \bar{F}_{22} = \frac{1}{V}\sum_{q=1}^{Q} x_{q,2}A_{q,2}\,. \tag{2.45}$$

  Note that the two deformation components above should be considered as a computational *result* obtained by prescribing the stress component $\bar{P}^*_{22}$.

The macroscopic deformation gradient $\bar{\boldsymbol{F}}$, which is followed by the four corner nodes of the sample, now is fully specified through its "(D)-type components" provided by $(2.43)_1$ and (2.44), and its "(T)-type components" given by $(2.45)_{1,2}$.

---

[2] Since the top boundary is subjected to a mixed (D)-(T) boundary condition, instead of leaving the particle rotations free at the boundary, i.e., a (T)-type condition, the particle rotations could have been equally well taken as fully constrained, i.e., a (D)-type condition. For relatively large samples the effect of this choice on the homogenized response of the particle aggregate is expected to be minor.

The corresponding macroscopic Piola-Kirchhoff stress tensor is defined by equation (2.23). For the adopted mixed-boundary conditions it will now be demonstrated that this stress definition satisfies the recast Hill-Mandel condition given by expression (2.30), i.e., the energy consistency between the macro- and micro scales. Accordingly, relation (2.30) is first split up with respect to the different boundary parts considered above, i.e.,

$$\begin{aligned} \sum_{q\in\partial V_b} \left(\mathbf{a}_q - \bar{\boldsymbol{P}}\cdot\mathbf{A}_q\right)\cdot\delta\mathbf{w}_q + \sum_{q\in\partial V_l\cup\partial V_r} \left(\mathbf{a}_q - \bar{\boldsymbol{P}}\cdot\mathbf{A}_q\right)\cdot\delta\mathbf{w}_q \\ + \sum_{q\in\partial V_t} \left(\mathbf{a}_q - \bar{\boldsymbol{P}}\cdot\mathbf{A}_q\right)\cdot\delta\mathbf{w}_q = 0\,. \end{aligned} \tag{2.46}$$

For the bottom boundary $\partial V_b$, boundary condition (D) holds, which, by comparing equations (2.17) and (2.14), lets the micro-fluctuations of the displacements vanish, $\mathbf{w}_q = \mathbf{0}$. Hence, the first term in (2.46) is equal to zero. At the left and right boundaries $q \in \partial V_l \cup \partial V_r$, the (P) boundary condition is imposed, for which the micro-fluctuations of the displacements are periodic, $\mathbf{w}_q^l = \mathbf{w}_q^r$, see (2.14) and (2.19). Together with the anti-periodicity of the boundary forces $\mathbf{a}_q^l + \mathbf{a}_q^r = \mathbf{0}$, see (2.20), the second term in (2.46) vanishes. Finally, for the top boundary $\partial V_t$, the last term in (2.46) may be further developed as

$$\sum_{q\in\partial V_t} \left[\left(a_{q,1} - \bar{P}_{1j}A_{q,j}\right)\delta w_{q,1} + \left(a_{q,2} - \bar{P}_{2j}A_{q,j}\right)\delta w_{q,2}\right] = 0\,. \tag{2.47}$$

Along the $\mathbf{e}_1$-direction, the micro-fluctuations of the boundary particle displacements vanish, $w_{q,1} = 0$, in correspondence with equation $(2.43)_1$, by which the first term in (2.47) becomes zero. Along the $\mathbf{e}_2$-direction, the boundary forces are uniform, $a_{q,2} - \bar{P}_{2j}A_{q,j} = 0$, see equation $(2.43)_2$, so that the second term in (2.47) becomes zero. With this result, the Hill-Mandel condition (2.46) is proven to be satisfied for the mixed boundary conditions.

### 2.5.2 Numerical implementation

The numerical algorithm for the implementation of the mixed boundary conditions is outlined in Table 2.5, and is based on a combination of the algorithms presented in Section 2.3 for the (D), (P) and (T) boundary conditions, without an initial displacement prediction.

During *stage 1* of the loading process, the vertical compressive stress $\bar{P}_{22} = \bar{P}_{22}^*$ is applied to the particle aggregate in a stepwise fashion[3], using a total of $i_{vs}$ loading increments, with the subscript $vs$ designating "vertical stress". After initiating the displacement and rotation boundary conditions at the top $\partial V_t$ and bottom $\partial V_b$

---

[3] Instead of applying the vertical compressive stress by means of the first Piola-Kirchhoff stress $\bar{P}_{22}$, the Cauchy stress $\bar{\sigma}_{22}$ could have been used. The conversion of the Cauchy stress into the first Piola-Kirchhoff stress, which is the stress measure used in the numerical algorithm presented in Table 2.5, can straightforwardly be accomplished by using the inverse form of expression (2.31).

boundaries, the vertical stress is incrementally updated and subsequently used to compute the displacement and rotation corrections at the left and right boundaries with expressions (2.32)-(2.33), and the displacement correction at the top boundary boundary with

$$\Delta u_{q,2} = g_a^t \Delta a_{q,2} \qquad \text{with} \qquad \Delta a_{q,2} = \bar{P}_{21} A_{q,1} + \bar{P}_{22}^* A_{q,2} - a_{q,2} \, . \tag{2.48}$$

The expression above is derived from $(2.43)_2$, whereby during the incremental application of the vertical stress $\bar{P}_{22}^*$ the value of $\bar{P}_{21}$ is prescribed as zero, in order to avoid the initial development of a shear stress. After the particle aggregate has reached its equilibrium state under dynamic relaxation, the boundary forces and moments of the particles at the top, left and right boundaries are recorded and employed to compute the corresponding residuals. When all residuals are lower than the prescribed values of the corresponding tolerances, the iterative loop is stopped and the next vertical stress increment is applied. Otherwise, the iterative loop is entered again, until a converged solution is found. After the application of $i_{vs}$ increments the vertical stress has reached the desired value, and stage 1 of the loading process has completed.

During *stage 2* of the loading process, the horizontal shear deformation $\bar{F}_{12}$ is imposed on the particles at the top $\partial V_t$ and bottom $\partial V_b$ boundaries of the granular assembly, by displacing these in a stepwise manner using $i_{tot} - i_{vs}$ increments. The rotations of the particles at the top boundary are free, and the vertical displacement and rotation of the particles at the bottom boundary are fully constrained. In a similar way as explained above for stage 1, the boundary forces and moments in the relaxed equilibrium state are used to compute the displacement and rotation corrections at the periodic left and right boundaries $\partial V_l$ and $\partial V_r$, and at the top boundary boundary $\partial V_t$. However, the only difference is that in (2.48) the shear stress $\bar{P}_{21}$ here is not prescribed as zero, but is calculated from the homogenized response of the particle assembly using equation (2.23). After the dynamic relaxation procedure has completed, the residuals are computed in the same way as during stage 1, and compared against the corresponding tolerances. The iterative process is terminated when the convergence criterion is satisfied, after which the shear deformation is incremented and the response to the next loading step is computed. This procedure is continued until all loading increments $i_{tot}$ are applied.

**Table 2.5:** Algorithm for the application of the mixed boundary conditions. The loading process consists of stage 1, during which the vertical stress is incrementally applied, and stage 2, during which the horizontal shear deformation is incrementally imposed.

**Algorithm for mixed boundary conditions**

```
1. DEM simulation. Apply vertical stress. Increments $0 \leq i \leq i_{vs}$
    1.1 Apply boundary conditions
        1.1.A $q \in \partial V_t \Longrightarrow$ Free rotations $\boldsymbol{m}_q = \mathbf{0}$
        1.1.B $q \in \partial V_b \Longrightarrow$ Zero vertical displacements $x_{q,2} = 0$ and zero rotations $\mathbf{Q}_q = \mathbf{I}$
    1.2 Update vertical stress $\bar{P}_{22} = \bar{P}_{22}^*$
    1.3 Update particle configuration
        1.3.A $q \in \partial V_t \Longrightarrow$ Calculate particles displacement correction $\Delta u_{q,2}$ via (2.48), with $\bar{P}_{21} = 0$
        1.3.B $q \in \partial V_l \cup \partial V_r \Longrightarrow$
                Calculate particles displacement $\Delta \mathbf{u}_q$ and rotation $\Delta \theta_q$ corrections via (2.32)-(2.33)
    1.4 Dynamic relaxation until equation (2.11) is reached. Obtain boundary forces and moments.
    1.5 Calculate residual(s)
        1.5.A $q \in \partial V_t \Longrightarrow r_a^t = \sqrt{\sum_{q \in \partial V_t} \Delta a_{q,2}{}^2 / \tilde{a}_q^2}$
        1.5.B $q \in \partial V_l \cup \partial V_r \Longrightarrow r_a^p = \sqrt{\sum_{q \in \partial V_l \cup \partial V_r} \Delta \mathbf{a}_q \cdot \Delta \mathbf{a}_q / \tilde{a}_q^2}$ and
                $r_m^p = \sqrt{\sum_{q \in \partial V_l \cup \partial V_r} (\Delta m_q / \tilde{m}_q)^2}$
    1.6 Check for convergence: $r_a^t \leq \epsilon_a^t$ and $r_a^p \leq \epsilon_a^p$ and $r_m^p \leq \epsilon_m^p$
        1.6.A if converged $\Longrightarrow$ Save current configuration and go to 1 (next increment $i + 1$)
        1.6.B if not converged $\Longrightarrow$ Return to 1.3

2. Apply horizontal shear deformation at fixed vertical stress. Increments $i_{vs} < i \leq i_{tot}$
    2.1 Apply updated macro-scale deformation and boundary conditions
        2.1.A $q \in \partial V_t \Longrightarrow$ Horizontal displacements $x_{q,1} = \bar{F}_{12} X_{q,2} + X_{q,1}$ and free rotations $\boldsymbol{m}_q = \mathbf{0}$
        2.1.B $q \in \partial V_b \Longrightarrow$ Zero vertical displacements $x_{q,2} = 0$ and zero rotations $\mathbf{Q}_q = \mathbf{I}$
                Horizontal displacements $x_{q,1} = \bar{F}_{12} X_{q,2} + X_{q,1}$
    2.2 Dynamic relaxation until equation (2.11) is satisfied. Obtain boundary forces and moments.
    2.3 Update particle configuration
        2.3.A $q \in \partial V_t \Longrightarrow$ Calculate particles displacement correction $\Delta u_{q,2}$ via (2.48)
        2.3.B $q \in \partial V_l \cup \partial V_r \Longrightarrow$
                Calculate particles displacement $\Delta \mathbf{u}_q$ and rotation $\Delta \theta_q$ corrections via (2.32)-(2.33)
    2.4 Dynamic relaxation until equation (2.11) is satisfied. Obtain boundary forces and moments.
    2.5 Calculate residual(s)
        2.5.A $q \in \partial V_t \Longrightarrow$ Refer to 1.5.A
        2.5.B $q \in \partial V_l \cup \partial V_r \Longrightarrow$ Refer to 1.5.B
    2.6 Check for convergence: $r_a^t \leq \epsilon_a^t$ and $r_a^p \leq \epsilon_a^p$ and $r_m^p \leq \epsilon_m^p$
        2.6.A if converged $\Longrightarrow$ Save current configuration and go to 2 (next increment $i + 1$)
        2.6.B if not converged $\Longrightarrow$ Return to 2.3
```

## 2.5.3 Computational results

The performance of the algorithm used for the implementation of the mixed boundary conditions is demonstrated by means of two DEM simulations of an irregular polydisperse packing of $449$ particles, with the particle radii taken randomly from a uniform size distribution with polydispersity $R_{max}/R_{min} = 1.5$, where the minimum radius equals $R_{min}= 0.8$ mm. The initial particle volume is $V = 1517$ mm$^2$, with the particle volume fraction of the packing being equal to $\mathfrak{v} = 0.849$, and the average particle coordination number as $3.55$. The two simulations consider different particle contact laws, namely the frictional contact law and the cohesive contact law described in Section 2.2.2.2. The model parameters are summarized in Table 2.6. Assuming relatively hard particles, the normal and tangential contact stiffnesses for the frictional contact law are set as $k_n = 10^5$ N/mm and $k_s = 4 \cdot 10^4$ N/mm, respectively, and the friction coefficient equals $\mu = 0.6$. The normal contact stiffness $k_n^b$ and the tangential contact stiffness $k_s^b$ for the cohesive contact interaction are assumed to be equal to those of the frictional contact law, and the bending contact stiffness is taken as $k_\theta^b = 2 \cdot 10^4$ Nmm. The normal, shear and bending strengths have the values $f_n^{b,u} = 300$ N, $f_s^{b,u} = 60$ N and $m_\theta^{b,u} = 200$ Nmm, respectively. The density of the particles is $\rho = 10 \cdot 10^3$ kg/m$^2$. The macroscopic vertical (compressive) stress is $\bar{P}_{22}^* = -1.05 \cdot 10^6$ N/m, which is applied in $i_{vs} = 6$ increments. The total macroscopic shear deformation equals $\bar{F}_{12} = 0.2$, which is imposed on the particle aggregate in $i_{tot} - i_{vs} = 100$ increments. The translational and rotational

**Table 2.6:** Physical and algorithmic model parameters for the simulations with mixed boundary conditions.

| **Parameter** | **Value** | **Unit** |
|---|---|---|
| Elastic normal stiffness $k_n = k_n^b$ | $1 \times 10^5$ | N/mm |
| Elastic tangential stiffness $k_s = k_s^b$ | $4 \times 10^4$ | N/mm |
| Elastic bending stiffness $k_\theta^b$ | $2 \times 10^4$ | Nmm |
| Friction coefficient $\mu$ | 0.6 | - |
| Cohesive normal strength $f_n^{b,u}$ | 300 | N |
| Cohesive tangential strength $f_s^{b,u}$ | 60 | N |
| Cohesive bending strength $m_\theta^{b,u}$ | 200 | Nmm |
| Density $\rho$ | $10 \times 10^3$ | kg/m$^2$ |
| Translational damping $\alpha$ | 0.7 | - |
| Rotational damping $\beta$ | 0.7 | - |
| Time increment $\Delta t$ | $10^{-5}$ | s |
| Tolerance force (P) $\epsilon_a^p$ | $2 \times 10^{-10}$ | - |
| Tolerance moment (P) $\epsilon_m^p$ | $2 \times 10^{-10}$ | - |
| Tolerance force (T) $\epsilon_a^t$ | $2 \times 10^{-10}$ | - |
| Gain force (P) $g_a^p M_i/\Delta t^2$ | $3 \times 10^4$ | - |
| Gain moment (P) $g_m^p M_i R_i^2/\Delta t^2$ | $6 \times 10^4$ | - |
| Gain force (T) $g_a^t M_i/\Delta t^2$ | $3 \times 10^4$ | - |
| Tolerance dynamic relaxation $\mathrm{tol}_E$ | $10^{-3}$ | - |

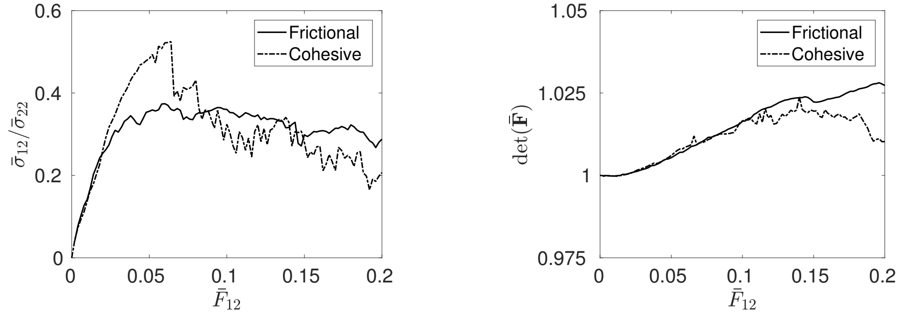

(a) Stress ratio $\bar{\sigma}_{12}/\bar{\sigma}_{22}$ (b) Relative volumetric change $\det(\bar{\boldsymbol{F}})$

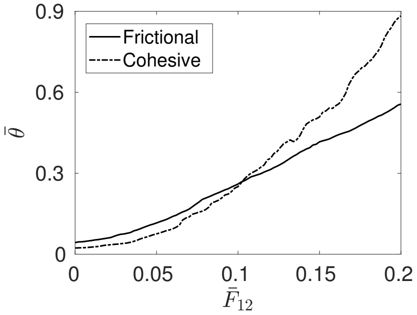

(c) Average particle rotation $\bar{\theta}$

**Figure 2.11:** Macroscopic response of an infinite granular layer subjected to a vertical compressive stress $\bar{P}_{22} = \bar{P}^*_{22}$ and a horizontal shear deformation $\bar{F}_{12}$. (a) Stress ratio $\bar{\sigma}_{12}/\bar{\sigma}_{22}$, (b) relative volumetric change $\det(\bar{\boldsymbol{F}})$, and (c) average particle rotation $\bar{\theta}$, all plotted versus the applied shear deformation $\bar{F}_{12}$ for cohesive (dot-dashed line) and frictional (solid line) packings.

damping factors used in the dynamic relaxation procedure are $\alpha = \beta = 0.7$, and the time increment equals $\Delta t = 10^{-5}$ s. The dimensionless values of the gain parameters are $g^t_a M_i/\Delta t^2 = g^p_a M_i/\Delta t^2 = 3 \cdot 10^4$ and $g^p_m M_i R^2_i/\Delta t^2 = 6 \cdot 10^4$, and the corresponding tolerances are equal to $\epsilon^t_a = \epsilon^p_a = \epsilon^p_m = 2 \cdot 10^{-10}$.

Figure 2.11 shows the macroscopic response of the particle aggregates as a function of the applied shear deformation $\bar{F}_{12}$, with the dot-dashed and solid lines referring to packings with cohesive and frictional particle contact interactions, respectively. In Figure 2.11(a) the stress ratio $\bar{\sigma}_{12}/\bar{\sigma}_{22}$ is depicted, while Figure 2.11(b) illustrates the relative volumetric change $\det(\bar{\boldsymbol{F}})$ (using the packing obtained after the application of the vertical stress as the reference state), and Figure 2.11(c) sketches the average particle rotation $\bar{\theta}$, in accordance with expression (2.41). Furthermore, in Figure 2.12 the particle configurations of the cohesive and frictional packings are plotted at four different deformation levels, namely (a) $\bar{F}_{12} = 0.002$, (b) $\bar{F}_{12} = 0.05$, (c) $\bar{F}_{12} = 0.1$ and (d) $\bar{F}_{12} = 0.015$. Here, the red lines between the particles represent cohesive contact forces, while the blue lines

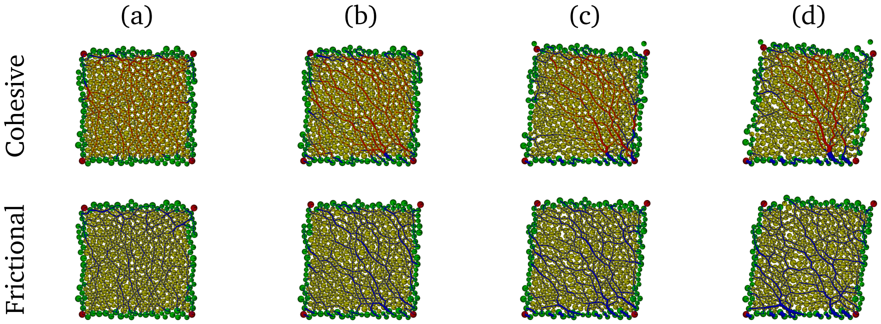

**Figure 2.12:** Deformed configurations of a packing with 449 particles corresponding to (a)$\bar{F}_{12} = 0.002$, (b) $\bar{F}_{12} = 0.05$, (c) $\bar{F}_{12} = 0.1$ and (d) $\bar{F}_{12} = 0.15$, for cohesive (top) and frictional (bottom) particle contact interactions. The networks of cohesive and frictional forces acting between particles are indicated by the red and blue lines, respectively.

indicate frictional contact forces. It can be observed from Figure 2.11(a) that up to a deformation $\bar{F}_{12} = 0.02$ the cohesive and frictional packings show a similar response, whereby the stress increases approximately proportionally with deformation. Upon continuing deformation, in the frictional packing a large number of contacting particles meet the failure criterion (2.6) and start to slide, such that the stress ratio $\bar{\sigma}_{12}/\bar{\sigma}_{22}$ reaches a maximum at $\bar{F}_{12} \approx 0.06$. The maximal stress ratio is accompanied by a volumetric increase of the particle structure, commonly referred to as “dilation”, see Figure 2.11(b). After passing the peak value, the stress ratio for the frictional packing slightly drops in magnitude, which is caused by a substantial rolling of particles. The effect of particle rolling can be clearly observed from Figure 2.11(c), where at the onset of shear deformation the increase in average particle rotation only is mild, but steadily grows towards a more or less constant value at $\bar{F}_{12} = 0.07$ for the frictional packing and at $\bar{F}_{12} = 0.12$ for the cohesive packing. Note from Figure 2.11(c) that the initial value of the average particle rotation is due to the application of the vertical stress $\bar{P}^{*}_{22}$, and for the frictional packing appears to be somewhat larger than for the cohesive packing. For the cohesive packing the maximal value of the stress ratio $\bar{\sigma}_{12}/\bar{\sigma}_{22}$ is about 1.5 times larger than for the frictional packing, and is reached at $\bar{F}_{12} \approx 0.07$, see Figure 2.11(a). At this stage a significant number of particle bonds are broken, in correspondence with the failure criterion (2.8). With continuing deformation, the broken particle bonds of the cohesive packing become frictional, as indicated by the thick blue lines in Figure 2.12(c), whereby the stress ratio $\bar{\sigma}_{12}/\bar{\sigma}_{22}$ of the packing drops to a level comparable to that of the frictional packing, see Figure 2.11(a). Observe from Figures 2.12(c) and (d) that for the cohesive packing the frictional contacts indicated by the blue lines are established only along local force chains in the particle structure, whereby the rest of the contacts remain cohesive, as indicated by the red lines. This implies that the overall deformation of the packing near the end of the loading process becomes governed by a localized failure zone, which indeed is associated to a strong softening behavior in the stress response, see Figure 2.11(a). Towards a shear deformation of $\bar{F}_{12} = 0.20$, both the stress ratio $\bar{\sigma}_{12}/\bar{\sigma}_{22}$ and the relative volumetric change $\det(\bar{\boldsymbol{F}})$ of the frictional and cohesive packings become approximately constant, characterizing the occurrence of a so-called "critical state". For the frictional packing the overall residual strength at the critical state is $\bar{\sigma}_{12}/\bar{\sigma}_{22} \approx 0.28$. This value is only about half of the value of 0.6 adopted for the local particle contact friction $\mu$, which can be explained from the fact that at the end of the deformation process the dilating particle structure, instead of sliding, is predominated by a relatively easy rolling of particles, see (Suiker and Fleck, 2004) for a more detailed discussion on this aspect. For the same reason, the eventual, large amount of particle rolling generated in the cohesive packing, see Figure 2.11(c), leads to a final residual strength that is lower than for the frictional packing, see Figure 2.11(a).

As a final note, it is mentioned that the contact moments in the cohesive packing determine about $10\%$ of the total potential energy. This contribution implicitly contributes to the stress ratio $\bar{\sigma}_{12}/\bar{\sigma}_{22}$ depicted in Figure 11(a) by means of moment equilibrium at the particle level. More specifically, for each particle the corresponding contact moments are balanced by the product of the contact shear forces and the particle radius, whereby contact shear forces contribute to the effective Cauchy stress in accordance with expressions (23) and (31).

## 2.6 Conclusions

Novel numerical algorithms have been presented for the implementation of three types of classical boundary conditions for a particle aggregate. The micro-scale boundary conditions are formulated within the discrete element method using large deformation theory, and, along the lines of (Miehe et al., 2010), are imposed on a frame of boundary particles of the particle packing, in accordance with i) a homogeneous deformation and zero particle rotation (D), ii) a periodic particle displacement and rotation (P), and iii) a uniform particle force and free particle rotation (T). The algorithms can be straightforwardly combined with commercial discrete element codes, thereby enabling the determination of the solution of boundary-value problems at the micro-scale only, or at multiple scales via a micro-to-macro coupling with a finite element model. The performance of the algorithms has been tested by means of discrete element method simulations on regular monodisperse packings and irregular polydisperse packings composed of frictional particles, which were subjected to various loading paths. The simulations provide responses with the typical stiff and soft bounds for the (D) and (T) boundary conditions, respectively, and illustrate for the (P) boundary condition a relatively fast convergence of the apparent macroscopic properties under an increasing packing size. Finally, a homogenization framework has been presented for the formulation of mixed (D)-(P)-(T) boundary conditions that satisfy the Hill-Mandel micro-heterogeneity condition on energy consistency at the micro-and macro-scales of the granular system. The numerical algorithm for mixed boundary conditions has been developed and tested for the case of an infinite layer subjected to a vertical compressive stress and a horizontal shear deformation, whereby the response computed for a layer of cohesive particles is compared against that for a layer of frictional particles. The results illustrate that the failure response for both contact laws is characterized by the development of a dilated particle structure, which at large deformation gradually turns into a critical state with an approximately constant residual strength and specific volume. The application of the present algorithms for multi-scale FEM-DEM analyses on granular systems with a large number of particles, and their extension towards a dynamics homogenization framework, are topics for future studies.

# Chapter 3

# Multi-scale quasi-static simulation[1]

A multi-scale model for the analysis of granular systems is proposed, which combines the principles of a coupled FEM-DEM approach with a novel servo-control methodology for the implementation of appropriate micro-scale boundary conditions. A mesh convergence study is performed, whereby the results of a quasi-static biaxial compression test are compared with those obtained by direct numerical simulations. The comparison demonstrates the capability of the multi-scale method to realistically capture the macro-scale response, even for macroscopic domains characterized by a relatively coarse mesh; this makes it possible to accurately analyse large-scale granular systems in a computationally efficient manner. The multi-scale framework is applied to study in a systematic manner the role of individual micro-structural characteristics on the effective macro-scale response. The effect of particle contact friction, particle rotation, and initial fabric anisotropy on the overall response is considered, as measured in terms of the evolution of the effective stress, the volumetric deformation, the average coordination number and the induced anisotropy. The trends observed are in accordance with notions from physics, and observations from experiments and other DEM simulations presented in the literature. Hence, it is concluded that the present framework provides an adequate tool for exploring the effect of micro-structural characteristics on the macroscopic response of large-scale granular structures.

---

[1] Based on Liu, J., Bosco, E. and Suiker, A.S.J. , Multi-scale modelling of granular materials: numerical framework and study on micro-structural features. Computational Mechanics, 2018. https://doi.org/10.1007/s00466-018-1600-y.

## 3.1 Introduction

The intrinsic influence of the discrete micro-structure of granular materials on their effective material properties and structural response is nowadays well recognized. The morphology, material evolution and mechanical interactions at the particle scale all contribute to the observed macroscopic non-linear failure and deformation behaviour. Multi-scale approaches provide an ideal tool for the modelling of granular systems, as they allow to directly incorporate the complex behaviour of the discrete micro-structure into the response of large-scale structural problems. This is typically done by coupling the discrete element method (DEM), which accurately represents the complex particle behaviour at the micro scale (Cundall and Strack, 1979; Herrmann and Luding, 1998; Kun and Herrmann, 1996; Ting et al., 1993; Borja and Wren, 1995; Suiker and Fleck, 2004; Luding, 2004; Luding and Suiker, 2008; Wellmann et al., 2008; Singh et al., 2014; Nitka and Tejchman, 2015; Zhu et al., 2016; Huang et al., 2017; Zhao et al., 2018), to the finite element method (FEM), which enables to efficiently solve boundary value problems at the macro scale. As a general principle, each integration point in the macro-scale FEM model is connected to a corresponding DEM micro-scale model via the application of adequate homogenization relations. In specific, a macroscopic deformation measure is imposed on the granular micro-structure through the definition of appropriate boundary conditions (Miehe et al., 2010; Liu et al., 2017). The DEM model is solved in turn, providing the particle contact forces in the granular assembly. These forces are subsequently translated into a macroscopic stress measure, which is required to solve the boundary value problem at the structural level. Several examples of coupled FEM-DEM approaches for granular materials have been presented in the literature. In (Nguyen et al., 2013; Shahin et al., 2016) a quasi-static multi-scale method is formulated within the framework of small deformations, whereby the role of the particle microstructure on the effective frictional failure response of macroscopic samples is analysed, with a special focus on the initiation of strain localization. In (Guo and Zhao, 2014) a small-strain multi-scale framework is proposed that elegantly computes the mechanical response for various monotonic and cyclic loading problems, whereby drained as well as undrained conditions are considered. In (Guo and Zhao, 2016b) this framework is applied for developing multi-scale insights into classical geomechanical problems, such as retaining wall and footing problems. Coupled FEM-DEM approaches are typically validated by analysing the macroscopic structural response in experimental tests typical for granular media, such as a biaxial compression test (Miehe et al., 2010; Guo and Zhao, 2014; Kaneko et al., 2003; Andrade et al., 2011; Nguyen et al., 2014), a slope stability test (Meier et al., 2009), or a (cyclic) shear test (Guo and Zhao, 2014).

In the current chapter a novel multi-scale framework is presented for granular materials, which employs the formulation and implementation of the micro-scale boundary conditions recently published in (Liu et al., 2017). This formulation is based on the first-order homogenization approach originally proposed in (Miehe et al., 2010), which includes important aspects that are usually ignored in other homogenization methods for particle systems, namely *i)* the Hill-Mandel micro-heterogeneity condition that enforces consistency of energy at the micro- and macro scales, *ii)* the influence of particle rotations in the formulation of micro-to-macro scale transitions, and *iii)* a rigorous generalization of the multi-scale relations within the theory of finite deformations. The implementation of the micro-scale boundary conditions is performed with a servo-control algorithm that uses a feedback principle similar to that of algorithms applied in control theory of dynamic systems. The servo-control algorithm has several attractive features compared to other methods used for implementing micro-scale boundary conditions. Firstly, from the computational viewpoint the algorithm is relatively simple to implement. Secondly, it can be implemented at the level of the interface communicating information between the macro-scale FEM and micro-scale DEM models, whereby modifications of the FEM and DEM source codes are not needed. The algorithm can therefore be easily combined with commercial software, whose source codes generally are not available to the user. Thirdly, in contrast to the often-used penalty method, the servo-control methodology preserves the physical meaning of the homogenized stress measure derived from the granular assembly. Further, the limit case at which the micro-scale boundary conditions are met exactly is rigorously retrieved from the formulation, see (Liu et al., 2017) for more details.

The first aim of this chapter is to demonstrate how the servo-control algorithm for the micro-scale boundary conditions can be conveniently incorporated in a multi-scale FEM-DEM framework. Accordingly, the governing equations of the multi-scale framework are formulated, and their numerical implementation is validated by comparing the computational results obtained for a quasi-static biaxial compression test to those calculated by direct numerical simulations. The convergence behaviour of the numerical results under mesh refinement is analysed, and the heterogeneity of the mechanical response across the specimen height is explored. The second aim of this chapter is to show how the FEM-DEM framework can be used for analysing the influence of micro-structural characteristics on the macroscopic response of a granular system. Using the biaxial compression test, the microscopic properties selected for the variation study are the particle contact friction, the particle rotation and the initial fabric anisotropy. The influence of these properties on the overall, macroscopic response is analysed by computing the evolution of the effective stress, the volumetric deformation, the average coordination number, and the induced fabric anisotropy. This study is essential for gaining confidence in the quality of the multi-scale formulation; nonetheless, most other works on coupled FEM-DEM modelling do not consider such a study, but refer to a specific example simulation for the validation of the proposed method.

This chapter is organized as follows. Section 3.2 presents the numerical homogenization framework for particle aggregates by defining the macro-scale and micro-scale models and the scale transition relations. Section 3.3 discusses numerical implementation aspects. The explicit time integration scheme adopted for the macro-scale problem is outlined, and details are provided on the dynamic relaxation procedure applied for satisfying the equilibrium conditions, and on the servo-control algorithm used for defining the boundary conditions at the micro scale. The section ends with a presentation of the coupled FEM-DEM solution algorithm. In Section 3.4, the performance of the proposed multi-scale framework is analysed for a biaxial compression test by comparing the computational results to those obtained by direct numerical simulations. A mesh convergence study is performed, and the role of several micro-structural parameters on the macroscopic response is studied. Some concluding remarks are provided in Section 3.5.

In this chapter the following notations will be used. The cross product and dyadic product of two vectors are denoted as $\mathbf{a} \times \mathbf{b} = e_{ijk} a_i b_j \mathbf{e}_k$ and $\mathbf{a} \otimes \mathbf{b} = a_i b_j \mathbf{e}_i \otimes \mathbf{e}_j$, respectively. Here $e_{ijk}$ is the permutation symbol, $\mathbf{e}_i$, $\mathbf{e}_j$ and $\mathbf{e}_k$ are unit vectors in a Cartesian vector basis, and Einstein's summation convention is used on repeated tensor indices. The inner products between two vectors and two second-order tensors are given by $\mathbf{a} \cdot \mathbf{b} = a_i b_i$ and $\mathbf{A} : \mathbf{B} = A_{ij} B_{ij}$, respectively. The action of a second-order tensor on a vector is indicated as $\mathbf{A} \cdot \mathbf{b} = A_{ij} b_j \mathbf{e}_i$. The symbol $\nabla$ indicates the gradient operator with respect to the reference configuration, and $|.|$ refers to the absolute value of a variable. Occasionally, field variables referring to the macroscopic scale are indicated by an overbar, for instance $\bar{\mathbf{F}}$, in order to avoid misinterpretation.

The present study focuses on two-dimensional particle aggregates. Accordingly, the dimensions related to volume, area, stress and mass density are consistently presented in their reduced form as length$^2$, length, force/length and mass/length$^2$, respectively.

## 3.2 Multi-scale framework for particle aggregates

This section treats the main principles of a multi-scale homogenization strategy for granular structures. These principles ensue from transforming relevant theorems used in classical first-order homogenization theories (Suquet, 1985; Kouznetsova et al., 2001; Miehe et al., 2002; Terada et al., 2000) from a continuous setting to a discrete setting. For more details on this aspect the reader is referred to (Miehe and Koch, 2002; Dettmar, 2006; Liu et al., 2017).

### 3.2.1 Macro-scale problem

Consider a two-dimensional macroscopic domain with an initial, undeformed volume $\Omega$ and boundary $\partial\Omega$, characterized by a heterogeneous, granular microstructure. The macroscopic domain is subjected to loadings and constraints at the boundaries under which the separation of scales principle holds, i.e., the characteristic length scale of the micro-structure is much smaller than the typical length across which the macroscopic deformation varies. Under this assumption, the macroscopic domain may be considered as a Boltzmann continuum, governed by the classical equilibrium equations:

$$\nabla \cdot \bar{\boldsymbol{P}} + \bar{\mathbf{b}} = \mathbf{0} \qquad \text{and} \qquad \bar{\boldsymbol{F}} \cdot \bar{\boldsymbol{P}}^T - \bar{\boldsymbol{P}} \cdot \bar{\boldsymbol{F}}^T = \mathbf{0} \quad \text{in} \quad \Omega, \tag{3.1}$$

with the boundary conditions

$$\bar{\boldsymbol{P}} \cdot \mathbf{N} = \bar{\mathbf{t}}^* \quad \text{on} \quad \partial\Omega^t \tag{3.2}$$

$$\bar{\mathbf{u}} = \bar{\mathbf{u}}^* \quad \text{on} \quad \partial\Omega^u. \tag{3.3}$$

In equation (3.1), $\bar{\boldsymbol{P}}$ is the first Piola-Kirchhoff stress, $\bar{\mathbf{b}}$ is the body force per unit volume, and $\bar{\boldsymbol{F}} = \nabla(\mathbf{x})$ is the macroscopic deformation gradient, which is a function of the current position $\mathbf{x}$. In relations (3.2) and (3.3) the external traction $\bar{\mathbf{t}}^*$ is imposed on the boundary $\partial\Omega^t$ characterized by the normal direction $\mathbf{N}$, and the displacement $\bar{\mathbf{u}}^*$ is prescribed on the boundary $\partial\Omega^u$.

In order to solve the boundary value problem defined by equations (3.1)-(3.3), a constitutive relation between the stress and the deformation is required. Instead of assuming a phenomenological constitutive equation, a multi-scale procedure is adopted that retrieves the constitutive response numerically from a computational analysis of the granular domain at the micro scale. The main features of the multi-scale scheme are illustrated in Figure 3.1. At each material point the macroscopic deformation gradient $\bar{\boldsymbol{F}}$ is calculated, and subsequently imposed on the corresponding micro-structural domain via appropriate micro-scale boundary conditions. After solving the response of the granular medium at the micro scale, from the particle contact forces at the boundaries the effective macroscopic stress $\bar{\boldsymbol{P}}$ of the particle medium is computed, which is returned to the macro scale to solve the macroscopic equilibrium expressed by equation (3.1).

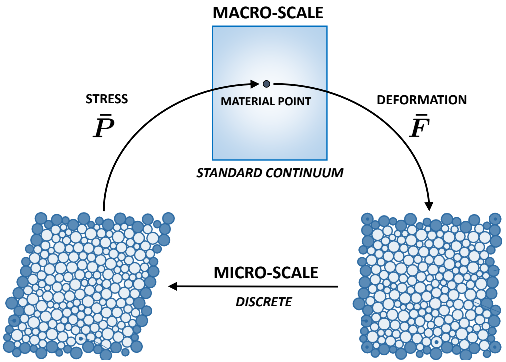

**Figure 3.1:** Schematic overview of the macroscopically continuous-microscopically discrete multi-scale framework.

### 3.2.2 Micro-scale problem

The micro-scale geometry is represented by a two-dimensional square domain composed of $P + Q$ rigid particles. These particles are partitioned into $P$ inner particles $\mathcal{P}_p$ with $p = 1, .., P$, defining the initial interior domain $V$, and $Q$ boundary particles $\mathcal{P}_q$ with $q = 1, .., Q$, defining the undeformed boundary $\partial V$. The boundary particles can be further split into corner particles $\mathcal{P}_c$ with $c = 1, .., 4$ and the remaining edge particles $\mathcal{P}_e$ with $e = 1, .., E = Q - 4$. The reference configuration of the centroids of the inner and boundary particles is denoted by the position vectors $\mathbf{X}_p \in \mathcal{P}_p$ and $\mathbf{X}_q \in \mathcal{P}_q$, respectively. The undeformed micro-scale domain is schematically shown in Figure 3.2(a).

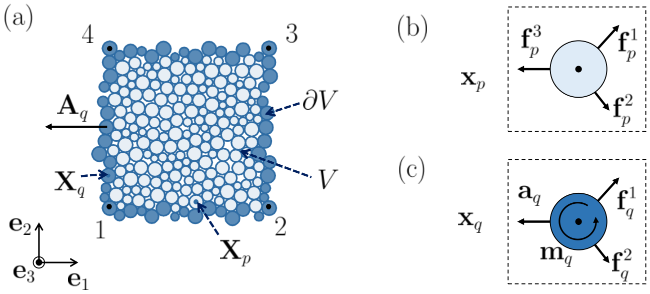

**Figure 3.2:** (a) Two-dimensional particle aggregate of undeformed volume $V$ and boundary $\partial V$. Light blue and blue colors refer to inner $\mathcal{P}_p$ and boundary $\mathcal{P}_q$ particles, respectively; (b) Particle contact forces $\mathbf{f}_p^c$ acting on inner particle $p \in \mathcal{P}_p$ in its current position $\mathbf{x}_p$; (c) Boundary forces $\mathbf{a}_q$, boundary moments $\mathbf{m}_q$, and particle contact forces $\mathbf{f}_q^c$ acting on boundary particle $q \in \mathcal{P}_q$ in its current position $\mathbf{x}_q$.

The effective response of the granular assembly is derived by using classical homogenization principles, in the transition from a continuous to a discrete description. In this perspective, the finite area vector $\mathbf{A}_q$ and the boundary forces $\mathbf{a}_q$ are defined at the centroids of the boundary particles $\mathcal{P}_q$ as

$$\int_{\partial V} \mathbf{N} ds \to \mathbf{A}_q \qquad \text{and} \qquad \int_{\partial V} \mathbf{t}\, ds \to \mathbf{a}_q \qquad \text{for} \qquad q = 1..., Q\,. \tag{3.4}$$

Here, $\mathbf{N}$ is the normal vector associated to the undeformed boundary $\partial V$ of the micro-scale domain, $\mathbf{t}$ is the boundary traction in the reference configuration, and $ds$ denotes an infinitesimal part of the boundary surface. The initial area vector $\mathbf{A}_q$ is computed by accounting for the different radii of the boundary particles (Miehe and Koch, 2002; Liu et al., 2017):

$$\mathbf{A}_q = \frac{R_q}{R_q + R_{q-1}} (\mathbf{X}_q - \mathbf{X}_{q-1}) \times \mathbf{e}_3 + \frac{R_q}{R_q + R_{q+1}} (\mathbf{X}_{q+1} - \mathbf{X}_q) \times \mathbf{e}_3\,, \tag{3.5}$$

in which $R_{q+1}$, $R_q$ and $R_{q-1}$ are the radii of adjacent boundary particles $q + 1$, $q$ and $q - 1$, respectively. In addition, $e_3$ is the unit vector in the out-of-plane direction of the two-dimensional particle structure, as indicated in Figure 2. It is emphasized that in equation (3.5) the boundary particles must be numbered in the counterclockwise direction to arrive at an area vector pointing in the outward normal direction of the boundary.

The kinematics of a rigid particle $i$ within the granular assembly departs from the linearisation of the macroscopic deformation map. The current position $\mathbf{x}_i$ of the centroid of particle $i$ can be expressed as

$$\mathbf{x}_i = \bar{\boldsymbol{F}} \cdot \mathbf{X}_i + \mathbf{w}_i \qquad \text{for} \qquad i = 1..., P + Q\,. \tag{3.6}$$

The first term in the right hand side of equation (3.6) reflects the contribution on the micro-scale kinematics by the macroscopic homogeneous deformation gradient $\bar{\boldsymbol{F}}$, and the second term indicates the local fluctuation $\mathbf{w}_i$ of the micro-scale position field with respect to the applied homogeneous deformation. The macroscopic deformation is imposed via the frame of boundary particles $\mathcal{P}_q$, which induces contact forces $\mathbf{f}_p$ and $\mathbf{f}_q$ on the inner and boundary particles, and boundary forces $\mathbf{a}_q$ and moments $\mathbf{m}_q$ on the boundary particles, see Figures 3.2(b) and (c). The force and moment equilibria of the overall granular micro-structure can be expressed as

$$\sum_{q=1}^{Q} \mathbf{a}_q = \mathbf{0} \qquad \text{and} \qquad \sum_{q=1}^{Q} (\mathbf{x}_q \times \mathbf{a}_q + \mathbf{m}_q) = \mathbf{0} \qquad \text{for} \qquad q = 1..., Q\,, \tag{3.7}$$

with $\mathbf{x}_q$ the current position vector of the boundary particles. Additionally, local equilibrium conditions must be formulated for each of the inner particles $\mathcal{P}_p$ and for each of the boundary particles $\mathcal{P}_q$:

$$\begin{aligned} &\sum_{c=1}^{N_p^c} \mathbf{f}_p^c = \mathbf{0} \qquad \text{and} \\ &\qquad \sum_{c=1}^{N_p^c} (\mathbf{x}_p^c - \mathbf{x}_p) \times \mathbf{f}_p^c = \mathbf{0} \qquad \text{for} \qquad p = 1..., P\,, \end{aligned} \tag{3.8}$$

$$\begin{aligned} &\sum_{c=1}^{N_q^c} \mathbf{f}_q^c = -\mathbf{a}_q \qquad \text{and} \\ &\qquad \sum_{q=1}^{N_q^c} (\mathbf{x}_q^c - \mathbf{x}_q) \times \mathbf{f}_q^c = -\mathbf{m}_q \qquad \text{for} \qquad q = 1..., Q\,. \end{aligned} \tag{3.9}$$

Equation (3.8) describes force and moment equilibrium of $N_p^c$ contact forces $\mathbf{f}_p^c$ at discrete contact points $\mathbf{x}_p^c$ on the surface of the interior particle $p$, with respect to its current configuration $\mathbf{x}_p$, see Figure 3.2(b). Analogously, relation (3.9) expresses force and moment equilibrium of $N_q^c$ contact forces $\mathbf{f}_q^c$ at contact points $\mathbf{x}_q^c$ on the surface of the boundary particle $q$, in relation to its current configuration $\mathbf{x}_q$, see Figure 3.2(c). Note that the combination of expressions (3.8) and (3.9) results in expression (3.7).

In order to solve the micro-scale problem, a contact law describing the particle interactions is finally required. In the present work, a stick-slip contact law is adopted that relates the contact forces $\mathbf{f}_i^c$ to the corresponding contact displacements $\Delta\mathbf{u}_i^c$ as (Cundall and Strack, 1979)

$$f_n = k_n \Delta u_n \qquad \text{and} \qquad f_s = \begin{cases} k_s \Delta u_s & \text{if} \quad |f_s| \leq -\mu f_n\,, \\ \mu f_n & \text{otherwise}\,. \end{cases} \tag{3.10}$$

where the superscript $c$ and subscript $i$ on the contact force and contact displacement have been dropped for the sake of clarity. The normal particle contact force $f_n$ (with tension considered as positive and compression as negative) depends on the normal particle overlap $\Delta u_n$ between two particles in contact through a multiplication by the normal contact stiffness $k_n$. When the contact is fully sticking, the tangential particle contact force $f_s$ is proportional to the relative tangential displacement $\Delta u_s$ at the particle contact via a multiplication by the tangential contact stiffness $k_s$. This elastic constitutive relation holds up to a limit value at which frictional sliding is initiated, as defined by the normal force multiplied by the particle contact friction coefficient $\mu$.

### 3.2.3 Scale transition relations

#### 3.2.3.1 Macro-to-micro: kinematics and boundary conditions

The kinematical averaging relation is an essential ingredient for establishing the micro-to-macro coupling, by requiring the macro-scale deformation gradient to be equal to the volume average of the local, micro-scale deformation gradients. In a discrete setting, this is equivalent to the expression (Miehe et al., 2010; Liu et al., 2017; Dettmar, 2006)

$$\bar{\boldsymbol{F}} = \frac{1}{V} \sum_{q=1}^{Q} \mathbf{x}_q \otimes \mathbf{A}_q\,. \tag{3.11}$$

Equation (3.11) is enforced to obtain appropriate boundary conditions in terms of displacements and rotations of the boundary particles of the granular microstructure. Different types of boundary conditions may be selected to satisfy the constraint given by equation (3.11), see e.g. (Miehe et al., 2010; Liu et al., 2017), among which the periodic boundary conditions adopted in the present study. Periodic boundary conditions already provide a realistic effective response for micro-structural volumes of relatively small to moderate size, which is commonly bounded by the upper and lower estimates obtained from, respectively, displacement and traction boundary conditions (Kouznetsova et al., 2001; Miehe et al., 2002; Liu et al., 2017). Under periodic boundary conditions both the displacements and rotations of the boundary particles $\mathcal{P}_q$ are subjected to periodicity requirements:

$$\mathbf{x}_q^+ - \mathbf{x}_q^- = \bar{\boldsymbol{F}} \cdot (\mathbf{X}_q^+ - \mathbf{X}_q^-) \qquad \text{and} \qquad \theta_q^+ - \theta_q^- = 0 \qquad \text{on} \qquad \partial V\,, \tag{3.12}$$

with $\theta_q$ the magnitude of the boundary particle center rotation $\boldsymbol{\theta}_q = \theta_q \mathbf{e}_3$, where $\mathbf{e}_3$ is the unit vector in the out-of-plane direction of the 2D particle structure. Superscripts $^+$ and $^-$ refer to corresponding particles on opposite boundaries $^+$ and $^-$ of the granular assembly. Note that equation $(3.12)_1$ directly follows from equation (3.6), by using the periodicity requirement that the local fluctuations at two opposite boundaries must be equal, $\mathbf{w}_q^+ = \mathbf{w}_q^-$. From the viewpoint of equilibrium, the forces and moments on opposite periodic boundaries need to be anti-periodic, thus satisfying the relations

$$\mathbf{a}_q^+ + \mathbf{a}_q^- = \mathbf{0} \qquad \text{and} \qquad m_q^+ + m_q^- = 0 \qquad \text{on} \qquad \partial V\,, \tag{3.13}$$

with $m_q$ the magnitude of the boundary moment, i.e., $\boldsymbol{m}_q = m_q \mathbf{e}_3$.

### 3.2.3.2 Micro-to-macro: macroscopic stress and Hill-Mandel condition

In the micro-to-macro scale transition the macro-scale first Piola-Kirchhoff stress tensor is required to be equal to the surface average of the micro-scale forces $\mathbf{a}_q$ acting on the boundary $\partial V$ of the particle aggregate:

$$\bar{\boldsymbol{P}} = \frac{1}{V} \sum_{q=1}^{Q} \mathbf{a}_q \otimes \boldsymbol{X}_q\,. \tag{3.14}$$

This expression, together with equations (3.11) and (3.12), satisfies the condition on energy consistency between the macro and micro scales, known as the Hill-Mandel micro-heterogeneity condition (Hill, 1963). For a discrete particle system, the Hill-Mandel condition becomes (Miehe and Koch, 2002; Liu et al., 2017)

$$\bar{\boldsymbol{P}} : \delta \bar{\boldsymbol{F}} = \frac{1}{V} \sum_{q=1}^{Q} \mathbf{a}_q \cdot \delta \mathbf{x}_q\,. \tag{3.15}$$

Equation (3.15) essentially states that the volume average of the virtual work applied at the boundaries of the granular micro-structure equals the virtual work of a macroscopic material point.

Finally, the numerical results of the multi-scale simulations will be presented in terms of components of the macro-scale Cauchy stress tensor $\bar{\boldsymbol{\sigma}}$. This stress measure is obtained from the first Piola-Kirchhoff stress $\bar{\boldsymbol{P}}$ computed through (3.14) by using the common transformation rule:

$$\bar{\boldsymbol{\sigma}} = \frac{1}{\det\left(\bar{\boldsymbol{F}}\right)} \bar{\boldsymbol{P}} \cdot \bar{\boldsymbol{F}}^T\,. \tag{3.16}$$

# 3.3 Numerical implementation

## 3.3.1 Macro-scale problem

### 3.3.1.1 Finite element formulation

In order to determine the solution of the macro-scale problem, a finite element formulation based on the theory of large deformations is employed. To this end, a total Lagrange scheme is adopted, for which the initial, undeformed macro-scale domain $\Omega$ is discretized into the domain $\Omega^h$ by using $n_e$ finite elements of volume $\Omega_e \in \Omega^h$. In the finite element formulation the strong form of the quasi-static macroscopic equilibrium (3.1) is transformed into the weak form, which, after integration by parts and using Gauss theorem, results in

$$\int_\Omega \bar{\boldsymbol{P}} : \delta\bar{\boldsymbol{F}} \, \mathrm{d}\Omega - \int_\Omega \bar{\mathbf{b}} \cdot \delta\bar{\mathbf{u}} \, \mathrm{d}\Omega - \int_{\partial\Omega} \bar{\mathbf{t}} \cdot \delta\bar{\mathbf{u}} \, \mathrm{d}\partial\Omega = 0 \,. \tag{3.17}$$

The first and second integrals in equation (3.17) represent the internal work and external work contributions, computed with respect to the test functions $\delta\bar{\boldsymbol{F}} = \boldsymbol{\nabla}(\delta\bar{\mathbf{u}})$ and $\delta\bar{\mathbf{u}}$, respectively. In the spatial discretization procedure, the weak form (3.17) is approximated by formulating the continuous displacement field $\bar{\mathbf{u}}$ in terms of finite element interpolation functions, which leads to a system of non-linear algebraic equations

$$\mathbf{f}_{int}(\boldsymbol{\mathcal{U}}) - \mathbf{f}_{ext} = \mathbf{0} \,. \tag{3.18}$$

Here, the vector $\boldsymbol{\mathcal{U}}$ contains the nodal values of the macroscopic displacement field $\bar{\mathbf{u}}$. The internal and external force vectors are given by

$$\mathbf{f}_{int}(\boldsymbol{\mathcal{U}}) = \int_\Omega \boldsymbol{\mathcal{B}}^T \cdot \bar{\boldsymbol{P}}(\boldsymbol{\mathcal{U}}) \, \mathrm{d}\Omega \quad \text{and} \quad \mathbf{f}_{ext} = \int_\Omega \boldsymbol{\mathcal{N}}^T \bar{\mathbf{b}} \, \mathrm{d}\Omega + \int_{\partial\Omega} \boldsymbol{\mathcal{N}}^T \bar{\mathbf{t}} \, \mathrm{d}\partial\Omega \,, \tag{3.19}$$

where $\boldsymbol{\mathcal{N}}$ and $\boldsymbol{\mathcal{B}}$ are matrices incorporating the interpolation functions and their spatial derivatives, respectively.

### 3.3.1.2 Dynamic relaxation

In the present work an explicit time marching scheme based on dynamic relaxation is adopted. The purpose of the dynamic relaxation method is to reach static equilibrium from the equations of motion in a relatively fast and numerically robust fashion, by effectively dissipating the kinetic energy of the modelled system. This requires the computation of the effective macroscopic stress tensor $\bar{\boldsymbol{P}}$, calculated from expression (3.14) via the boundary forces acting on the granular micro-structure, but circumvents the additional computation of the (computationally expensive) constitutive tangent matrix typically required in implicit time marching schemes. Correspondingly, the macro-scale balance equation, originally given by relation (3.18), takes the form

$$\bar{\mathbf{M}} \cdot \ddot{\boldsymbol{\mathcal{U}}}^n + \bar{\mathbf{C}} \cdot \dot{\boldsymbol{\mathcal{U}}}^n + \mathbf{f}_{int}\left(\boldsymbol{\mathcal{U}}^n\right) = \mathbf{f}_{ext} \,, \tag{3.20}$$

where $\bar{\mathbf{M}}$ is the mass matrix and $\bar{\mathbf{C}}$ is the damping matrix, which here is taken proportional to the mass matrix as $\bar{\mathbf{C}} = \alpha\bar{\mathbf{M}}$, with $\alpha$ a viscous damping coefficient. Further, $\ddot{\mathcal{U}}^n$, $\dot{\mathcal{U}}^n$ and $\mathcal{U}^n$ designate the nodal acceleration, nodal velocity and nodal displacement vectors at time $t_n$, respectively. In correspondence with (Underwood, 1983), the nodal accelerations $\ddot{\mathcal{U}}^n$ at time $t_n$ are approximated through a central difference scheme based on time step $\Delta t$ in the time interval $\left[t_{n-\frac{1}{2}}, t_{n+\frac{1}{2}}\right]$, while the nodal velocities $\dot{\mathcal{U}}^n$ are straightforwardly calculated from averaging the values at times $t_{n-\frac{1}{2}}$ and $t_{n+\frac{1}{2}}$:

$$\ddot{\mathcal{U}}^n = \frac{1}{\Delta t}\left(\dot{\mathcal{U}}^{n+\frac{1}{2}} - \dot{\mathcal{U}}^{n-\frac{1}{2}}\right) \quad \text{and} \quad \dot{\mathcal{U}}^n = \frac{1}{2}\left(\dot{\mathcal{U}}^{n+\frac{1}{2}} + \dot{\mathcal{U}}^{n-\frac{1}{2}}\right). \tag{3.21}$$

Inserting relations (3.21) into the equation of motion (3.20) results in the update for the nodal velocities $\dot{\mathcal{U}}$ at time $t_{n+\frac{1}{2}}$:

$$\dot{\mathcal{U}}^{n+\frac{1}{2}} = \frac{1}{2+\Delta t\alpha}\left[(2-\Delta t\alpha)\,\dot{\mathcal{U}}^{n-\frac{1}{2}} + 2\Delta t\bar{\mathbf{M}}^{-1}(\mathbf{f}_{ext} - \mathbf{f}_{int}(\mathcal{U}^n))\right]. \tag{3.22}$$

Subsequently, the displacement vector $\mathcal{U}^{n+1}$ is computed from the velocity vector $\dot{\mathcal{U}}^{n+\frac{1}{2}}$ as

$$\mathcal{U}^{n+1} = \mathcal{U}^n + \dot{\mathcal{U}}^{n+\frac{1}{2}}\Delta t\,. \tag{3.23}$$

In the above relations a lumped (diagonal) mass matrix is used, for which the diagonal terms at nodes $k = 1, \ldots K$ of element $e$ follow from (Zienkiewicz and Taylor, 1991)

$$M^e_{kk} = \frac{\int_{\Omega_e} \mathcal{N}_k^2 \mathrm{d}\Omega}{\sum_{k=1}^{K} \int_{\Omega_e} \mathcal{N}_k^2 \mathrm{d}\Omega} \int_{\Omega_e} \bar{\rho}\mathrm{d}\Omega, \tag{3.24}$$

where $K$ is the total number of nodes of element $e$, $\mathcal{N}_k$ is the shape function referring to node $k$, and $\bar{\rho}$ is the macroscopic density computed as the product between the particle density $\rho$ and the packing volume fraction $v_m$, i.e., $\bar{\rho} = \rho v_m$. The damping coefficient $\alpha$ appearing in equation (3.22) is adjusted in each iteration $j$ of time step $n$ as (Benson, 2007)

$$\alpha = \alpha^{n,j} = 2\xi\omega^{n,j}, \tag{3.25}$$

with $\xi$ the damping ratio and $\omega^{n,j}$ a frequency parameter, computed as (Zhang and Yu, 1989):

$$\omega^{n,j} = \left(\frac{(\mathcal{U}^{n,j})^T \mathbf{f}^{n,j}_{int}}{(\mathcal{U}^{n,j})^T \bar{\mathbf{M}} \mathcal{U}^{n,j}}\right)^{1/2}. \tag{3.26}$$

Finally, for warranting the stability of the solution, the time increment $\Delta t$ is iteratively updated as (Benson, 2007)

$$\Delta t = \Delta t^{n,j} = \gamma\frac{2}{\omega^{n,j}}\left(\sqrt{\xi^2+1} - \xi\right), \tag{3.27}$$

with $\gamma$ a safety factor. This safety factor ensures that the time increment $\Delta t$ can be prescribed sufficiently small to avoid numerical divergence characteristic of an explicit time-marching scheme. The solution of equation (3.20) is considered to be converged when the ratio between the systems' kinetic energy $\bar{E}^{n,j}_{kin}$ in the current iteration $j$ of time step $n$ and the maximal kinetic energy $\bar{E}^{n}_{kin,max}$ reached during the time step is less or equal than a prescribed tolerance $\mathrm{tol}_{\bar{E}}$:

$$\frac{\bar{E}^{n,j}_{kin}}{\bar{E}^{n}_{kin,max}} \leq \mathrm{tol}_{\bar{E}}\,, \tag{3.28}$$

with the kinetic energy computed as

$$\bar{E}^{n,j}_{kin} = \frac{1}{2}(\dot{\boldsymbol{\mathcal{U}}}^{n,j})^T \bar{\mathbf{M}} \dot{\boldsymbol{\mathcal{U}}}^{n,j}. \tag{3.29}$$

The macro-scale solution procedure has been implemented in the finite element code ESyS-Escript (Schaa et al., 2016); details on the solution algorithm are provided in Section 3.3.3. The package mpi4py[2] was used for parallelizing the DEM computations at the different integration points.

## 3.3.2 Micro-scale problem

### 3.3.2.1 Dynamic relaxation

The micro-scale boundary value problem, consisting of the equilibrium equations (3.7) to (3.9), the constitutive response of the particles (3.10), and the boundary conditions (3.12), is solved by applying a dynamic relaxation method, similar to the approach adopted for the macro-scale problem. For each particle $i$, with $i = 1, .., P + Q$, the generalized equation of motion can be expressed as

$$\mathbf{M}_i \ddot{\mathbf{d}}_i = (\mathbf{p}_r + \mathbf{p}_d)_i \qquad \text{for} \qquad i = 1..., P + Q\,, \tag{3.30}$$

where the mass matrix $\mathbf{M}_i = \mathrm{diag}\,[M_i, I_i]$ includes the particle mass $M_i$ and the mass moment of inertia $I_i = M_i R_i^2/2$, with $R_i$ the particle radius. The term $\ddot{\mathbf{d}}_i$ represents the generalized acceleration vector, calculated as the second time derivative of the generalized coordinate vector $\mathbf{d}_i = [\mathbf{x}_i,\ \boldsymbol{\theta}_i \cdot \mathbf{e}_3]^T$. The generalized coordinate vector contains the current locations of the particle centres $\mathbf{x}_i$ and the particle rotations $\boldsymbol{\theta}_i$. The vector $\mathbf{p}_r = [\mathbf{f}_r,\ \mathbf{m}_r \cdot \mathbf{e}_3]^T$ is the generalized force vector composed of the resultant force $\mathbf{f}_r$ and moment $\mathbf{m}_r$ acting on particle $i$. Analogously, $\mathbf{p}_d = [\mathbf{f}_d,\ \mathbf{m}_d \cdot \mathbf{e}_3]^T$ is the generalized vector containing the resulting particle force and moment following from the artificial dissipation applied in the simulations. Based on (Potyondy and Cundall, 2004), the artificial dissipative force $\mathbf{f}_d$ and moment $\mathbf{m}_d$ are defined as $\mathbf{f}_d = -\alpha|\mathbf{f}_r|\,\mathrm{sign}(\dot{\mathbf{x}}_i)$ and $\mathbf{m}_d = -\beta|\mathbf{m}_r|\,\mathrm{sign}(\dot{\boldsymbol{\theta}}_i)$. The symbols $\alpha$ and $\beta$ are damping values that are coupled to (signum) functions of the particle translational velocity $\dot{\mathbf{x}}_i$ and rotational

---

[2] See: http://mpi4py.scipy.org/docs/

velocity $\dot{\boldsymbol{\theta}}_i$, respectively. The equations of motion (3.30) are integrated using an explicit, first-order finite difference scheme, the details of which can be found in (Weatherley et al., 2014) . The dynamic relaxation process is considered to be converged when the ratio between the kinetic energy $E_{kin}$ of the inner particles $\mathcal{P}_p$ in the granular medium and their potential energy $E_{pot}$ is less or equal than a prescribed tolerance (Imole et al., 2013), i.e.,

$$\frac{E_{kin}}{E_{pot}} \leq \mathrm{tol}_E \, , \tag{3.31}$$

with

$$E_{kin} = \frac{1}{2}\sum_{i=1}^{P} \dot{\mathbf{d}}_i^T \mathbf{M}_i \dot{\mathbf{d}}_i \qquad \text{and} \qquad E_{pot} = \frac{1}{2}\sum_{c=1}^{N^c} \left[ k_n \left( \frac{f_n^c}{k_n} \right)^2 + k_s \left( \frac{f_s^c}{k_s} \right)^2 \right] , \tag{3.32}$$

where $f_n^c/k_n$ and $f_s^c/k_s$ reflect the relative elastic displacements in the normal and tangential directions of particle contact $c$ and $N^c$ is the total number of particle contacts.

#### 3.3.2.2 Servo-control algorithm for micro-scale boundary conditions

The periodic displacement and periodic rotation boundary conditions discussed in Section 3.2.3.1 were implemented by means of a servo-control algorithm (Liu et al., 2017). This algorithm is based on finding an iterative correction for the boundary particle displacements and rotations in order to reduce the difference between the measured and the required values of the boundary condition. Considering the anti-periodicity conditions (3.13) required for boundary forces and boundary moments, the corresponding residuals for the edge particles are

$$\Delta \mathbf{a}_e = \mathbf{a}_e^+ + \mathbf{a}_e^- , \quad \Delta m_e = (\mathbf{m}_e^+ + \mathbf{m}_e^-) \cdot \mathbf{e}_3 \qquad \text{for } e = 1..., E/2 \, . \tag{3.33}$$

Introducing the gain parameters $g_a$ and $g_m$, the corrections for displacements and rotations of the edge particles can be obtained by multiplying the residuals by the corresponding gains:

$$\Delta \mathbf{u}_e^+ = \Delta \mathbf{u}_e^- = g_a \Delta \mathbf{a}_e , \quad \Delta\theta_e^+ = \Delta\theta_e^- = g_m \Delta m_e \qquad \text{for } e = 1..., E/2 \, . \tag{3.34}$$

For the four corner particles no displacement correction is needed as their displacements are directly imposed as a function of the macroscopic deformation, i.e. $\mathbf{x}_c = \bar{\boldsymbol{F}}\mathbf{X}_c$. The rotations of the corner particles are updated in a similar way as done for the edge particles in relation (3.34), in accordance with the correction

$$\Delta\theta_c^+ = \Delta\theta_c^- = g_m \Delta m_c \, , \tag{3.35}$$

with

$$\Delta m_c = \sum_{c=1}^{4} \mathbf{m}_c \cdot \mathbf{e}_3 \, . \tag{3.36}$$

This correction is added to the displacement and rotation calculated at the previously converged increment. The process is considered to be converged when the residual in terms of the particle forces and particle moments, defined in expressions (3.33) and (3.36), satisfies the criterion

$$r_a(\Delta \mathbf{a}_e, \Delta m_e, \Delta m_c) \leq \epsilon_a \, . \tag{3.37}$$

The residual $r_a$ is characterized by the normalized $L_2$-norm of the incremental boundary forces $\Delta \mathbf{a}_e$ and moments $\Delta m_e$ and $\Delta m_c$ of the edge and corner particles, see Table 2, and $\epsilon_a$ is a pre-defined tolerance. The implementation of the micro-scale problem, involving the dynamic relaxation procedure and the servo-control algorithm for the boundary conditions, has been performed by using the open-source discrete element code ESyS-Particle (Virgo et al., 2013; Guo and Zhao, 2013). The numerical algorithm for the multi-scale framework is discussed in detail in Section 3.3.3.

### 3.3.3 Multi-scale FEM-DEM coupling

In order to perform a multi-scale analysis of a granular system, the macroscopic continuum formulation treated in Section 3.3.1 is coupled to the discrete micro-scale model described in Section 3.3.2. The coupled macro-micro solution algorithm is summarized in Table 3.1. The macroscopic domain is discretized in $n_e$

**Table 3.1:** Incremental-iterative nested multi-scale solution scheme for the coupled FEM-DEM framework.

| **MACRO** | | **MICRO** |
|---|---|---|
| **1.** Initialization<br>• Initialize the macroscopic model<br>• Assign a discrete RVE to every IP | | |
| **2.** Next increment $i_{inc} \geq 1$<br>• Apply increment of the macroscopic external load | | |
| **3.** Next iteration $i_{it} \geq 1$<br>• Loop over all integration points<br>If increment $i_{inc} = 1 \Rightarrow$ Set $\bar{\boldsymbol{F}} = \mathbf{I}$ and $\bar{\boldsymbol{P}} = \mathbf{0}$ | | |
| If increment $i_{inc} > 1 \Rightarrow$ Update deformation gradient $\bar{\boldsymbol{F}}$ | $\xrightarrow{\bar{\boldsymbol{F}}}$ | DEM simulation - see Table 3.2<br>• Prescribe periodic boundary conditions<br>• Dynamic relaxation |
| Store macroscopic stress $\bar{\boldsymbol{P}}$ | $\xleftarrow{\bar{\boldsymbol{P}}}$ | • Compute macroscopic stress $\bar{\boldsymbol{P}}$ |
| **4.** Continue iteration<br>• End IPs loop<br>• Solve the macroscopic equation of motion (3.20) with iteratively updated damping coefficient (3.26) and time step (3.27)<br>• Compute nodal velocities using (3.22)<br>• Compute nodal displacements with (3.23) | | |
| **5.** Check for convergence (3.28) in terms of kinetic energy<br>• If converged $\Rightarrow$ go to next increment 2<br>• If not converged $\Rightarrow$ go to next iteration 3 | | |

finite elements, with $n_{ip}$ integration points (IPs) per element. Before the loading is applied, an identical granular micro-structure is assigned to each integration point. The multi-scale coupling is realized by following a deformation driven procedure, consistent with the homogenization strategy presented in Section 3.2. As pointed out in Table 3.1, the external load is applied to the macroscopic domain in an incremental fashion, whereby for each macroscopic integration point the macroscopic deformation gradient $\bar{\boldsymbol{F}}$ is incrementally updated from the nodal displacements, and subsequently imposed upon the frame of boundary particles of the micro-scale granular packing. At the onset of each increment the macroscopic deformation is applied homogeneously to all the boundary particles $\mathcal{P}_q$, and the particle assembly is dynamically relaxed to its equilibrium state. Subsequently, an iterative loop is entered, whereby the corrections for the displacement and rotation of the boundary particles are calculated following the servo-control methodology, see relations (3.33)-(3.36). After the application of these corrections, the particle system is again dynamically relaxed to the equilibrium state, and the residual $r_a$ is computed as a function of the current values of the boundary forces and moments. When the convergence criterion given by (3.37) is satisfied, the iterative loop is terminated. The macro-scale stress $\bar{\boldsymbol{P}}$ is calculated from the micro-structural boundary forces in accordance with expression (3.14), and its value is transferred back to the corresponding integration point in the macroscopic domain. This procedure is performed for all integration points in the macroscopic domain. Table 3.2 summarizes the solution algorithm for the micro-scale DEM simulation. Once the macroscopic stress is computed in the integration points, the macroscopic equations of motion (3.20) are solved using the iteratively adjusted values of the damping coefficient (3.25) and time step (3.27). The nodal velocities and nodal displacements are calculated from relations (3.22) and (3.23). When criterion (3.28) is satisfied, the current increment is considered to be converged. When this is not the case, the procedure above is repeated, until

**Table 3.2:** Algorithm for the solution of the DEM problem.

```
DEM simulation. Increment $i_{inc}$
1. Initialize boundary conditions by applying updated macro-scale deformation homogeneously
        $\mathbf{x}_q = \bar{\boldsymbol{F}}\mathbf{X}_q$   and   $\theta_q = 0$   for   $q = 1..., Q$
2. Dynamic relaxation until convergence criterion (3.31) is satisfied.
        Obtain boundary forces and moments.
3. Update particle configuration
        Partition the boundary into corner c and edge e particles
        Calculate edge particles displacement $\Delta\mathbf{u}_e$ and rotation $\Delta\theta_e$ corrections via (3.33)-(3.34)
        and corner particles rotation corrections $\Delta\theta_c$ via (3.35)-(3.36)
4. Dynamic relaxation until convergence criterion (3.31) is satisfied.
        Obtain boundary forces and moments.
5. Calculate residual
        $r_a = \sqrt{\sum_{e=1}^{E/2}(\Delta\mathbf{a}_e \cdot \Delta\mathbf{a}_e/\tilde{a}_e^2 + (\Delta m_e/\tilde{m}_e)^2) + (\Delta m_c/\tilde{m}_c)^2}$
        where $\tilde{a}_k = \frac{M_k R_k}{\Delta t^2}$, $\tilde{m}_k = \frac{M_k R_k^2}{\Delta t^2}$ with $M_k$ and $R_k$ the mass and radius of particle $k$; $k \in \{c, e\}$.
6. Check for convergence: $r_a \leq \epsilon_a$
        6A. if converged $\Longrightarrow$ Save current configuration, compute macroscopic stress $\bar{\boldsymbol{P}}$ with (3.14)
        and go to macro-scale simulation.
        6B. if not converged $\Longrightarrow$ Return to 3.
```

expression (3.28) holds.

## 3.4 Computational results

In this section the proposed FEM-DEM multi-scale framework is validated on a series of representative numerical simulations. A reference problem is defined first, for which a mesh convergence study is performed to establish the appropriate element size for the FEM model. Subsequently, the influence of various micro-structural properties on the macro-scale response is investigated.

### 3.4.1 Definition of the reference problem

The macro-scale domain consists of a rectangular specimen of dimensions $10$ mm $\times$ $20$ mm, supported vertically at the complete bottom edge and horizontally in the lower left corner node. The domain is discretized into $n_e$ bilinear quadrilateral elements, with $n_{ip} = 4$ integration points per element. The specimen is first subjected to isotropic compression with the stress magnitude $\bar{\sigma}_0 = 0.15$ MN/m applied in ten loading steps, see Figure 3.3(a). Next, a biaxial compression loading stage is initiated, whereby the vertical displacement $\bar{d}$ is increased incrementally up to a vertical strain of $\bar{\varepsilon} = \bar{d}/h_{ic} = 10\%$ of the sample height $h_{ic}$ obtained after isotropic compression, see Figure 3.3(b). The contribution by the gravitational loading to the sample response is relatively small, and therefore may be ignored. Four different FEM discretizations of the macro-scale domain are considered, as detailed in Section 3.4.2. The damping ratio and safety factor used in expression (3.27) are $\xi = 1.0$ and $\gamma = 0.5$, respectively[3]. The constitutive behaviour in each macroscopic integration point follows from the effective response of an initially (almost) isotropic polydisperse packing composed of 228 particles, see Figure 3.3(c) and (d). The chosen number of particles is based on the convergence study performed in (Liu et al., 2017), which shows that under simple shear deformation and periodic boundary conditions the effective stress response for this number of particles does not significantly change under a further increase of the sample size. The initial packing structure is generated by a collision-driven molecular dynamics code and subsequently reconstructed into a geometrically periodic packing, see (Liu et al., 2017) for more details. The particle radii are taken from a uniform size distribution with polydispersity $R_{max}/R_{min} = 1.5$, with the minimal particle radius in accordance with $R_{min}/L = 0.03$, where $L$ is the side length of the initially square micro-structural domain. Note that from dimensional considerations it follows that the sample response is uniquely determined via the specific values chosen for the ratios $R_{min}/L$ and $R_{max}/R_{min}$. The volume fraction of the initial packing is $v_m = 0.846$, and the initial coordination number (i.e, before the application of isotropic compression) is $\bar{n}^0 = 2C/(P + Q) = 3.42$,

---

[3] Occasionally, the damping ratio $\xi$ and safety factor $\gamma$ were modified during the simulation to improve the convergence speed.

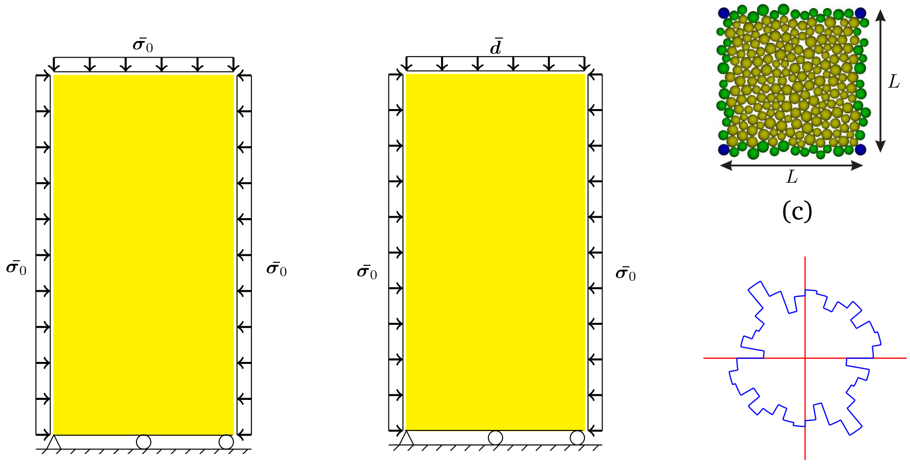

(a) (b) (c) (d)

**Figure 3.3:** Geometry of the macro-scale problem and applied boundary conditions for the (a) initial isotropic compression loading stage, and (b) biaxial compression loading stage; (c) initial, square micro-structural domain, and (d) corresponding rose diagram.

with $C$ the total number of particle contacts and $P+Q$ the total number of (inner + boundary) particles. The fabric anisotropy is measured as

$$\mathcal{A} = \frac{\Pi_1}{\Pi_2} - 1\,, \tag{3.38}$$

where $\Pi_1$ and $\Pi_2$ are the eigenvalues of the fabric tensor

$$\mathbf{\Pi} = \frac{1}{2C} \sum_{p=1}^{P+Q} \sum_{c=1}^{N_p^c} \mathbf{n}^{pc} \otimes \mathbf{n}^{pc}\,, \tag{3.39}$$

with $N_p^c$ the total number of particles in contact with particle $p$ and $\mathbf{n}^{pc}$ the unit vector pointing from the centroid of particle $p$ to the specific contact point $c$. The initial anisotropy of the reference packing is $\mathcal{A}^0 = 0.02$. The normal and tangential stiffnesses in the stick-slip particle contact model (3.10) are $k_n = 10^4$ N/m and $k_s = 2 \cdot 10^3$ N/m, representing relatively *soft* particles, and the friction coefficient equals $\mu = 0.4$. The density of the particles is $\rho = 2 \cdot 10^3$ kg/m$^2$. The translational and rotational damping factors used in the dynamic relaxation procedure are $\alpha = \beta = 0.7$, and the time increment is $\Delta t = 10^{-6}$s. The gain parameters adopted in equation (3.34) for the application of the boundary conditions are (in dimensionless form) $g_a M/\Delta t^2 = 1 \cdot 10^2$ and $g_m M_i R_i^2/\Delta t^2 = 2 \cdot 10^2$, with $M_i = \rho \pi R_i^2$ representing the mass of particle $i$ and $R_i$ its radius. The tolerances in expressions (3.31) and (3.37) are taken as $\mathrm{tol}_E = 10^{-3}$ and $\epsilon_a = 10^{-4}$, respectively. The parameters used at the macroscopic and microscopic levels of the multi-scale framework are summarized in Table 3.3.

**Table 3.3:** Geometrical, physical and algorithmic model parameters at the macro and micro scales.

| Parameter | Value | Unit |
|---|---|---|
| **Macro-scale** | | |
| Applied stress isotropic compression $\bar{\sigma}_0$ | $0.15$ | MN/m |
| Vertical strain biaxial compression $\bar{\varepsilon}$ | $0.1$ | - |
| Tolerance kinetic energy $\mathrm{tol}_{\bar{E}}$ | $10^{-3}$ | - |
| Damping ratio $\xi$ | $1.0$ | - |
| Safety factor $\gamma$ | $0.5$ | - |
| **Micro-scale** | | |
| Polydispersity $R_{max}/R_{min}$ | $1.5$ | |
| Anisotropy $\mathcal{A}^0$ | $0.02$ | |
| Coordination number $\bar{n}^0$ | $3.42$ | |
| Elastic normal stiffness $k_n$ | $1 \cdot 10^4$ | N/m |
| Elastic tangential stiffness $k_s$ | $2 \cdot 10^3$ | N/m |
| Friction coefficient $\mu$ | $0.4$ | - |
| Density $\rho$ | $2 \cdot 10^3$ | kg/m$^2$ |
| Translational damping $\alpha$ | $0.7$ | - |
| Rotational damping $\beta$ | $0.7$ | - |
| Time increment $\Delta t$ | $10^{-6}$ | s |
| Tolerance force $\epsilon_a$ | $10^{-4}$ | - |
| Gain force $g_a M/\Delta t^2$ | $1 \cdot 10^2$ | - |
| Gain moment $g_m M R^2/\Delta t^2$ | $2 \cdot 10^2$ | - |
| Tolerance dynamic relaxation $\mathrm{tol}_E$ | $10^{-3}$ | - |

### 3.4.2 Mesh convergence study

In order to explore the mesh sensitivity of the multi-scale approach, the macroscopic domain depicted in Figure 3.3(a) has been discretized into four different finite element meshes, which are characterized by the following number of elements: $n_e = [1 \times 1, 1 \times 2, 2 \times 4, 4 \times 8]$, with the corresponding number of integration points as $n_{ip} = [4, 8, 32, 128]$, respectively. The specimen first undergoes isotropic compression, followed by biaxial compression, as described in Section 3.4.1. The overall stress-deformation response for the considered meshes is shown in Figure 3.4. The stress is measured in terms of the stress ratio $\bar{\sigma}$, given by

$$\bar{\sigma} = \left| \frac{\bar{\sigma}_{11} - \bar{\sigma}_{22}}{\bar{\sigma}_{11} + \bar{\sigma}_{22}} \right| , \tag{3.40}$$

which is taken as the average over all integration points, where $\bar{\sigma}_{11}$ and $\bar{\sigma}_{22}$ are the normal components of the macroscopic Cauchy stress (3.16) in the axial and lateral directions of the specimen, respectively. Note that the biaxial stress ratio

$\bar{\sigma}$ given by Equation (3.40) directly reflects the macroscopic friction angle $\phi_m$ via the usual relation $\phi_m = \arcsin(\bar{\sigma})$. The linear axial strain $\bar{\varepsilon}$ is imposed on the specimen via the vertical displacement $\bar{d}$:

$$\bar{\varepsilon} = \frac{\bar{d}}{h_{ic}}, \tag{3.41}$$

where $h_{ic}$ is the sample height obtained after the initial, isotropic compression stage.

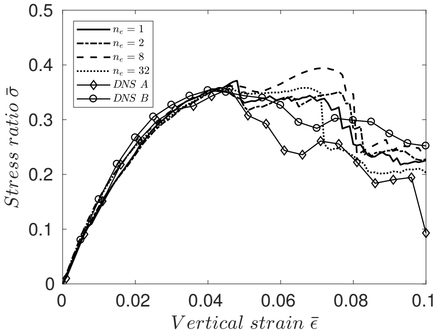

**Figure 3.4:** Average macroscopic stress ratio $\bar{\sigma}$ as a function of the applied vertical strain $\bar{\varepsilon}$ for different mesh sizes, and the comparison with the predictions of two DNS with 441 particles (*A*) and 1641 particles (*B*).

The results of the multi-scale simulations are compared to those of two direct numerical simulations (DNS), in which the rectangular specimen is described by DEM models of 441 and 1681 particles.These models are referred to as DNS *A* and DNS *B*, respectively, and the corresponding samples are constructed by copying the square $L \times L$ micro-structural domain (used in the multi-scale simulations) multiple times along the sample height and width, see Figures 3.7(e) and (f). Accordingly, the length scale $L$ defines the sample height and width as $2L \times L$ for DNS *A* and $4L \times 2L$ for DNS *B*. The particle radius is kept the same in the two DEM models, in accordance with the ratios $R_{max}/R_{min} = 1.5$ and $R_{min}/L = 0.03$ adopted for the micro-structure used in the multi-scale simulations.

The traction boundary conditions characterizing the initial isotropic compression stage and the displacement boundary condition defining the biaxial compression stage are applied in accordance with the servo-control procedure presented in (Liu et al., 2017). Figure 3.4 illustrates that the average stress response of the coupled FEM-DEM models for all meshes considered is very close to the predictions of the direct numerical simulations, in particular in the pre-peak regime, $0 \leq \bar{\varepsilon} \leq 0.05$. After this point, a moderate softening behaviour is observed, whereby the responses for the different meshes start to deviate from one other. The mesh size dependency of the FEM response in the post-peak regime is a well-known effect; to circumvent this problem in a multi-scale setting, kinematically enriched multi-scale frameworks have been proposed in the literature, see (Bosco et al., 2014, 2015b). Since in the present work the focus is mainly on the pre-peak regime of the macroscopic response, the application of these frameworks for granular systems is considered as a topic for future research.

The influence of the choice of the macroscopic mesh size on the effective response is further investigated by considering the evolution of the coordination number $\bar{n}$ and the induced fabric anisotropy $\mathcal{A}$ (both averaged over all macroscopic integration points), see Figures 3.5(a) and (b). As a general trend, it can be observed that the results are only slightly sensitive to the mesh adopted. The coordination number somewhat decreases with increasing deformation, due to the horizontal expansion of the macroscopic domain. The anisotropy initially increases, since the packing deforms stronger in the vertical direction than in the horizontal direction, in correspondence with the macroscopic biaxial loading conditions applied. The induced anisotropy becomes maximal at about the same deformation stage as at which the peak strength is reached. In the softening regime, a small decrease in anisotropy is observed, which is caused by a dilating particle structure that develops under progressive shear failure.

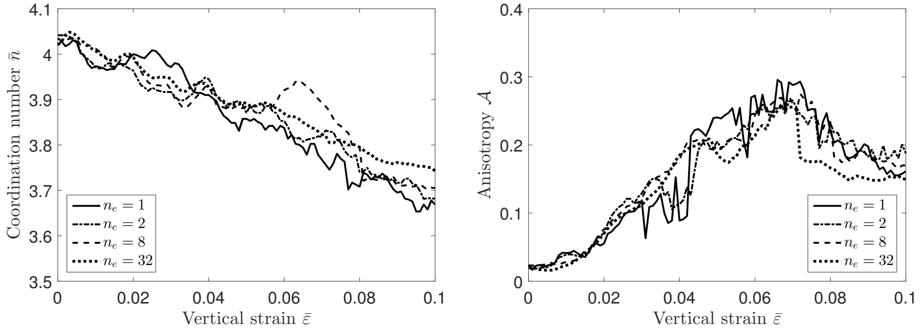

(a) (b)

**Figure 3.5:** (a) Average macroscopic coordination number $\bar{n}$ and (b) average induced anisotropy $\mathcal{A}$ as a function of the applied vertical strain $\bar{\varepsilon}$ for different mesh sizes.

In addition to examining the development of the *average* stress in the macroscopic domain, the *variation* in stress is considered by plotting the stress evolutions in the individual integration points of the FEM model. Figures 3.6(a) and (b) show the stress ratio $\bar{\sigma}$ in all the integration points of two specific meshes selected, which have $n_e = [2 \times 4]$ and $n_e = [4 \times 8]$ elements, respectively. The thick black line represents the corresponding average stress response taken from Figure 3.4. In general, the spread in stress values in the relatively coarse mesh is smaller than in the fine mesh, which illustrates that the fine mesh more accurately describes the heterogeneous response of the macroscopic domain. The heterogeneity of the response clearly becomes rather strong in the softening regime, due to a localization of the macroscopic deformation pattern. This effect can be further explored by depicting the micro-structures at a vertical deformation $\bar{\varepsilon} = 0.09$ in two different integration points, corresponding to the locations with the highest (bold dark grey line) and lowest (bold light grey line) stress levels at the macro-scale. The micro-structural responses clearly show differences in both the overall deformed shape and in the force chains developing within the particle structure (indicated by the red lines).

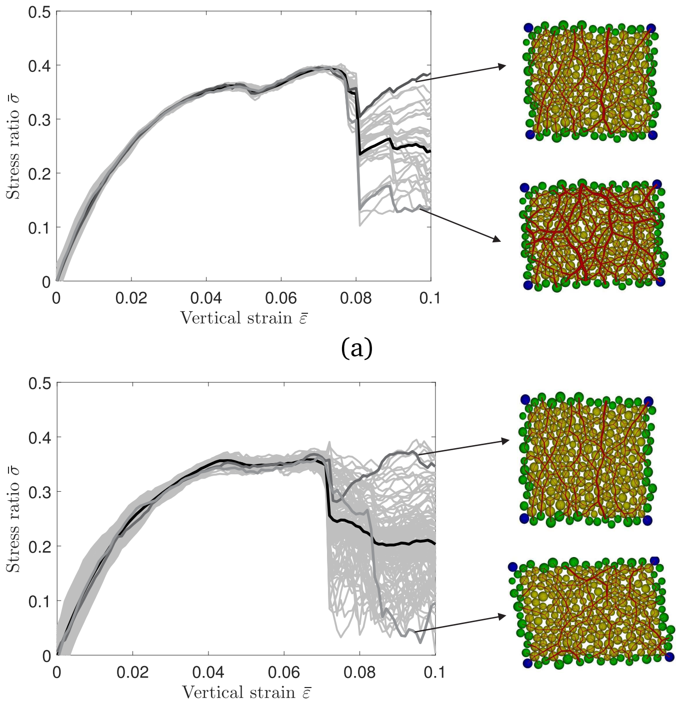

(a)

(b)

**Figure 3.6:** Evolution of the stress ratio $\bar{\sigma}$ in all integration points of the two FEM meshes (a) $n_e = [2 \times 4]$ and (b) $n_e = [4 \times 8]$. The bold dark grey and light grey lines refer to the integration points with the highest and lowest stress levels at a strain $\bar{\varepsilon} = 0.09$, and the corresponding micro-structural responses are visualized in the insets (with the particle contact forces indicated in red). The black bold line represents the evolution of the average stress, taken from Figure 3.4.

In conclusion, the results in Figures 3.4 and 3.5 demonstrate that even the coarsest mesh with $n_e = [1 \times 1]$ accurately captures the *average* multi-scale stress-deformation response. This supports the capability of the proposed multi-scale framework to adequately perform large-scale simulations with a relatively coarse mesh discretization of the macroscopic domain at limited computational cost. Obviously, a finer mesh allows for a richer description of the heterogeneous macroscopic response. This aspect, which has been noticed from the stress evolutions in Figure 3.6, is further elaborated by comparing the deformed macroscopic configurations computed by the multi-scale method and the DNS at the end of the deformation process $\bar{\varepsilon} = 0.1$, see Figure 3.7. Here, the variable used in the contour plots is the incremental equivalent strain $\Delta\bar{\varepsilon}_{eq}$, defined as the $L^2$-norm of the increments of the components of the linear strain tensor $\bar{\varepsilon} = \bar{\boldsymbol{F}} - \mathbf{I}$. It can be observed that the deformation of the macroscopic domain computed by the multi-scale simulations lies closer to those computed by DNS when the mesh be-

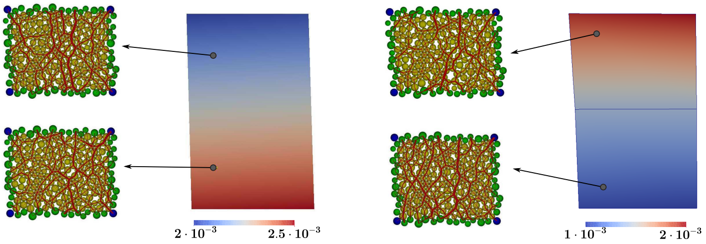

(a) Mesh with $n_e = [1 \times 1]$ (b) Mesh with $n_e = [1 \times 2]$

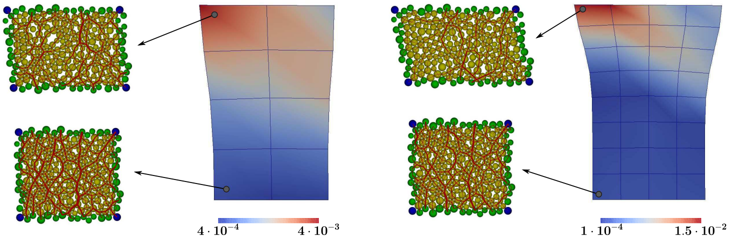

(c) Mesh with $n_e = [2 \times 4]$ (d) Mesh with $n_e = [4 \times 8]$

(e) DNS A: 441 particles (f) DNS B: 1681 particles

**Figure 3.7:** (a)-(b)-(c)-(d) Contour plots of the incremental equivalent strain $\Delta\bar{\varepsilon}_{eq}$ on the deformed macroscopic domain at $\bar{\varepsilon} = 0.1$, for the four considered meshes; the insets illustrate the deformed micro-structures at integration points near the top and bottom of the macroscopic domain (with the particle contact forces indicated in red). (e)-(f) Deformed configurations of the two direct numerical simulations, shown for comparison.

comes finer. In addition, the localization pattern becomes more prominent for a finer mesh. Based on these results, it is concluded that a good compromise between the accuracy in the description of the local macroscopic features and the computational time is found for the mesh of $n_e = [2 \times 4]$ elements with $n_{ip} = 32$ integration points. Hence, this mesh will be used for the forthcoming multi-scale simulations in which the influence of micro-structural parameters on the effective macroscopic response is analysed. As a final note, from the deformed configurations computed with DNS it can be observed that a few inner particles have been pushed through the frame of boundary particles during the dynamic relaxation procedure, thereby ending up outside the actual macroscopic domain. A way to prevent this from happening is by extending the thickness of the boundary frame with more particles. This solution, however, has not been implemented here, since the influence of this effect on the macroscopic response is negligible.

### 3.4.3 Influence of micro-structural parameters on the macroscopic response

The macroscopic geometry in Figure 3.3 is discretized with the selected mesh of $2 \times 4$ finite elements, whereby the particle contact friction, the particle rotation, and the initial fabric anisotropy are varied. In the analysis of the results the attention will be focused on the pre-peak regime of the macroscopic response, during which the FEM results are independent of the mesh size, see Section 3.4.2.

#### 3.4.3.1 Particle contact friction

The effect of the particle contact friction on the macro-scale response is investigated by considering three different values for the particle contact friction, namely $\mu = [0.2, 0.4, 0.6]$. Note that $\mu = 0.4$ is the friction coefficient of the reference particle packing studied in Section 3.4.2. The macroscopic stress evolution, expressed in terms of the stress ratio $\bar{\sigma}$ averaged over all the integration points, is presented in Figure 3.8(a). In addition, the evolution of the volumetric deformation $\bar{J}_{rel} = (\det(\bar{\mathbf{F}}) - \det(\bar{\mathbf{F}}_{ic}))/\det(\bar{\mathbf{F}}_{ic})$ is plotted in Figure 3.8(b), where $\bar{\mathbf{F}}_{ic}$ is the deformation gradient, evaluated at the end of the preliminary isotropic compression stage. As expected, from Figure 3.8(a) it follows that in the pre-peak regime the stress ratio clearly is higher for a larger particle contact friction. In addition, the development of compaction (corresponding to a negative value of $\bar{J}_{rel}$) during the initial stage of deformation, as typical for packings with relatively soft particle contacts, is larger for a higher value of the particle contact friction. Essentially, the normal contact forces become higher when the particle contact friction increases, which generates more particle overlap, and thus more compaction. This result is consistent with other DEM results presented in the literature (Göncü and Luding, 2013). At $\bar{\varepsilon} = 0.08$ the structure starts to fail and develops into a dilated particle structure (corresponding to a positive value of $\bar{J}_{rel}$). At this stage, the order of the deformation responses in Figure 3.8(b) changes, and is expected to eventually show a trend whereby the dilation will be larger for a higher particle friction, see also (Suiker and Fleck, 2004; Göncü and Luding, 2013). However, this will happen at deformations falling outside the range considered here, whereby shear failure has substantially developed.

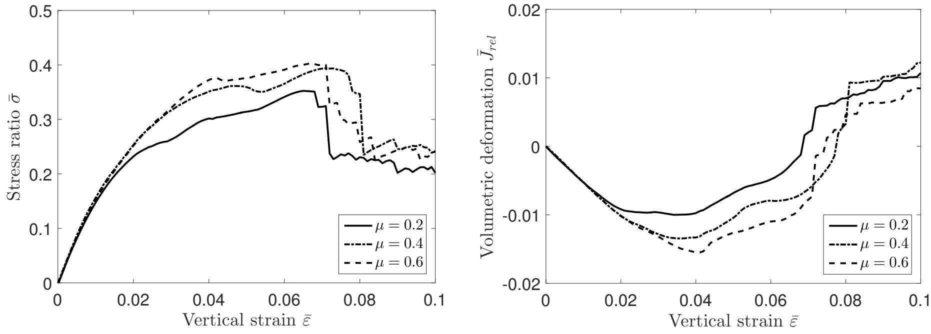

(a) (b)

**Figure 3.8:** (a) Average macroscopic stress ratio $\bar{\sigma}$ and (b) average volumetric deformation $\bar{J}_{rel}$ as a function of the applied vertical strain $\bar{\varepsilon}$ for different particle contact friction coefficients $\mu$.

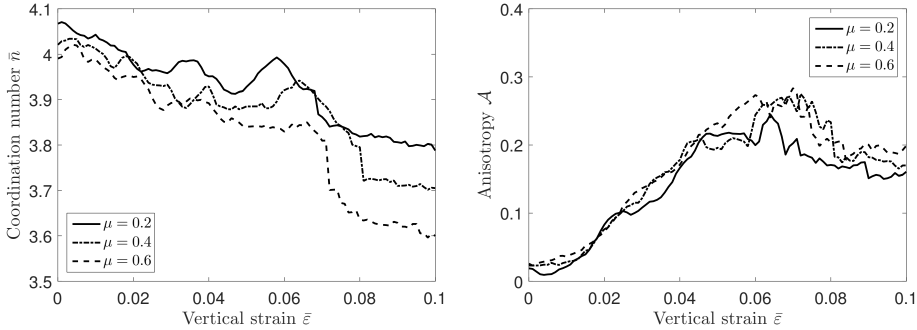

(a) (b)

**Figure 3.9:** (a) Average macroscopic coordination number $\bar{n}$ and (b) average induced anisotropy $\mathcal{A}$ as a function of the applied vertical strain $\bar{\sigma}$ for different particle contact friction coefficients $\mu$.

The evolutions of the mean coordination number $\bar{n}$ and the mean anisotropy parameter $\mathcal{A}$ for simulations performed with different particle friction coefficients are illustrated in Figures 3.9(a) and (b), respectively. For all cases the coordination number decreases with increasing deformation; the loss of contacts can be ascribed to the horizontal expansion of the specimen, which occurs despite that the overall material structure compacts, see Figure 3.8(b). A similar observation was made in the DEM study presented in (Kuhn, 1999). Moreover, the coordination number in general is lower for a higher particle contact friction, which is in correspondence with the DEM study presented in (Göncü and Luding, 2013). Since the coordination number is lower and the overall strength is larger at higher particle contact friction, the average particle contact force becomes larger when the particle contact friction increases. Observe further that the effect of the contact friction on the induced fabric anisotropy is minimal during the initial stage of the response. Close to progressive shear failure some differences emerge, whereby the induced anisotropy tends to grow when the particle contact friction, and thus the overall failure strength, becomes larger.

#### 3.4.3.2 Particle rotation

The effect of particle rotation upon the macroscopic response of the granular structure is examined by comparing the responses of the reference particle structure defined in Table 3.3 for the cases with and without particle rotation. The latter case is obtained by prescribing the rotation of the inner particles $\mathcal{P}_p$ of the granular micro-structure to be zero, $\theta_p = 0$, throughout the entire loading process. For the boundary particles $\mathcal{P}_q$ the rotation follows from the periodicity requirement (3.12). Figure 3.10(a) shows the evolution of the stress ratio $\bar{\sigma}$ and Figure 3.10(b) illustrates the development of the volumetric deformation $\bar{J}_{rel}$ for the two cases. The ultimate failure strength of the system with constrained particle rotation appears to be more than $30\%$ higher than the ultimate failure strength of the system with unconstrained particle rotation. Essentially, limiting the particle rotation may be interpreted as a kinematic constraint that increases the shear strength (Bardet, 1994; Suiker and Fleck, 2004). Hence, granular materials composed of angular shaped particles, which are susceptible to interlocking, show limited particle rotation, and thus typically have a higher effective strength than granular materials composed of smooth, round particles (Lambe and Whitman, 1969). The deformation behaviour plotted in Figure 3.10(b) illustrates that the particle system with constrained rotation experiences more compaction than the particle system with unconstrained rotation. This result is consistent with the DEM study on relatively soft particle systems reported in (Bardet, 1994), and is due to larger particle overlap from the higher normal contact forces generated under constrained particle rotation. Note that the above trends are analogue to what has been observed in Figure 3.8 from constraining particle *sliding* by increasing the particle contact friction.

Figures 3.11(a) and (b) show the evolution of the coordination number $\bar{n}$ and the induced fabric anisotropy $\mathcal{A}$, respectively, for the simulations with constrained and unconstrained particle rotations. The coordination number decreases with deformation, and is smaller for the case of constrained particle rotation. Furthermore, from Figures 3.10a and 3.11b it is concluded that the shear strength is higher when the induced anisotropy is larger. More specifically, at an axial strain $\bar{\varepsilon} = 0.073$ the granular assembly with unconstrained particle rotation has reached its maximal shear strength, which is $0.39/0.48 = 0.81$ times lower than the corresponding strength of the granular assembly with constrained particle rotation. The anisotropy ratio for the two granular assemblies turns out to be similar, and at $\bar{\varepsilon} = 0.073$ equals $0.27/0.33 = 0.82$, thus indicating here an almost linear relation

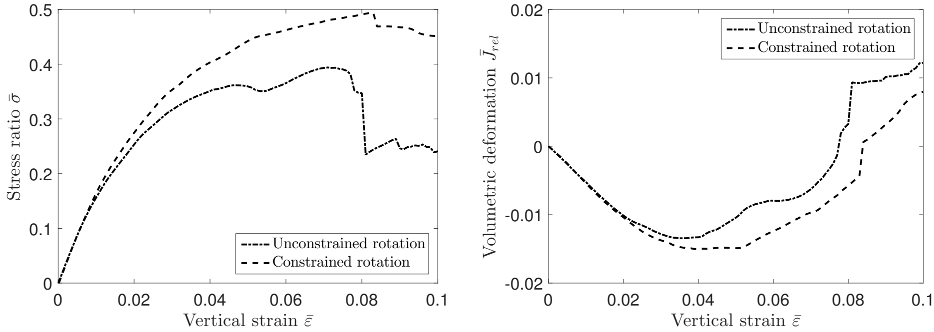

(a) (b)

**Figure 3.10:** (a) Average macroscopic stress ratio $\bar{\sigma}$ and (b) average volumetric deformation $\bar{J}_{rel}$ as a function of the applied vertical strain $\bar{\varepsilon}$ for constrained and unconstrained particle rotation.

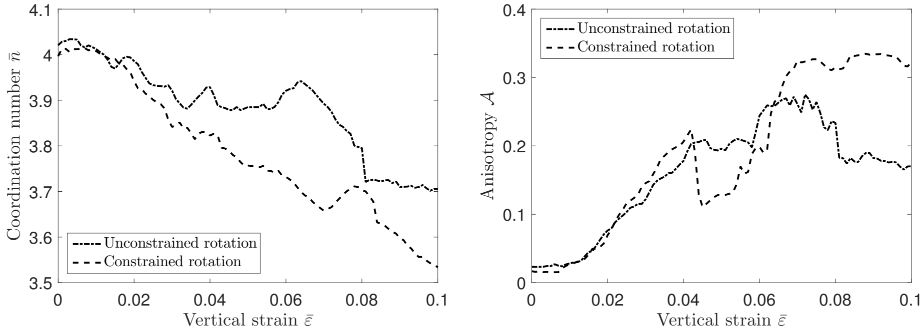

(a) (b)

**Figure 3.11:** (a) Average macroscopic coordination number $\bar{n}$ and (b) average induced anisotropy $\mathcal{A}$ as a function of the applied vertical strain $\bar{\varepsilon}$ for constrained and unconstrained particle rotations.

between shear strength and induced anisotropy.

#### 3.4.3.3 Initial anisotropy

The influence of the initial anisotropy of the granular micro-structure on the macro-scale response is assessed by considering, together with the reference particle packing defined in Table 3.3, two additional particle packings characterized by higher anisotropy values. Accordingly, the set of initial anisotropy parameters is $\mathcal{A}^0 = [0.02, 0.05, 0.08]$, and the corresponding microstructures and rose diagrams are shown in Figure 3.12. The evolutions of the effective stress and the volumetric deformation for the different initial fabric anisotropies are shown in Figures 3.13(a) and (b), respectively. The value of the peak strength appears to be lower for a higher initial fabric anisotropy, and is reached at a smaller axial strain

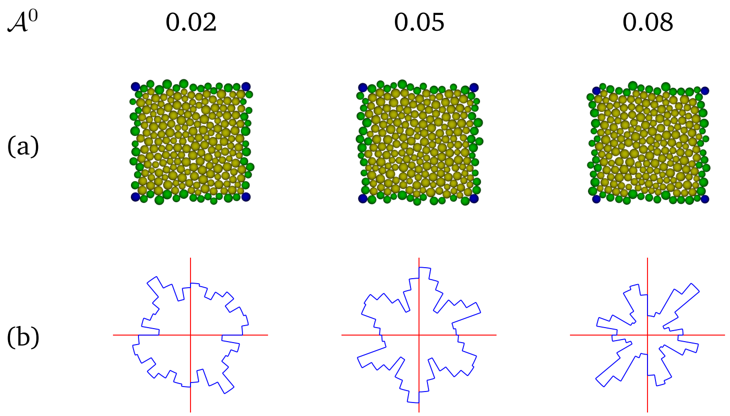

**Figure 3.12:** (a) Particle packings used to assess the effects of initial fabric anisotropy on the macro-scale response, and (b) the corresponding rose diagrams, for initial anisotropies $\mathcal{A}^0 = [0.02, 0.05, 0.08]$.

$\bar{\varepsilon}$. Further, in the pre-peak regime a higher initial fabric anisotropy creates less compaction of the granular packing, which agrees with the DEM study performed in (Kuhn, 1999). Combining the results from both figures leads to the conclusion that a higher compaction level obtained under a lower initial anisotropy provides a higher effective shear strength of the sample.

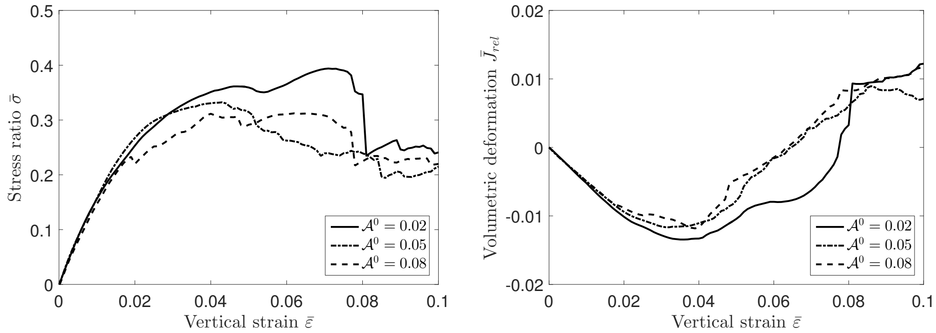

(a) (b)

**Figure 3.13:** (a) Average macroscopic stress ratio $\bar{\sigma}$ and (b) volumetric deformation $\bar{J}_{rel}$ as a function of the applied vertical strain $\bar{\varepsilon}$ for three packings with different values of the initial anisotropy $\mathcal{A}^0$.

The average coordination number $\bar{n}$ and the induced anisotropy $\mathcal{A}$ are illustrated in Figures 3.14(a) and (b) for the three different initial anisotropies. The structure with the lowest initial anisotropy $\mathcal{A} = 0.02$ clearly has the highest coordination number close to the onset of localized failure at $\bar{\varepsilon} = 0.07$, which corresponds to the highest compacting level and the largest overall strength, see Figure 3.13. For the other two anisotropies considered this relation is less clear, but may become more apparent when the number of particles in the micro-scale domain is enlarged. Further, the link between the initial anisotropy and the induced anisotropy depicted in Figure 3.14(b) can not be clearly established, although it can be observed that during progressive shear failure (i.e., in the deformation range $0.06 \leq \bar{\varepsilon} \leq 0.08$) the order of the three curves is similar as for the shear strength depicted in Figure 3.13a.

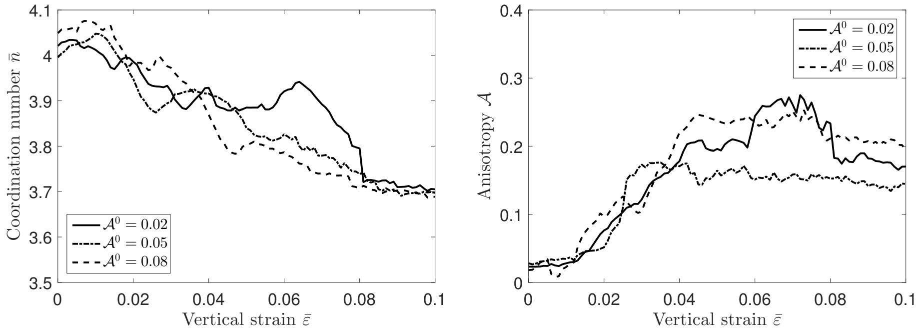

(a) (b)

**Figure 3.14:** (a) Average macroscopic coordination number $\bar{n}$ and (b) average induced anisotropy $\mathcal{A}$ as a function of the applied vertical strain $\bar{\varepsilon}$ for three packings with different initial anisotropy $\mathcal{A}^0$.

## 3.5 Conclusions

In the present contribution a multi-scale model for the analysis of granular systems has been proposed, which combines the principles of a coupled FEM-DEM approach with a novel servo-control methodology for the implementation of appropriate micro-scale boundary conditions. A mesh convergence study has been performed, whereby the results of a quasi-static biaxial compression test were compared to those obtained by direct numerical simulations. The comparison demonstrated the capability of the multi-scale method to realistically capture the macro-scale response, even for macroscopic domains characterized by a relatively coarse mesh; this makes it possible to accurately analyse large-scale granular systems in a computationally efficient manner. The multi-scale framework has been applied to study in a systematic manner the role of individual micro-structural characteristics on the effective macro-scale response. The effect of particle contact friction, particle rotation, and initial fabric anisotropy on the overall response has been considered, as measured in terms of the evolution of the effective stress, the volumetric deformation, the average coordination number and the induced anisotropy. The trends observed are in accordance with notions from physics, and observations from experiments and other DEM simulations presented in the literature. Accordingly, it is concluded that the present framework provides an adequate tool for exploring the effect of micro-structural characteristics on the macroscopic response of large-scale granular structures.

Since the proposed multi-scale framework is based on first-order homogenization principles, it can only be adequately applied for problems whereby microscopic length scale effects do not influence the macroscopic response. Examples whereby this separation of length scales holds are static (and dynamic) problems in which significant strain localization remains absent, and dynamic problems in which the time-dependent response is composed of non-dispersive, slowly varying low-frequency components. The extension of the proposed multi-scale FEM-DEM scheme for applications related to strain localization and high-frequency wave propagation is a topic for future research.

# Chapter 4
# Multi-scale dynamic simulation

In this Chapter, the multi-scale FEM-DEM method introduced in Chapter 3 is extended towards a dynamics formulation to simulate wave propagation in granular materials. In order to (explicitly) solve the macro-scale dynamic problem, the effective first Piola-Kirchhoff stress tensor and the effective density are required as input parameters at the integration point level. Using the hypothesis of a separation of length scales, i.e., the micro-structural length scale is much smaller than the characteristic length related to the macroscopic domain, the effective density is obtained from the densities of the microstructural components (particles, air) via a rule of mixtures. The macroscopic stress is computed for each time increment from a DEM simulation of the underlying granular assembly. The applicability and limitations of this approach are studied on a set of benchmark numerical examples. First, the model is validated for a one-dimensional string of particles, comparing the multi-scale solution with DNS results. Next, two-dimensional microstructures are considered, which reveal that the applicability of the method is dependent of the constitutive assumptions made at the micro-structural level. While for bond-elastic interactions the FEM-DEM solution and the DNS solution agree well, for compressive-elastic interactions the differences may become significant. This aspect constitutes a limitation of the method that should be addressed in future research.

## 4.1 Introduction

Understanding the response of granular materials to ground vibrations is particularly relevant for engineering applications, for instance to predict soil behaviour during earthquakes. Some experimental works in the literature deal with wave propagation in granular materials, for instance in order to determine the elastic stiffness of soil using the bender element test (O'Donovan et al., 2012b) or to measure the dynamic mechanical behaviour of cohesive granular materials (Zhang and Zhao, 2014). From the modelling viewpoint, the discrete element method (DEM) has often been used to study the dynamic response of granular materials (Sadd et al., 2000; Somfai et al., 2005; Mouraille et al., 2006; O'Donovan et al., 2012a). This approach has revealed that wave propagation in granular media may be affected by several factors, including fabric (Sadd et al., 2000), confining pressure (Somfai et al., 2005), particle friction (Mouraille et al., 2006) and loading frequency (O'Donovan et al., 2012a). However, DEM analyses are not suitable for representing large-scale engineering problems, due to the high number of degrees of freedom involved, which would require a substantial computational effort.

Alternatively, a multi-scale FEM-DEM solution strategy can be adopted, which relies on averaging theorems to relate force and displacement measures at the particle micro-scale to stress and strain measures at the macroscopic level (Kaneko et al., 2003; Miehe et al., 2010; Guo and Zhao, 2014; Shahin et al., 2016; Guo and Zhao, 2016b; Nguyen et al., 2014; Liu et al., 2016). Most of these works, however, focus on quasi-static problems only. The response of a granular material to shear wave propagation has been studied in (Liu et al., 2016). Despite that this is a valuable contribution, in this work the dynamic effective response was not compared against the results from direct numerical simulations (DNS) obtained from DEM models; moreover, the frequency range in which the long-wavelength based FEM-DEM model is valid was not analysed.

This chapter explores the applicability of the multi-scale FEM-DEM model proposed in Chapter 3 for wave propagation problems. The method is based on the assumption of a separation of the microscopic and macroscopic length scales. This allows to directly compute the effective density of the granular assembly via a rule of mixtures from the densities of the particles and the air. The macroscopic stress at each time increment is calculated from the solution of a DEM quasi-static problem defined on the underlying granular domain. The limitations of the method due to these hypotheses will be investigated.

The chapter is organized as follows. Section 4.2 presents a review of the formulation of the proposed multi-scale FEM-DEM model. Section 4.3 discusses the numerical implementation, for both the coupled FEM-DEM model and the DNS. In Section 4.4, numerical simulations are performed, which relate to wave propagation in a macroscopic domain associated to different micro-structural assemblies. Concluding remarks are finally provided in Section 4.5.

In terms of notations, the following notations will be used. The dyadic product of two vectors is denoted as $\mathbf{a} \otimes \mathbf{b} = a_i b_j \mathbf{e}_i \otimes \mathbf{e}_j$. Here $\mathbf{e}_i$, $\mathbf{e}_j$ and $\mathbf{e}_k$ are unit vectors in a Cartesian vector basis, and Einstein's summation convention is used on repeated tensor indices. The inner products between two vectors and two second-order tensors are given by $\mathbf{a} \cdot \mathbf{b} = a_i b_i$ and $\mathbf{A} : \mathbf{B} = A_{ij} B_{ij}$, respectively. The action of a second-order tensor on a vector is indicated as $\mathbf{A} \cdot \mathbf{b} = A_{ij} b_j \mathbf{e}_i$.

Field variables referring to the macroscopic scale will be indicated by an over-bar, for instance $\bar{\text{a}}$.

## 4.2 Computional homogenization for wave propagation

### 4.2.1 Working assumptions: separation of scales and long wavelength approximation

Computational homogenization is a multi-scale method that allows to derive the response of a material at the macroscopic, engineering scale from the analysis of the behaviour of the underlying micro-structural volume. First-order computational homogenization is based on the assumption of a strong separation of scales, i.e., the characteristic length at the macro-scale must be much larger than that at the micro-scale. In the particular case of granular materials, this can be formulated as

$$R_k \ll L\,, \tag{4.1}$$

where $R_k$ is the radius of particle $k$ in the micro-structural volume, and $L$ is the characteristic length scale related to the macroscopic domain, or the fluctuation length of the applied macroscopic deformation field (Kouznetsova et al., 2001). In the case of dynamic loading, this fluctuation length equals the shortest wavelength of the various waves generated in the granular structure, by which Equation (4.1) may be characterized as the *long wave approximation*. When the condition given by Equation (4.1) holds, the effective macroscopic density of the granular structure can be computed by using a rule of mixtures:

$$\bar{\rho} = \rho v_m\,, \tag{4.2}$$

where $\bar{\rho}$ is the macroscopic density, $\rho$ is the particle density and $v_m$ is the packing volume fraction (Sanchez-Palencia, 1980).

### 4.2.2 Macro-scale problem

Consider a macroscopic domain of undeformed volume $\Omega$ and boundary $\partial\Omega$. Based on the above assumptions, the domain can be described by a standard continuum. According to the conservation of linear momentum, the equation of motion in the reference configuration, neglecting body forces, is expressed by

$$\nabla \cdot \bar{\boldsymbol{P}} = \bar{\rho}\ddot{\bar{\mathbf{u}}}\,, \tag{4.3}$$

where $\bar{\boldsymbol{P}}$ is the first Piola-Kirchhoff stress and $\ddot{\bar{\mathbf{u}}}$ is the macroscopic acceleration. The conservation of angular momentum in the reference configuration reads

$$\bar{\boldsymbol{F}} \cdot \bar{\boldsymbol{P}}^T = \bar{\boldsymbol{P}} \cdot \bar{\boldsymbol{F}}^T\,, \tag{4.4}$$

where $\bar{\boldsymbol{F}} = \nabla \bar{\mathbf{x}}$ is the macroscopic deformation gradient calculated as the gradient of the current position $\bar{\mathbf{x}}$ with respect to the initial configuration. Equation (4.3) should be completed with appropriate boundary conditions, defined as

$$\bar{\mathbf{u}} = \bar{\mathbf{u}}^* \quad \text{on} \quad \partial\Omega^u \,, \tag{4.5}$$

$$\bar{\boldsymbol{P}} \cdot \mathbf{N} = \bar{\mathbf{t}}^* \quad \text{on} \quad \partial\Omega^t \,, \tag{4.6}$$

where $\bar{\mathbf{u}}^*$ is the prescribed displacement on the undeformed Dirichlet boundary $\partial\Omega^u$, $\mathbf{N}$ and $\bar{\mathbf{t}}^*$ are the outward unit normal and the prescribed traction on the undeformed Neumann boundary $\partial\Omega^t$, respectively. A constitutive specification linking the macroscopic deformation $\bar{\boldsymbol{F}}$ to the macroscopic stress $\bar{\boldsymbol{P}}$ is finally needed. In the framework of computational homogenization, this relation is obtained from the (nested) solution of a quasi-static boundary value problem defined on the micro-structural domain, as will be discussed later.

### 4.2.3 Micro-scale problem

The quasi-static micro-structural problem is formulated on an assembly of particles of undeformed volume $V$. The geometry and the governing equations for the micro-structural domain have been introduced in Chapter 3. The macro-scale deformation gradient $\bar{\boldsymbol{F}}$ is enforced on the boundary frame of the particle assembly via micro-structural boundary conditions. Despite that, in principle different boundary conditions may be selected (Liu et al., 2017), in this Chapter displacement boundary conditions are used.

Finally, to solve the micro-scale problem, the particle interaction must be specified by an appropriate contact law. An elastic model and a cohesive model are employed to prescribe the compressive-elastic interactions and the bond-elastic interactions between particles, respectively.

The elastic model describing the compressive-elastic interaction between particles relates the normal contact force $f_n$ to the normal overlap between two particles $\Delta u_n$, as

$$f_n = k_n \Delta u_n \,, \tag{4.7}$$

where $k_n$ is the normal contact stiffness.

The bond-elastic model assumes that two particles in contact are initially bonded via a linear relation between the force (or moment) and the corresponding relative displacement (or rotation) at the particle contact (Wang and Mora, 2008; Wang, 2009). This can be specified as

$$f_n^b = k_n^b \Delta u_n \quad , \quad f_s^b = k_s^b \Delta u_s \quad \text{and} \quad m_\theta^b = k_\theta^b \Delta \theta^b \,, \tag{4.8}$$

where $f_n^b$ is the bond force in the normal direction, $k_n^b$ is the bond normal stiffness, $\Delta u_n$ is the normal relative displacement between two particles, $f_s^b$ is the bond force in the tangential direction, $k_s^b$ is the bond shear stiffness, $\Delta u_s$ is the tangential relative displacement between two particles, $m_\theta^b$ is the moment inducing bending, $k_\theta^b$ is the bond bending stiffness, and $\Delta\theta^b$ is the relative angular displacement. When the bond breaks, the bond-elastic interaction changes into a compressive-elastic interaction in accordance with the failure criterion (Wang and Mora, 2008)

$$\frac{f_n^b}{f_n^{b,u}} + \frac{|f_s^b|}{f_s^{b,u}} + \frac{|m_\theta^b|}{m_\theta^{b,u}} = 1\,, \tag{4.9}$$

where $f_n^{b,u}$ is the (ultimate) tensile strength, $f_s^{b,u}$ is the shear strength and $m_\theta^{b,u}$ is the bending strength.

### 4.2.4 Multi-scale coupling

The macro-to-micro scale coupling is achieved by imposing the macro-scale deformation gradient $\bar{\boldsymbol{F}}$ on the boundary particles of the particle assembly. In a continuum setting, this scale transition relation requires that the macro-scale deformation gradient $\bar{\boldsymbol{F}}$ should be equal to the volume average of its micro-scale counterpart. For a granular packing, it reads (Miehe et al., 2010; Dettmar, 2006; Liu et al., 2017)

$$\bar{\boldsymbol{F}} = \frac{1}{V}\sum_{q=1}^{Q} \boldsymbol{x}_q \otimes \boldsymbol{A}_q\,, \tag{4.10}$$

where $V$ is the initial volume covered by the granular packing, $Q$ is the total number of boundary particles, $\boldsymbol{x}_q$ is the current position vector of the centroid of boundary particle $q$, and $\boldsymbol{A}_q$ is the initial area vector of particle $q$. Condition (4.10) is enforced by imposing displacement boundary conditions, i.e.

$$\boldsymbol{x}_q = \bar{\boldsymbol{F}} \cdot \boldsymbol{X}_q\,, \tag{4.11}$$

with $\boldsymbol{X}_q$ the position vector of the centroid of particle $q$ in the original configuration.

On the other hand, the transition from the micro-scale to the macro-scale is obtained by returning to the macro-scale problem the first Piola-Kirchhoff stress $\bar{\boldsymbol{P}}$ computed from the micro-structural analysis. The stress averaging relation requires the macroscopic first Piola-Kirchhoff stress $\bar{\boldsymbol{P}}$ to be equal to the volume average of its microscopic counterpart. In a discrete setting, the macroscopic first Piola-Kirchhoff stress may be defined as (Miehe et al., 2010; Liu et al., 2017)

$$\bar{\boldsymbol{P}} = \frac{1}{V}\sum_{q=1}^{Q} \boldsymbol{a}_q \otimes \boldsymbol{X}_q\,, \tag{4.12}$$

with $\boldsymbol{a}_q$ the boundary force acting on particle $q$.

For a granular medium, Equation (4.10) and Equation (4.12) satisfy the Hill-Mandel condition (Hill, 1963) that expresses the equality between the virtual work done at a macroscopic material point to the volume average of the virtual work done at the micro-structural level. This condition may be written as (Miehe et al., 2010; Liu et al., 2017)

$$\bar{\boldsymbol{P}} : \delta\bar{\boldsymbol{F}} = \frac{1}{V}\sum_{q=1}^{Q} \boldsymbol{a}_q \cdot \delta\boldsymbol{x}_q \,. \tag{4.13}$$

# 4.3 Numerical implementation

## 4.3.1 Macro-scale problem

### 4.3.1.1 Finite element formulation

The macro-scale problem is solved by using a finite element formulation based on the theory of large deformations. To this aim, introducing the test functions $\delta\bar{\mathbf{u}}$ and $\delta\bar{\mathbf{F}} = \nabla(\delta\bar{\mathbf{u}})$, the weak form of the dynamic macroscopic equilibrium (4.3) is obtained, i.e.,

$$\int_{\partial\Omega} \delta\bar{\mathbf{u}} \cdot \bar{\mathbf{t}} \, \mathrm{d}\partial\Omega - \int_{\Omega} \delta\bar{\mathbf{F}} : \bar{\boldsymbol{P}} \, \mathrm{d}\Omega = \int_{\Omega} \delta\bar{\mathbf{u}} \cdot \bar{\rho}\ddot{\bar{\mathbf{u}}} \, \mathrm{d}\Omega \,. \tag{4.14}$$

Equation (4.14) is discretized according to the Galerkin method, by writing the continuous displacement $\bar{\mathbf{u}}$ and acceleration $\ddot{\bar{\mathbf{u}}}$ fields in terms of finite element interpolation functions. This leads to a system of non-linear algebraic equations

$$\mathbf{f}_{ext} - \mathbf{f}_{int} = \bar{\mathbf{M}}\ddot{\boldsymbol{\mathcal{U}}} \,, \tag{4.15}$$

where the vectors $\boldsymbol{\mathcal{U}}$ and $\ddot{\boldsymbol{\mathcal{U}}}$ contain the nodal values of the macroscopic displacement $\bar{\mathbf{u}}$ and acceleration $\ddot{\bar{\mathbf{u}}}$ fields, respectively. In (4.15), the external force $\mathbf{f}_{ext}$, the internal force $\mathbf{f}_{int}$, and the consistent mass matrix $\bar{\mathbf{M}}$ are defined as

$$\mathbf{f}_{ext} = \int_{\partial\Omega} \boldsymbol{\mathcal{N}}^T \bar{\mathbf{t}} \, \mathrm{d}\partial\Omega \quad \text{and} \quad \mathbf{f}_{int} = \int_{\Omega} \boldsymbol{\mathcal{B}}^T \bar{\boldsymbol{P}}(\boldsymbol{\mathcal{U}}) \, \mathrm{d}\Omega \quad \text{and} \quad \bar{\mathbf{M}} = \int_{\Omega} \boldsymbol{\mathcal{N}}^T \bar{\rho} \boldsymbol{\mathcal{N}} \, \mathrm{d}\Omega \,, \tag{4.16}$$

with $\boldsymbol{\mathcal{N}}$ and $\boldsymbol{\mathcal{B}}$ matrices containing the interpolation functions and their (spatial) derivatives, respectively. Considering that the explicit time integration scheme is used, instead of the consistent mass matrix $\bar{\mathbf{M}}$ defined above, the lumped mass matrix is employed. This allows to reduce the numerical approximation error in the solution, as explained in (de Borst and Sluys, 2015). The lumped mass matrix of element $e$ is defined by its diagonal components at nodes $k = 1, ...K$ according to (Zienkiewicz and Taylor, 1991)

$$M^e_{kk} = \frac{\int_{\Omega_e} \mathcal{N}_k^2 \mathrm{d}\Omega}{\sum_{k=1}^{K} \int_{\Omega_e} \mathcal{N}_k^2 \mathrm{d}\Omega} \int_{\Omega_e} \bar{\rho} \mathrm{d}\Omega \,, \tag{4.17}$$

where $K$ is the total number of nodes of element $e$, $\mathcal{N}_k$ is the shape function referring to node $k$, and $\bar{\rho}$ is the macroscopic density obtained from Equation (4.2).

#### 4.3.1.2 Explicit time integration

A first-order finite difference scheme is used to integrate the equation of motion (4.15). First, the acceleration field is calculated. Next, the velocity and the displacement fields are updated, in accordance with the following relationships:

$$\ddot{\mathcal{U}}^{n+1} = \frac{\mathbf{f}_{ext} - \mathbf{f}_{int}}{\bar{\mathbf{M}}}\,, \tag{4.18}$$

$$\dot{\mathcal{U}}^{n+1} = \dot{\mathcal{U}}^{n} + \ddot{\mathcal{U}}^{n+1}\Delta t\,, \tag{4.19}$$

$$\mathcal{U}^{n+1} = \mathcal{U}^{n} + \dot{\mathcal{U}}^{n+1}\Delta t\,, \tag{4.20}$$

with $\Delta t$ the incremental time step. In the computational homogenization procedure, the internal force $\mathbf{f}_{int}$ depends on the DEM quasi-static solution of the micro-scale problem associated to each Gauss point. The detailed solution procedure for the DEM quasi-static problem and the FEM-DEM coupled problem can be found in Chapter 3.

### 4.3.2 Direct numerical simulation

In order to assess the performance of the coupled FEM-DEM model in simulating wave propagation in granular materials, the results obtained from computational homogenization have to be compared to those computed from a direct numerical simulation performed with the DEM method. For a granular assembly composed of $N$ particles, the dynamic equilibrium equation for particle $i$ can be written as

$$\mathbf{M}_i\ddot{\mathbf{d}}_i = (\mathbf{p}_r)_i \qquad \text{for} \qquad i = 1...,N\,, \tag{4.21}$$

where the mass matrix $\mathbf{M}_i = \mathrm{diag}\,[M_i, I_i]$ includes the particle mass $M_i$ and the mass moment of inertia $I_i = 1/2\ M_iR_i^2$, with $R_i$ the particle radius. The term $\ddot{\mathbf{d}}_i$ represents the generalized acceleration vector, which is integrated twice to obtain the generalized coordinate vector $\mathbf{d}_i = [\mathbf{x}_i,\ \boldsymbol{\theta}_i \cdot \mathbf{e}_3]^T$. The latter vector contains the current locations of the particle centroids $\mathbf{x}_i$ and the particle rotations $\boldsymbol{\theta}_i$. Finally, the vector $\mathbf{p}_r = [\mathbf{f}_r,\ \mathbf{m}_r \cdot \mathbf{e}_3]^T$ is the generalized force vector composed of the resultant force $\mathbf{f}_r$ and moment $\mathbf{m}_r$ acting on particle $i$.

Equation (4.21) is integrated by using an explicit, first-order finite difference scheme. For each time step $t_{n+1}$, this allows for an explicit update of the particle acceleration, velocity and displacement.

## 4.4 Computational results

### 4.4.1 Overview of the simulations

The reference macroscopic domain consists of a rectangular body of length $l$ and height $h$, as illustrated in Figure 4.1. The left boundary is supported both in the horizontal and vertical direction, and the top and bottom boundaries are supported in the vertical direction. The right boundary is subjected to a half-sine displacement pulse, $\bar{u}(t) = A\sin(2\pi t/T)$ for $0 \leq t \leq T/2$, where $A$ is the amplitude of the pulse and $T$ is the period.

The macroscopic response will be computed for different underlying microstructures: i) a one-dimensional string of $n$ particles, see Figure 4.2; ii) a regular mono-disperse packing of 255 particles, see Figure 4.3(a); iii) an irregular polydisperse packing of 228 particles, see Figure 4.3(b). In all the cases, the solution of the FEM-DEM method will be compared to that of a corresponding direct numerical simulation. Note that the mono-disperse packing in principle could have been taken smaller due to the regularity of the microstructure. However, for simplicity the size of the regular packing is taken similar to that of the irregular polydisperse packing.

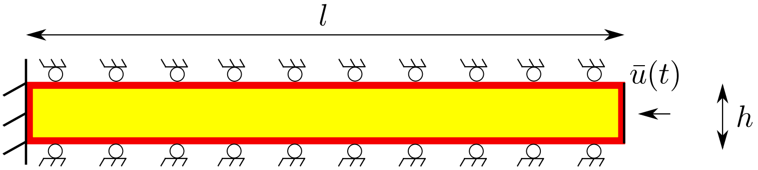

**Figure 4.1:** Displacement boundary conditions for the FEM-DEM model.

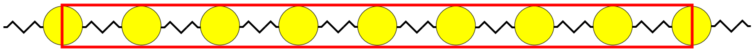

**Figure 4.2:** a string of $n$ particles.

(a) (b)

**Figure 4.3:** (a) regular packing of 255 particles, and (b) polydisperse packing of 228 particles.

### 4.4.2 Benchmark one dimensional problem: string of bond-elastic particles

The coupled FEM-DEM framework is first used to investigate the response of a one-dimensional string of bond-elastic particles, see Figure 4.2, whereby the particles are characterized by a bond-elastic constitutive interaction given by Equation (4.8).

#### 4.4.2.1 Analytical expressions for effective density and stress

The effective response of a string of $n$ bond-elastic particles can be computed analytically. Based on Equation (4.2), the effective density $\bar{\rho}$ of the string of particles is calculated as

$$\bar{\rho} = \rho \frac{V_p}{V} = \frac{(n-1)\pi R^2}{4R^2(n-1)} = \rho \frac{\pi}{4}\,, \tag{4.22}$$

where $\rho$ is the particle density, $V_p$ is the particle volume, $V$ is the total volume, and $R$ is the particle radius. Note that the effective density $\bar{\rho}$ does not depend on the particle number $n$ and the particle radius $R$. For a deformation-controlled loading condition in the 1-direction, the applied deformation gradient tensor may be generally written as $\bar{\boldsymbol{F}} = F_{11}\boldsymbol{e}_1 \otimes \boldsymbol{e}_1 + F_{12}\boldsymbol{e}_1 \otimes \boldsymbol{e}_2 + F_{21}\boldsymbol{e}_2 \otimes \boldsymbol{e}_1 + F_{22}\boldsymbol{e}_2 \otimes \boldsymbol{e}_2$, with $F_{11} = a$, $F_{12} = F_{21} = 0$ and $F_{22} = 1$. Considering that the normal force between two particles (both in tension and compression) is given by Equation $(4.8)_1$, and that the relative particle displacement between two particles may be expressed as $\Delta u_n = 2R(F_{11} - 1)$, a combination of these two relations allows to write the force vector as $\boldsymbol{a}_q = \left(2Rk_n^b\,(F_{11} - 1)\,, 0\right)$. Furthermore, the position vector indicating the center of particle $n$ is expressed as $\boldsymbol{X}_q = (2R\,(n-1)\,, 0)$, so that, with Equation (4.12), the first Piola-Kirchhoff stress tensor becomes

$$\bar{\boldsymbol{P}} = \frac{1}{4R^2(n-1)} \begin{bmatrix} k_n^b(F_{11}-1)(n-1)(2R)^2 & 0 \\ 0 & 0 \end{bmatrix} = \begin{bmatrix} k_n^b(a-1) & 0 \\ 0 & 0 \end{bmatrix}. \tag{4.23}$$

Note that the stress does not depend on the particle size or number, so that the string of particles may be unconditionally considered as a *representative volume element* (RVE). Hence, this micro-structure is very suitable for analyzing mesh convergence aspects with the FEM-DEM framework, since the accuracy of the response computed hereby only is determined by the FEM discretization, and does not depend on the size of the RVE. The mesh convergence behaviour is one of the aspects examined in the section below, which is done by means of a comparison of the FEM-DEM solution to the exact DNS solution (computed by DEM).

#### 4.4.2.2 Coupled FEM-DEM solution and comparison to DNS

The coupled FEM-DEM numerical procedure presented in Section 4.3 is applied to solve the dynamics problem illustrated in Figure 4.1. The dimensions of the macro-scale domain are $l \times h = 800R \times 2R$, in correspondence with a string of $400$ circular particles. The domain is discretized by using 4-node iso-parametric elements with one-point Gauss quadrature. In the mesh convergence study four different finite element meshes are considered, with the number of elements equal to $n_e = [40 \times 1; 80 \times 1; 200 \times 1; 400 \times 1]$. The period of the half-sine pulse applied at the right boundary is $T = 5$ ms and the amplitude is $A = 1.8$ mm. The macro-scale density and stress, represented by Equations (4.22) and (4.23), serve as input for expressions (4.17) and $(4.16)_2$, respectively.

Additionally, a DNS is performed on a string of 400 bonded particles with elastic contact interactions. The corresponding micro-structural parameters are listed in Table 4.1. Note that the bond tensile strength and the tangential and bending strengths are given artificially high values to ensure that the particles maintain a cohesive response, i.e., bond failure can not occur. The values listed for the tangential and bending strengths and stiffnesses are not relevant for the present simulations, but will be used in subsequent simulations related to 2-dimensional granular micro-structures.

**Table 4.1:** Geometrical and physical parameters used in DEM simulation.

| Parameter | Value | Unit |
|---|---|---|
| Elastic normal stiffness $k_n = k_n^b$ | $1 \times 10^4$ | N/m |
| Elastic tangential stiffness $k_s = k_s^b$ | $4 \times 10^3$ | N/m |
| Elastic bending stiffness $k_\theta^b$ | $0 \times 10^3$ | N/m |
| Bond tension strength $f_n^{b,u}$ | $3 \times 10^6$ | N |
| Bond tangential strength $f_s^{b,u}$ | $6 \times 10^6$ | N |
| Bond bending strength $m_\theta^{b,u}$ | $2 \times 10^6$ | Nm |
| Particle radius $R$ | $1.1 \times 10^{-3}$ | m |
| Particle density $\rho$ | $2 \times 10^3$ | kg/m$^3$ |
| Translational damping $\alpha$ | 0.7 | – |
| Rotational damping $\beta$ | 0.7 | – |
| Time increment $\Delta t$ | $10^{-6}$ | s |

Figure 4.4 illustrates the time evolution of the axial displacement (normalized with respect to the amplitude $A$ of the half-sine pulse) at nodes located at a distance of $20R$ (10 particles) and $100R$ (50 particles) from the right boundary of the macroscopic domain (at which the half-sine pulse is applied). The response is shown for the four different FEM discretizations considered, together with the DNS result. Further, the half-sine pulse load signal is illustrated as a reference. It can be observed that for an increasing number of elements the displacement response computed by the FEM-DEM model converges towards that of the DNS model. Additionally, the displacement profile at a distance of $100R$ from the source, plotted in Figure 4.4(b), requires a somewhat finer mesh for convergence than the displacement profile at a distance of $20R$, depicted in Figure 4.4(a). This is due to the fact that mesh discretization effects of a relatively short wavelength, which are most apparent at the end of the response signal, tend to grow in amplitude with increasing travelling distance of the compression wave. However, for the finest mesh of $n_e = 400$ elements, these discretization effects seem to have vanished.

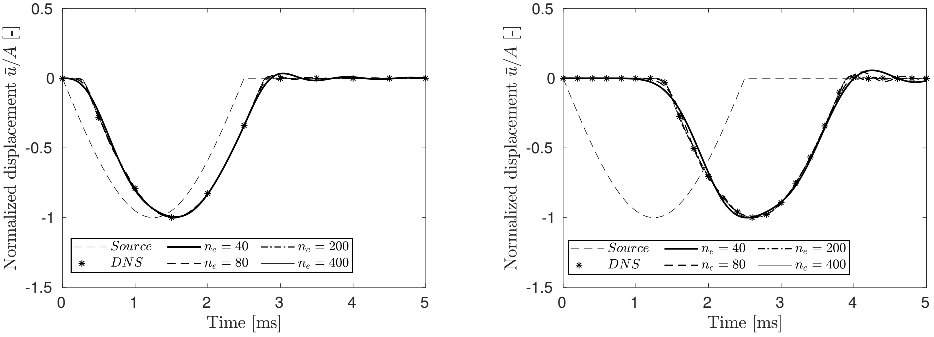

(a) (b)

**Figure 4.4:** Time evolution of the displacement response of FEM models with four different mesh sizes (solid lines), together with the DNS solution (asterisk symbols). The displacement half-sine pulse applied (dashed line) is plotted for comparison. (a) Response at a distance of $20R$ (10 particles) from the right boundary, and (b) Response at a distance of $100R$ (50 particles) from the right boundary.

#### 4.4.2.3 Wave dispersion effects

The first-order FEM-DEM framework presented in Section 4.2 is formally valid under the long wave approximation given by Equation (4.1). However, for the one-dimensional string of particles depicted in Figure 4.2, it is expected to give accurate results in the range of short wavelengths as well, as for this microstructure the effective density and stress are independent of the size of the RVE, see Equations (4.22) and (4.23). In order to investigate the dynamic response under relatively short wavelengths, the period of the half-sine pulse is varied as $T = [0.5, 1, 2, 5]$ ms. Note that the maximal value of $T = 5$ ms corresponds to the period used in the analyses presented in the previous section.

The phase velocity of a string of bonded elastic particles in the long-wave limit can be expressed as (Suiker and de Borst, 2005)

$$c^{\infty} = \sqrt{\frac{4k_n R^2}{M}}\,, \tag{4.24}$$

with $k_n$ the particle normal stiffness and $M$ the particle mass. The 2D simulations were performed for a string of cylindrical particles of radius $R = 1.1$ mm and a thickness of $1$ mm, which, with the parameter values listed in Table 4.1, via Equation (4.24) results in a phase velocity of $c \approx 80$ mm/ms. Correspondingly, the wavelengths related to the four pulse periods selected become $\lambda = c^{\infty}T \approx [36; 72; 144; 364]\,R$.

Figure 4.5 shows the time evolution of the normalized horizontal displacement for the four different pulse periods, as obtained with an FEM model of $n_e = 400 \times 1$ elements (which is the finest mesh examined in the mesh convergence study of the previous section), and from the DNS solution. Figures 4.5(a) and (b) refer to nodes located at $20R$ (10 particles) and $100R$ (50 particles) from the right boundary, respectively.

It can be observed that the FEM-DEM results and DNS results match closely for all pulse periods analyzed. Furthermore, for the shortest pulse periods, $T = 0.5$ ms and $T = 1.0$ ms, wave dispersion effects become prominent, as characterized by the oscillatory pattern of relatively high frequency appearing at the end of the response signal. The reason that these high-frequency components propagate relatively slow follows from the typical sinusoidal shape of the $\omega - k$ dispersion curve characterizing a string of elastic particles, see Suiker and de Borst (2005); this shape of the dispersion curve causes the group velocity (= the velocity at which the wave energy propagates) to decrease with increasing frequency, whereby it finally becomes zero at the maximum frequency for a propagating wave, $\omega_{max} = 2\sqrt{k_n/M}$, thereby resulting in a standing wave.

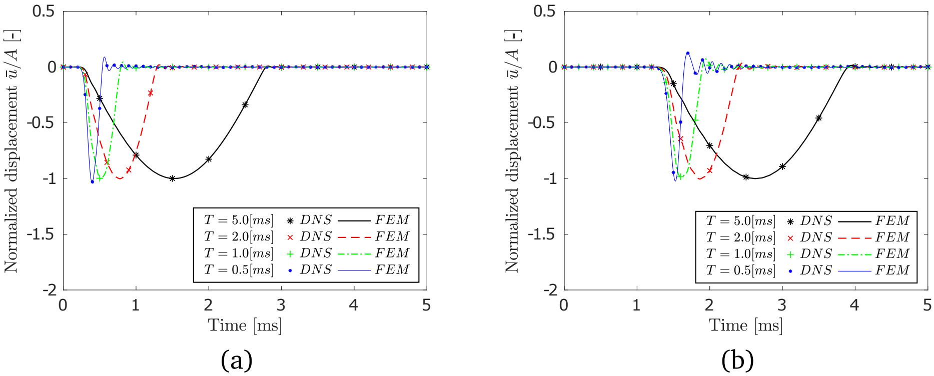

(a) (b)

**Figure 4.5:** Horizontal displacement response (normalized) under half-sine pulses of different period. The response signals are recorded at (a) $20R$ and (b) $100R$ from the right boundary of the macroscopic domain (at which the half-sine pulse is applied).

### 4.4.3 Regular monodisperse packing

In this Section, the macroscopic domain illustrated in Figure 4.1 is associated to the underlying micro-structural geometry represented by the regular monodisperse packing of 255 particles shown in Figure 4.3(a). The packing has dimensions $30.5 \times 30.8$ mm$^2$. The dynamic response in the macroscopic domain will be studied by considering two different constitutive interactions between the particles in the micro-structure: a bond-elastic interaction (i.e., elastic interaction both in tension and compression) and a compressive-elastic interaction (i.e., elastic interaction in compression, no interaction in tension).

#### 4.4.3.1 Packing with bond-elastic particle interactions

A granular micro-structure with a bond-elastic interaction - see Equation (4.8) - is considered first. The constitutive parameters related to the particle contacts are presented in Table 4.1. The macro-scale domain size is specified as $l \times h = 1219.4 \times 30.8$ mm$^2$, thus representing a composition of 40 micro-structural geometries in the longitudinal direction of the domain. A mesh convergence study is performed, by considering the macroscopic domain to be discretized with 4-node iso-parametric elements with one-point Gauss quadrature. Here, the number of elements equals $n_e = [40 \times 1; 80 \times 1; 160 \times 1; 320 \times 1]$. A half-sine displacement pulse with a period $T = 5$ ms and an amplitude $A = 5$ mm is applied at the right boundary of the macroscopic domain. The results of the coupled FEM-DEM analyses for the different FEM meshes considered are shown in Figure 4.6. The average of the horizontal displacements of the nodes located at $30.5$ mm (corresponding to a distance of one micro-structural geometry) and $305$ mm (corresponding to a distance of 10 micro-structural geometries) from the right boundary of the macroscopic domain (which is where the half-sine pulse is applied), normalized by the pulse amplitude, are illustrated in Figures 4.6(a) and (b), respectively. A DNS is also performed, in which the rectangular specimen is described by a DEM model of $9615$ particles. It can be observed that for an increasing number of elements in the FEM model, the FEM-DEM displacement response clearly converges to the DNS displacement response (represented by the average

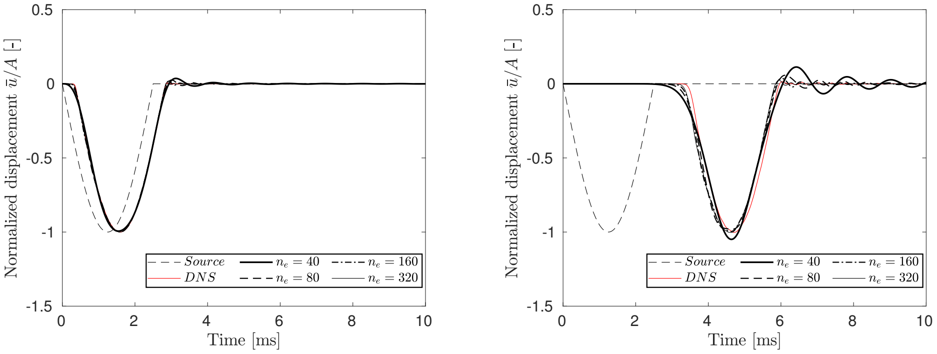

(a) (b)

**Figure 4.6:** Time evolution of the (normalized) horizontal displacement response of FEM-DEM models with four different mesh sizes (black lines), whereby the underlying micro-structure is a *regular packing* with *bond-elastic* interactions between the particles. The DNS solution (red line), and the half-sine displacement pulse applied (dashed line), are plotted for comparison. The displacement is evaluated at locations (a) $30.5$ mm (corresponding to a distance of one micro-structural geometry) and (b) $305$ mm (corresponding to a distance of 10 micro-structural geometries) from the right boundary of the macroscopic domain.

particle displacement over the sample height at the specific location considered). As observed before in Figure 4.4 for the one-dimensional string of particles, a comparison of Figures 4.6(a) and (b) illustrates that the displacement response closer to location of the pulse load accurately approaches the DNS response at a somewhat coarser mesh.

#### 4.4.3.2 Packing with compressive-elastic particle interactions

The FEM-DEM response is now investigated by considering a micro-structural packing of particles with a compressive-elastic contact interactions, as represented by Equation (4.7). The material parameters used are listed in Table 4.1. The macro-scale dimensions are $l \times h = 792.6 \times 30.8\ \text{mm}^2$. The macroscopic domain is discretized into four different meshes, which are characterized by the following number of elements: $n_e = [26 \times 1; 52 \times 1; 104 \times 1; 208 \times 1]$. A corresponding DNS is considered, where the macroscopic domain consists of $6255$ particles. The half-sine displacement pulse applied at the right boundary of the macroscopic domain is characterized by a period $T = 5.0$ ms and an amplitude $A = 1.8$ mm.

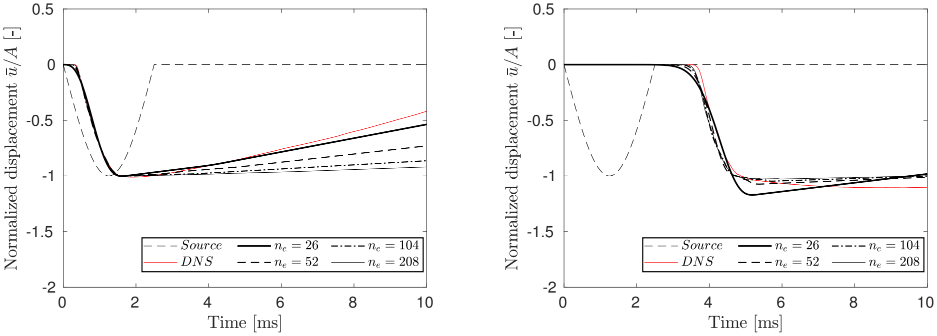

(a) (b)

**Figure 4.7:** Time evolution of the (normalized) horizontal displacement response of FEM-DEM models with four different mesh sizes (black lines), whereby the underlying micro-structure is a *regular packing* with a *compressive-elastic* interaction between the particles. The DNS solution (red line), and the displacement-driven half-sine pulse applied (dashed line), are plotted for comparison. The displacement is evaluated at locations (a) $30.5$ mm (corresponding to a distance of one micro-structural geometry) and (b) $305$ mm (corresponding to a distance of 10 micro-structural geometries) from the right boundary of the macroscopic domain.

The horizontal displacement response to the pulse loading is illustrated in Figure 4.7 for the different FEM meshes considered. Note that the displacement response here is *not* characterized by a sinusoidal shape similar to that of the pulse load, since, due to a compressive-elastic particle interaction, the tensile force required to pull the particles back to their original position can not develop.

At the initial stage, i.e., before the displacement response reaches its maximum, the response of the FEM-DEM models is close to that of the DNS. After passing the maximum value, the displacement predicted by the FEM-DEM model starts to deviate from the DNS solution. Moreover, as can be clearly observed from Figure 4.7(a), the difference between the multi-scale solution and the result obtained by the DNS may be larger for a finer mesh. This characteristic can yet not be explained, and needs to be addressed in future work.

## 4.4.4 Irregular poly-disperse packing

The dynamic analysis is finally performed assuming an irregular polydisperse packing as the underlying micro-structure associated to the macroscopic domain, see Figures 4.1 and 4.3(b). The packing is initially (almost) isotropic and is characterized by 228 particles. Its dimensions are $30 \times 30$ mm$^2$. It has been verified that this packing size is sufficient to be statistically representative for computing the effective response under the present dynamic loading conditions. In the following, the multi-scale problem will be solved by successively considering both bond-elastic particle interactions and compressive-elastic particle interactions.

### 4.4.4.1 Packing with bond-elastic particle interactions

A granular packing characterized by bond-elastic interactions is considered first. The constitutive parameters are specified in Table 4.1. The macro-scale domain, which has dimensions $l \times h = 1200 \ \times 30$ mm$^2$, is discretized into four different finite element meshes, characterized by the number of elements $n_e = [40 \times 1; 80 \times 1; 160 \times 1; 320 \times 1]$. The FEM mesh is constructed by using 4-node iso-parametric elements with one-point Gauss quadrature. The corresponding DNS model has $8535$ particles. A half-sine displacement pulse with a period $T = 5$ ms and an amplitude $A = 1.8$ mm is applied.

Figure 4.8 shows the (normalized) displacement response averaged across two different cross-sections, located (a) $30$ mm (corresponding to a distance of one microstructural geometry) and (b) $300$ mm (corresponding to a distance of 10 microstructural geometries) from the right boundary at which the load is applied. Close to the source, the multi-scale response is in good agreement with the response of the DNS model, even for the relatively coarse meshes, see Figure 4.8(a). However, at the location further from the loading source, the displacement for the two coarsest meshes show some oscillations at the end of the response signal, which are likely to be the result of numerical dispersion (i.e., the effect of the finite element size on the dynamic response under shorter wavelength), see Figure 4.8(b). In addition, the response by the multi-scale simulations shows a small time shift compared to that of the DNS.

Figures 4.9(a) and (b) show the time evolution of the stress normal to the top boundary, evaluated at $15$ mm (corresponding to the location of the integration point in the first element) and $285$ mm (corresponding to the location of the integration point in the 10th element) from the right boundary. The response

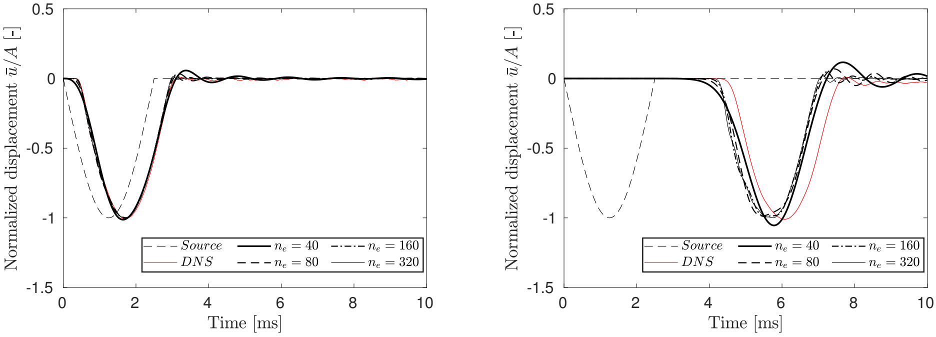

(a) (b)

**Figure 4.8:** Time evolution of the (normalized) horizontal displacement response of FEM-DEM models with four different mesh sizes (black lines), whereby the underlying micro-structure is an *irregular polydisperse packing* with a *bond-elastic* interaction between the particles. The DNS solution (red line), and the displacement-driven half-sine pulse applied (dashed line), are plotted for comparison. The displacement is evaluated at locations (a) 30 mm (corresponding to a distance of one micro-structural geometry) and (b) 300 mm (corresponding to a distance of 10 micro-structural geometries) from the right boundary of the macroscopic domain.

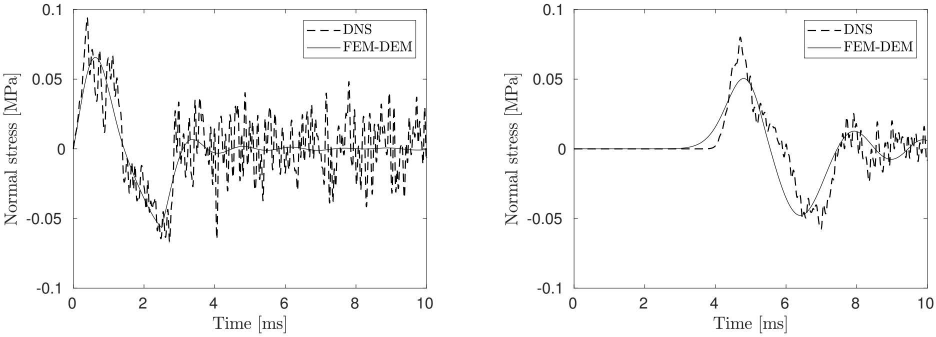

(a) (b)

**Figure 4.9:** Stress response normal to the top boundary of the FEM-DEM model ($n_e = 40$ elements) and the DNS model, evaluated at positions (a) $15$ mm, (b) $285$mm from the loading source. The underlying micro-structure is an *irregular packing* with *bond-elastic* interactions.

of the FEM-DEM model is computed using a mesh with $n_e = 40 \times 1$ elements. Accordingly, the element size here corresponds with the size of the particle microstructure. For the DNS the stress in Figures 4.9(a) and (b) is computed by summing up the boundary forces over a distance of $0$-$30$ mm and $270$-$300$ mm from the right boundary, respectively, and dividing the result by the corresponding distance of $30$ mm (which thus equals the element length in the FEM-DEM model). Both for the multi-scale model and the DNS the stress response initially is compressive, followed by a tensile part (= negative stress value) of a somewhat lower amplitude. Due to non-uniform motions of individual particles, for the DNS the stress response oscillates around the more smooth response computed with the multi-scale model. The reason that the high-frequency oscillations remain absent in the multiscale model, is because the response of the granular microstructure here is based on a quasi-static analysis. The normal stress at the top edge results from the constraining effect caused by vertical supports. Note that the stress computed by the FEM-DEM model somewhat decreases in amplitude, which may be the result of numerical dispersion caused by the interaction between the generated wavelengths and the relatively coarse element size.

#### 4.4.4.2 Packing with compressive-elastic particle interactions

The micro-structural irregular packing associated to the macroscopic domain is now characterized by compressive-elastic particle interactions. The constitutive properties are listed in Table 4.1. The domain size of the macroscopic domain is $l \times h = 780 \times 30 \ \text{mm}^2$. The macro-scale geometry is discretized into four finite element meshes, with the number of elements $n_e = [26 \times 1; 52 \times 1; 104 \times 1; 208 \times 1]$. The corresponding DNS model consists of $5553$ particles. The applied half-sine displacement pulse and the type of elements used are the same as for the regular granular packing.

Figure 4.10 shows the time evolution of the horizontal displacement averaged across the cross-section, evaluated at locations $30$ mm (corresponding to a distance of one micro-structural geometry) and $300$ mm (corresponding to a distance of 10 micro-structural geometries) from the loading source. The corresponding multi-scale solutions are comparable to those computed for the regular packing, see Figure 4.7. Nonetheless, the difference with the corresponding DNS solutions is significant, which is an issue that currently can not be explained and therefore requires a more detailed investigation.

The time evolution of the stress normal to the top edge, evaluated at distances $15$ mm and $285$ mm from the right edge at which the loading is applied, are shown in Figures 4.11(a) and (b), respectively, for a granular structure with compressive-elastic particle interactions. The DNS responses plotted for comparison are computed by summing up the boundary forces over the distances $0 - 30$ mm and $270 - 300$ mm from the right boundary, and dividing these sums by the corresponding length of $30$ mm. The DNS responses and multi-scale responses approximately show the same trend, which is initially represented by a compressive stress pulse that approaches to zero when time progresses. Comparing the responses plotted in Figures 4.11(a) and (b) illustrate that the amplitude of the compressive pulse slightly decreases with propagation distance, while its period somewhat increases. These are typical wave dispersion effects. Note further that the tensile part of the stress response present in Figure 4.9 for the bond-elastic

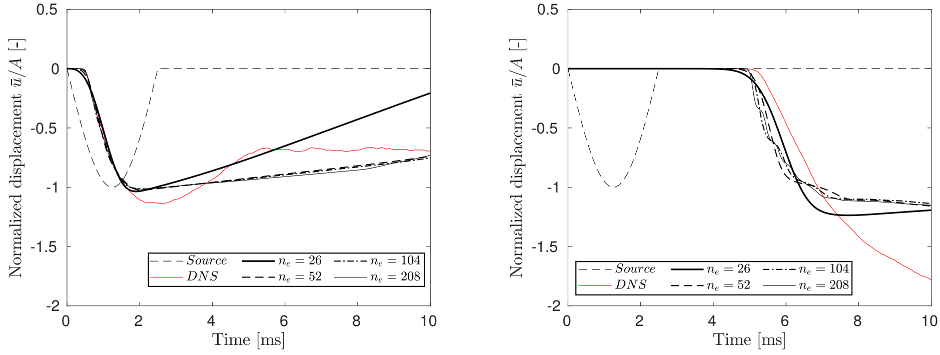

(a) (b)

**Figure 4.10:** Time evolution of the (normalized) horizontal displacement response of FEM-DEM models with four different mesh sizes (black lines), whereby the underlying micro-structure is an *irregular polydisperse packing* with *compressive-elastic* particle interactions. The DNS solution (red line), and the displacement-driven half-sine pulse applied (dashed line), are plotted for comparison. The displacement is evaluated at locations (a) $30$ mm (corresponding to a distance of one micro-structural geometry) and (b) $300$ mm (corresponding to a distance of 10 micro-structural geometries) from the right boundary of the macroscopic domain (at which the half-sine pulse is applied).

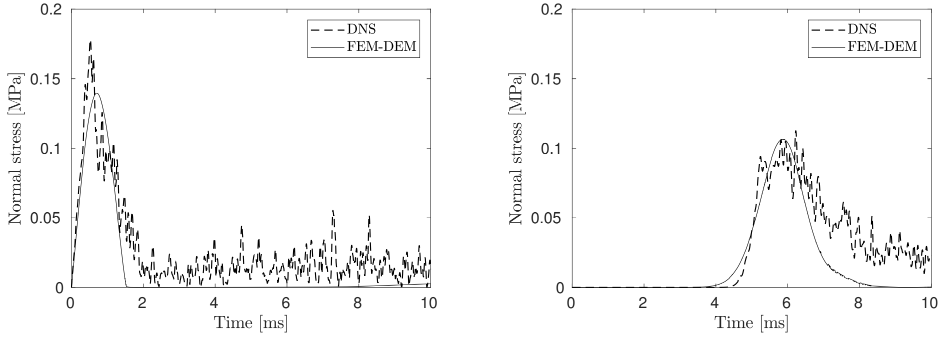

(a) (b)

**Figure 4.11:** Stress response normal to the top boundary of the FEM-DEM model ($n_e = 26$ elements) and the DNS model, evaluated at positions (a) $15$ mm, (b) $285$mm from the loading source. The underlying micro-structure is an *irregular packing* with *compressive-elastic* interactions.

model remains absent here, since the compressive-elastic interactions in the current particle structure are not able to transfer tensile forces.

## 4.5 Conclusions

In this Chapter, the multi-scale FEM-DEM framework for the analysis of granular materials has been extended to capture wave propagation phenomena. The method is based on a first-order computational homogenization approach, thereby using the hypotheses of scale separation and the long-wave approximation. The macro-scale problem is defined through a classical continuum, for which the standard equations of motion hold. This set of equations requires as input from the micro scale the first Piola-Kirchhoff stress tensor and the macroscopic effective density. In view of the hypotheses made, the former parameter is extracted from a quasi-static DEM analysis performed on the granular packing associated to each macroscopic material point. The effective density is simply derived by a rule of mixtures. The method has been tested on a numerical example, consisting of a macroscopic rectangular domain subjected to a compressive half-sine displacement pulse. The macro-scale problem is solved for different underlying granular microstructures, namely a one-dimensional string of particles, a regular mono-disperse packing and an irregular poly-disperse packing, which are characterized by bond-elastic or compressive-elastic particle interactions. The analysis of the results illustrates that the multi-scale solution agrees exactly to the DNS response for the one-dimensional string of particles. For the two-dimensional granular microstructures, the efficacy of the multi-scale method depends on the selected micro-structural contact law. For a bond-elastic particle interaction, the FEM-DEM solution agrees well with the DNS. Conversely, when considering compressive-elastic particle interactions, the multi-scale response shows significant differences with the DNS solution. These aspects point out a criticality of the method that currently remains unresolved and therefore requires further research.

# Chapter 5

# Conclusions and Recommendations

## 5.1 Conclusion

This thesis focuses on the first-order hierarchical multi-scale modeling of granular materials at large deformations. For this purpose, first a servo-control methodology is adopted to implement two types of classical boundary conditions for granular packings modelled with the discrete element method (DEM), namely, (1) periodic particle displacement and periodic particle rotation (P) and (2) uniform particle force and free particle rotation (T). The third classical boundary condition, which is homogeneous particle displacement and zero particle rotation (D), follows an implementation that, in contrast to the (P) and (T) boundary conditions, does not require an iterative scheme. The servo-control algorithm for the periodic boundary conditions is coupled with the finite element method to study effects of micro-scale parameters on the macro-scale response during quasi-static biaxial compression. The applicability and limitations of the presented multi-scale FEM-DEM method for solving wave propagation problem is demonstrated. The main conclusions drawn from numerical studies discussed in the individual chapters are summarized below.

### 5.1.1 Micro-scale boundary conditions

Novel algorithms for micro-scale boundary conditions of granular packings are implemented using an open-source DEM code ESyS-Particle, and are validated by studying the response of regular and irregular granular packings subjected to various loading paths.

For a regular, monodisperse packing subjected to a combined compression-true shear deformation mode, the (D) and (T) boundary conditions respectively provide stiff and soft responses that bound the response under (P) boundary conditions. The responses under the (D), (P) and (T) boundary conditions converge towards each other under increasing packing size. Furthermore, the response of an irregular polydisperse packing subjected to simple shear illustrates that the (P) boundary condition provides a faster convergence towards the apparent macroscopic properties than the (D) and (T) boundary conditions.

Additionally, mixed (D)-(P)-(T) boundary conditions have been proposed and have been proven to satisfy the Hill-Mandel micro-heterogeneity condition. The algorithm for these mixed boundary conditions is developed and tested for the case of an infinite layer subjected to a vertical compressive stress and a horizontal shear deformation, whereby the ultimate strength computed for a layer of cohesive particles appears to be about 1.5 times larger than that for a layer of frictional particles. The failure response for both contact laws is characterized by the dilatation of the particle assembly, which at large deformation gradually results in a critical state with an approximately constant residual strength and specific volume.

### 5.1.2 Multi-scale quasi-static simulations

The hierarchical multi-scale FEM-DEM method has been implemented by using the open-source DEM code ESyS-Particle and the open-source FEM code ESyS-Escript, and has been parallelized by using the module MPI in mpi4py.

First, a mesh convergence study has been performed, where the multi-scale FEM-DEM models have different meshes characterized by a number of elements: $n_e = [1 \times 1, 1 \times 2, 2 \times 4, 4 \times 8]$, and all Gauss point are initially connected to one and the same polydisperse granular microstructure composed of relatively soft particles. Upon mesh refinement the average stress-strain response of the coupled FEM-DEM models turns out to be in good agreement with that of the DNS model, especially in the pre-peak regime. After passing the maximum stress, the responses for the different meshes start to deviate from one other, due to the well-known reason that the strain-softening behavior is mesh dependent. The evolutions of the average macroscopic coordination number and the average anisotropy agree well with those reported in the literature. The spread in the stress values across the relatively coarse mesh is smaller than across the fine mesh, indicating that the fine mesh describes the heterogeneous response of the macroscopic domain with higher accuracy. For the finest mesh the overall deformation pattern at localized failure appears to be in good agreement with that of the DNS model.

A variation study of the particle contact friction shows that a larger value of the particle contact friction typically generates a higher stress, a larger volumetric compaction, and a smaller coordination number of the granular packing, which is consistent with results reported in the literature. In addition, constraining the particle rotation leads to a higher ultimate strength, a larger volumetric compaction, and a lower coordination number than for the case of unconstrained particle rotation. Finally, a higher initial fabric anisotropy creates a lower peak strength and less volumetric compaction.

### 5.1.3 Multi-scale dynamic simulations

By considering different granular microstructures and different contact laws between particles, the applicability and limitations of the multi-scale FEM-DEM method in solving wave propagation problems in the range of relatively long wavelengths are explored. It has been demonstrated that the multi-scale solution agrees exactly to the DNS response if the microstructure consists of a one-dimensional string of particles with bonded, elastic contacts. For two-dimensional regular and irregular polydisperse granular microstructures, the efficacy of the multi-scale method depends on the selected micro-structural contact law. For a bond-elastic particle interaction, the FEM-DEM solution agrees well with the DNS. However, when considering compressive-elastic particle interactions, the multi-scale response shows significant differences with the DNS solution. These aspects point out a criticality of the method that currently remains unresolved and therefore requires further research.

## 5.2 Recommendations

The numerical results for the quasi-static, multi-scale simulations presented in Chapter 3 have illustrated a mesh-dependent behavior during the strain softening (or shear banding) stage. This mesh-dependent behavior is common for first-order computational homogenization procedures. The mesh dependency results from the principle of local action assumed in the standard continuum theory and from the uniformity assumption on the macroscopic deformation across the attached micro-structural domain (Kouznetsova, 2002). These two assumptions can be relaxed by either using at the macro level a non-local continuum model, e.g., (Liu et al., 2016) or a higher-order continuum model, e.g., (Li et al., 2014), resulting in a mesh-independent behavior during strain softening upon mesh refinement. Despite this remedy, these two approaches are not sufficiently adequate to deal with strong localization, i.e., discrete cracking. The method presented in (Bosco et al., 2015a) employed the extended finite element method (XFEM) for the macroscopic domain and the percolation-path-aligned boundary conditions for the microscopic domain in order to simulate macroscopic crack propagation originating from damage at the micro scale. So, the computational scheme proposed in (Bosco et al., 2015a) may be adopted to simulate discrete cracking in cohesive granular materials by implementing a hierarchical multi-scale XFEM-DEM model where the XFEM is employed at the macro scale level and the percolation-path-aligned boundary conditions are used for the associated DEM model at the micro scale.

The application and limitations of the current FEM-DEM model to solve wave propagation problems have been demonstrated in Chapter 4. The FEM-DEM method developed in this thesis appeared to be highly accurate only for dynamic responses characterized by low-frequency waves propagating in granular materials with linear-elastic particle interactions. For dynamic responses characterized by relatively short waves that initiate wave dispersion phenomena, a more advanced, higher-order multi-scale model is required for obtaining a good correspondence with direct numerical simulations. As further demonstrated in Chapter 4, the accuracy level of the multi-scale method for wave propagation problems in granular systems composed of particles with non-linear contact interactions still contains unsatisfactory aspects, which need to be studied in more detail.

# Bibliography

Andrade, J. E., Avila, C. F., Hall, S. A., Lenoir, N., and Viggiani, G. (2011). Multiscale modeling and characterization of granular matter: From grain kinematics to continuum mechanics. *Journal of the Mechanics and Physics of Solids*, 59(2):237 – 250.

Bardet, J. P. (1994). Observations on the effects of particle rotations on the failure of idealized granular materials. *Mechanics of Materials*, 18:159–182.

Benson, D. J. (2007). Explicit finite element methods for large deformation problems in solid mechanics. In *Encyclopedia of Computational Mechanics*, pages 2–25. Wiley online library.

Bensoussan, A., Lions, J.-L., and Papanicolaou, G. (1978). *Asymptotic analysis for periodic structures*. Elsevier, North-Holland, Amsterdam.

Borja, R. I. and Wren, J. R. (1995). Micromechanics of granular media Part I: Generation of overall constitutive equation for assemblies of circular disks. *Computer Methods in Applied Mechanics and Engineering*, 127(1):13 – 36.

Bosco, E., Kouznetsova, V. G., Coenen, E. W. C., Geers, M. G. D., and Salvadori, A. (2014). A multiscale framework for localizing microstructures towards the onset of macroscopic discontinuity. *Computational Mechanics*, 54(2):299–319.

Bosco, E., Kouznetsova, V. G., and Geers, M. G. D. (2015a). Multi-scale computational homogenization–localization for propagating discontinuities using x-fem. *International Journal for Numerical Methods in Engineering*, 102(3-4):496–527.

Bosco, E., Kouznetsova, V. G., and Geers, M. G. D. (2015b). Multi-scale computational homogenization–localization for propagating discontinuities using X-FEM. *International Journal for Numerical Methods in Engineering*, 102(3-4):496–527.

Chang, C. S. and Gao, J. (1995). Non-linear dispersion of plane wave in granular media. *International journal of non-linear mechanics*, 30(2):111–128.

Chang, C. S. and Gao, J. (1997). Wave propagation in granular rod using high-gradient theory. *Journal of engineering mechanics*, 123(1):52–59.

Chang, C. S. and Liao, C. L. (1990). Constitutive relation for a particulate medium with the effect of particle rotation. *International Journal of Solids and Structures*, 26:437–453.

Chang, C. S. and Ma, L. (1992). Elastic material constants for isotropic granular solids with particle rotation. *International Journal of Solids and Structures*, 29:1001–1018.

Coenen, E. W. C., Kouznetsova, V. G., and Geers, M. G. D. (2012). Novel boundary conditions for strain localization analyses in microstructural volume elements. *International Journal for Numerical Methods in Engineering*, 90(1):1–21.

Cundall, P. A. and Strack, O. D. L. (1979). A discrete numerical model for granular assemblies. *Géotechnique*, 29(1):47–65.

de Borst, R. and Sluys, L. J. (2015). Computational methods in non-linear solid mechanics.

Desrues, J., Argilaga, A., Dal Pont, S., Combe, G., Caillerie, D., and kein Nguyen, T. (2017). Restoring mesh independency in fem-dem multi-scale modelling of strain localization using second gradient regularization. In *International Workshop on Bifurcation and Degradation in Geomaterials*, pages 453–457. Springer.

Dettmar, J. (2006). *Static and Dynamic Homogenization Analyses of Discrete Granular and Atomistic Structures on Different Time and Length Scales*. PhD thesis, University of Stuttgart.

Donev, A., Torquato, S., and Stillinger, F. H. (2005). Neighbor list collision-driven molecular dynamics simulation for nonspherical hard particles. i. algorithmic details. *Journal of Computational Physics*, 202(2):737–764.

Dussault, J. P. (1995). Numerical stability and efficiency of penalty algorithms. *SIAM Journal on Numerical Analysis*, 32:296–317.

Frangin, E., Marin, P., and Daudeville, L. (2006). On the use of combined finite/discrete element method for impacted concrete structures. In *Journal de Physique IV (Proceedings)*, volume 134, pages 461–466. EDP sciences.

Ghosh, S., Lee, K., and Moorthy, S. (1995). Multiple scale analysis of heterogeneous elastic structures using homogenization theory and voronoi cell finite element method. *International Journal of Solids and Structures*, 32(1):27–62.

Ghosh, S., Lee, K., and Moorthy, S. (1996). Two scale analysis of heterogeneous elastic-plastic materials with asymptotic homogenization and voronoi cell finite element model. *Computer methods in applied mechanics and engineering*, 132(1-2):63–116.

Göncü, F. and Luding, S. (2013). Effect of particle friction and polydispersity on the macroscopic stress-strain relations of granular materials. *Acta Geotechnica*, 8:629–643.

Guedes, J. M. and Kikuchi, N. (1990). Preprocessing and postprocessing for materials based on the homogenization method with adaptive finite element methods. *Computer methods in applied mechanics and engineering*, 83(2):143–198.

Gunaratne, A. and Wu, Z. (2011). A penalty function method for constrained molecular dynamics simulation. *International Journal of Numerical Analysis and Modeling*, 8:496–517.

Guo, N. and Zhao, J. (2013). The signature of shear-induced anisotropy in granular media. *Computers and Geotechnics*, 47:1–15.

Guo, N. and Zhao, J. (2014). A coupled FEM/DEM approach for hierarchical multiscale modelling of granular media. *International Journal for Numerical Methods in Engineering*, 99(11):789–818.

Guo, N. and Zhao, J. (2016a). 3D multiscale modeling of strain localization in granular media. *Computers and Geotechnics*, 80:360–372.

Guo, N. and Zhao, J. (2016b). Multiscale insights into classical geomechanics problems. *International Journal for Numerical and Analytical Methods in Geomechanics*, 40(3):367–390.

Guo, N., Zhao, J., and Sun, W. C. (2016). Multiscale analysis of shear failure of thick-walled hollow cylinder in dry sand. *Géotechnique Letters*, 6(1):1–6.

Hashin, Z. and Shtrikman, S. (1963). A variational approach to the theory of the elastic behaviour of multiphase materials. *Journal of the Mechanics and Physics of Solids*, 11(2):127–140.

Herrmann, H. J. and Luding, S. (1998). Modeling granular media on the computer. *Continuum Mechanics and Thermodynamics*, 10(4):189–231.

Hill, R. (1963). Elastic properties of reinforced solids: some theoretical principles. *Journal of the Mechanics and Physics of Solids*, 11(5):357–372.

Huang, X., O'Sullivan, C., Hanley, K., and Kwok, C. (2017). Partition of the contact force network obtained in discrete element simulations of element tests. *Computational Particle Mechanics*, 4(2):145–152.

Imole, O. I., Kumar, N., Magnanimo, V., and Luding, S. (2013). Hydrostatic and shear behavior of frictionless granular assemblies under different deformation conditions. *Kona*, 30:84 – 108.

Kaneko, K., Terada, K., Kyoya, T., and Kishino, Y. (2003). Global-local analysis of granular media in quasi-static equilibrium. *International Journal of Solids and Structures*, 40(15):4043 – 4069.

Kouznetsova, V. G. (2002). *Computational homogenization for the multi-scale analysis of multi-phase materials*. PhD thesis, Technische Universiteit Eindhoven.

Kouznetsova, V. G., Brekelmans, W. A. M., and Baaijens, F. P. T. (2001). An approach to micro-macro modeling of heterogeneous materials. *Computational Mechanics*, 27(1):37–48.

Kuhn, M. R. (1999). Structured deformation in granular materials. *Mechanics of Materials*, 31:407–429.

Kun, F. and Herrmann, H. J. (1996). A study of fragmentation processes using a discrete element method. *Computer Methods in Applied Mechanics and Engineering*, 138(1):3 – 18.

Lambe, T. W. and Whitman, R. V. (1969). *Soil Mechanics*. John Wiley & Sons, New York.

Li, X., Liang, Y., Duan, Q., Schrefler, B. A., and Du, Y. (2014). A mixed finite element procedure of gradient cosserat continuum for second-order computational homogenisation of granular materials. *Computational Mechanics*, 54(5):1331–1356.

Li, X., Liu, Q., and Zhang, J. (2010a). A micro–macro homogenization approach for discrete particle assembly–cosserat continuum modeling of granular materials. *International Journal of Solids and Structures*, 47(2):291–303.

Li, X. and Wan, K. (2011). A bridging scale method for granular materials with discrete particle assembly–cosserat continuum modeling. *Computers and Geotechnics*, 38(8):1052–1068.

Li, X., Wang, Z., Du, Y., and Duan, Q. (2016). Advances in multiscale fem-dem modeling of granular materials. In *International Conference on Discrete Element Methods*, pages 267–279. Springer.

Li, X., Zhang, J., and Zhang, X. (2011). Micro-macro homogenization of gradient-enhanced cosserat media. *European Journal of Mechanics-A/Solids*, 30(3):362–372.

Li, X., Zhang, X., and Zhang, J. (2010b). A generalized Hill's lemma and micromechanically based macroscopic constitutive model for heterogeneous granular materials. *Computer Methods in Applied Mechanics and Engineering*, 199(49-52):3137–3152.

Liu, J., Bosco, E., and Suiker, A. S. J. (2017). Formulation and numerical implementation of micro-scale boundary conditions for particle aggregates. *Granular Matter*, 19(4):72.

Liu, Y., Sun, W. C., Yuan, Z., and Fish, J. (2016). A nonlocal multiscale discrete-continuum model for predicting mechanical behavior of granular materials. *International Journal for Numerical Methods in Engineering*, 106(2):129–160.

Luding, S. (2004). Micro-macro transition for anisotropic, frictional granular packings. *International Journal of Solids and Structures*, 41:5821–5836.

Luding, S. and Suiker, A. S. J. (2008). Self-healing of damaged particulate materials through sintering. *Philosophical Magazine*, 88(28-29):3445–3457.

Åström, K. J. and Murray, R. (2008). *Feedback Systems: An Introduction for Scientists and Engineers*. Princeton University Press.

Meier, H., Steinmann, P., and Kuhl, E. (2009). On the multiscale modelling of confined granular media. In Eberhardsteiner, J., Hellmich, C., Mang, H. A., and Périaux, J., editors, *ECCOMAS Multidisciplinary Jubilee Symposium, New Computational Challenges in Materials, Structures and Fluids*. Springer, Dordrecht, Netherlands.

Meier, H. A., Steinmann, P., and Kuhl, E. (2008). Towards multiscale computation of confined granular media: contact forces, stresses and tangent operators. *Technische Mechanik*, 28(1):32–42.

Miehe, C. and Bayreuther, C. G. (2007). On multiscale FE analyses of heterogeneous structures: from homogenization to multigrid solvers. *International Journal for Numerical Methods in Engineering*, 71(10):1135–1180.

Miehe, C., Dettmar, J., and Zäh, D. (2010). Homogenization and two-scale simulations of granular materials for different microstructural constraints. *International Journal for Numerical Methods in Engineering*, 83(8-9):1206–1236.

Miehe, C. and Koch, A. (2002). Computational micro-to-macro transitions of discretized microstructures undergoing small strains. *Archive of Applied Mechanics*, 72(4-5):300–317.

Miehe, C., Schotte, J., and Lambrecht, M. (2002). Homogenization of inelastic solid materials at finite strains based on incremental minimization principles. Application to the texture analysis of polycrystals. *Journal of the Mechanics and Physics of Solids*, 50:2123–2167.

Miehe, C., Schotte, J., and Schröder, J. (1999a). Computational micro–macro transitions and overall moduli in the analysis of polycrystals at large strains. *Computational Materials Science*, 16(1-4):372–382.

Miehe, C., Schröder, J., and Schotte, J. (1999b). Computational homogenization analysis in finite plasticity simulation of texture development in polycrystalline materials. *Computer methods in applied mechanics and engineering*, 171(3-4):387–418.

Mouraille, O., Mulder, W. A., and Luding, S. (2006). Sound wave acceleration in granular materials. *Journal of Statistical Mechanics: Theory and Experiment*, 2006(07):P07023.

Mühlhaus, H. B. and Vardoulakis, I. (1987). The thickness of shear bands in granular materials. *Geotechnique*, 37(3):271–283.

Nguyen, T. K., Combe, G., Caillerie, D., and Desrues, J. (2013). Modeling of a cohesive granular materials by a multi-scale approach. *Powders and Grains*, 1542(1194-1197):106.

Nguyen, T. K., Combe, G., Caillerie, D., and Desrues, J. (2014). FEM×DEM modelling of cohesive granular materials: Numerical homogenisation and multi-scale simulations. *Acta Geophysica*, 62(5):1109–1126.

Nitka, M., Combe, G., Dascalu, C., and Desrues, J. (2011). Two-scale modeling of granular materials: a DEM-FEM approach. *Granular Matter*, 13(3):277–281.

Nitka, M. and Tejchman, J. (2015). Modelling of concrete behaviour in uniaxial compression and tension with dem. *Granular Matter*, 17(1):145–164.

O'Donovan, J., O'Sullivan, C., and Marketos, G. (2012a). Micromechanics of seismic wave propagation in granular materials. In *Discrete Element Modelling of Particulate Media*, pages 245–254.

O'Donovan, J., O'ullivan, C., and Marketos, G. (2012b). Two-dimensional discrete element modelling of bender element tests on an idealised granular material. *Granular Matter*, 14(6):733–747.

Potyondy, D. O. and Cundall, P. A. (2004). A bonded-particle model for rock. *International Journal of Rock Mechanics and Mining Sciences*, 41(8):1329–1364.

Rojek, J. and Oñate, E. (2007). Multiscale analysis using a coupled discrete/finite element model. *Interaction and Multiscale Mechanics*, 1(1):1–31.

Rothenburg, L., Bathurst, R., and Matyas, E. (1989). Mechanisms of fabric evolution in granular media. In *Proc. 12th International Conference on Soil Mechanics and Foundation Engineering, Rio de Janeiro, Brazil*, pages 753–756. A.A. Balkema, Rotterdam.

Sadd, M. H., Adhikari, G., and Cardoso, F. (2000). Dem simulation of wave propagation in granular materials. *Powder Technology*, 109(1-3):222–233.

Sanchez-Palencia, E. (1980). Non-homogeneous media and vibration theory, lecture notes in physics. 127.

Schaa, R., Gross, L., and Du Plessis, J. (2016). PDE-based geophysical modelling using finite elements: examples from 3D resistivity and 2D magnetotellurics. *Journal of Geophysics and Engineering*, 13:S59–S73.

Shahin, G., Desrues, J., Dal Pont, S., Combe, G., and Argilaga, A. (2016). A study of the influence of REV variability in double scale FEM×DEM analysis. *International Journal for Numerical Methods in Engineering*, 107(10):882–900.

Singh, A., Magnanimo, V., Saitoh, K., and Luding, S. (2014). Effect of cohesion on shear banding in quasi-static granular materials. *Physical Review E*, 90(2):022202.

Somfai, E., Roux, J.-N., Snoeijer, J. H., van Hecke, M., and van Saarloos, W. (2005). Elastic wave propagation in confined granular systems. *Physical Review E*, 72(2):021301.

Suiker, A. S. J. and de Borst, R. (2005). Enhanced continua and discrete lattices for modelling granular assemblies. *Philosophical Transactions of the Royal Society series A.*, 363:2543–2580.

Suiker, A. S. J., de Borst, R., and Chang, C. S. (2001a). Micro-mechanical modelling of granular material. Part 1: Derivation of a second-gradient micro-polar constitutive theory. *Acta Mechanica*, 149:161–180.

Suiker, A. S. J., de Borst, R., and Chang, C. S. (2001b). Micro-mechanical modelling of granular material. Part 2: Plane wave propagation propagation in infinite media. *Acta Mechanica*, 149:181–200.

Suiker, A. S. J. and Fleck, N. A. (2004). Frictional collapse of granular assemblies. *Journal of Applied Mechanics*, 71(3):350–358.

Suquet, P. M. (1985). Local and global aspects in the mathematical theory of plasticity. In Sawczuk, A. and Bianchi, G., editors, *Plasticity Today: Modelling, Methods and Applications*, pages 279–310. Elsevier Applied Science Publishers, London.

Terada, K., Hori, M., Kyoya, T., and Kikuchi, N. (2000). Simulation of the multiscale convergence in computational homogenization approaches. *International Journal of Solids and Structures*, 37(16):2285 – 2311.

Ting, J. M., Khwaja, M., Meachum, L. R., and Rowell, J. D. (1993). An ellipse-based discrete element model for granular materials. *International Journal for Numerical and Analytical Methods in Geomechanics*, 17(9):603–623.

Torquato, S. (2002). *Random Heterogeneous Materials*. Springer-Verlag, New York.

Underwood, P. (1983). Dyamic relaxation. In Belytschko, T. and Hughes, T. J. R., editors, *Computational Methods for Transient Analysis*, pages 245–265. North-Holland, Amsterdam.

Virgo, S., Abe, S., and Urai, J. L. (2013). Extension fracture propagation in rocks with veins: Insight into the crack-seal process using discrete element method modeling. *Journal of Geophysical Research: Solid Earth*, 118(10):5236–5251.

Wagner, G. J. and Liu, W. K. (2003). Coupling of atomistic and continuum simulations using a bridging scale decomposition. *Journal of Computational Physics*, 190(1):249–274.

Wang, Y. (2009). A new algorithm to model the dynamics of 3-D bonded rigid bodies with rotations. *Acta Geotechnica*, 4(2):117–127.

Wang, Y. and Mora, P. (2008). Modeling wing crack extension: implications for the ingredients of discrete element model. *Pure and Applied Geophysics*, 165(3-4):609–620.

Weatherley, D., Hancock, W., Boros, V., and Abe, S. (2014). ESyS-particle tutorial and user's guide version 2.3.1.

Wellmann, C., Lillie, C., and Wriggers, P. (2008). Homogenization of granular material modeled by a three-dimensional discrete element method. *Computers and Geotechnics*, 35(3):394 – 405.

Wellmann, C. and Wriggers, P. (2012). A two-scale model of granular materials. *Computer Methods in Applied Mechanics and Engineering*, 205:46–58.

Willis, J. R. (1981). Variational and related methods for the overall properties of composites. In *Advances in applied mechanics*, volume 21, pages 1–78. Elsevier.

Wu, H., Guo, N., and Zhao, J. (2018a). Multiscale modeling and analysis of compaction bands in high-porosity sandstones. *Acta Geotechnica*, 13(3):575–599.

Wu, H., Zhao, J., and Guo, N. (2018b). Multiscale insights into borehole instabilities in high-porosity sandstones. *Journal of Geophysical Research: Solid Earth*, 123(5):3450–3473.

Xiao, S. P. and Belytschko, T. (2004). A bridging domain method for coupling continua with molecular dynamics. *Computer methods in applied mechanics and engineering*, 193(17-20):1645–1669.

Zhang, L. G. and Yu, T. X. (1989). Modified adaptive dynamic relaxation method and its application to elastic-plastic bending and wrinkling of circular plates. *Computers & Structures*, 33(2):609–614.

Zhang, Q. and Zhao, J. (2014). A review of dynamic experimental techniques and mechanical behaviour of rock materials. *Rock mechanics and rock engineering*, 47(4):1411–1478.

Zhao, J. (2017). Hierarchical multiscale modeling of strain localization in granular materials: A condensed overview and perspectives. In *International Workshop on Bifurcation and Degradation in Geomaterials*, pages 349–359. Springer.

Zhao, J. and Guo, N. (2015). The interplay between anisotropy and strain localisation in granular soils: a multiscale insight. *Géotechnique*, 65(8):642–656.

Zhao, S., Evans, T., and Zhou, X. (2018). Shear-induced anisotropy of granular materials with rolling resistance and particle shape effects. *International Journal of Solids and Structures*, 150:268–281.

Zhu, H., Nicot, F., and Darve, F. (2016). Meso-structure evolution in a 2d granular material during biaxial loading. *Granular Matter*, 18(1):3.

Zienkiewicz, O. C. and Taylor, R. L. (1991). *The Finite Element Method - Volume 2, Solid and Fluid Mechanics, Dynamics and Non-linearity*. McGraw-Hill Book Campany Europe, 4th edition.

# Curriculum Vitae

Jiadun Liu was born on 22nd April, 1987 in Shandong, China. In July 2009, he obtained his Bachelor degree in Mining Engineering in Hunan University of Science and Technology, China. From September 2009, he continued his master's study in Mining Engineering in China University of Mining and Technology, Beijing, under the supervision of prof. Jiachen Wang and dr. Weidong Pan. In July 2012, he obtained his Master degree in Mining Engineering. After one-year PhD study in the group of prof. Hongwei Zhou in China University of Mining and Technology, Beijing, in September 2013, funded by the Chinese Scholarship Council, he came to the Netherlands to study 'Multi-scale FEM-DEM model for granular materials' under the supervision of prof.dr.ir. A.S.J. Suiker and dr.ir. E. Bosco. The research results are presented in this thesis.

# Publication list

## Journal Publications

1. Liu, J., Bosco, E. and Suiker, A.S.J. , Formulation and numerical implementation of micro-scale boundary conditions for particle aggregates. Granular Matter, 19(4), 72, 2017.
2. Liu, J., Bosco, E. and Suiker, A.S.J. , Multi-scale modelling of granular materials: numerical framework and study on micro-structural features. Computational Mechanics, 2018. https://doi.org/10.1007/s00466-018-1600-y.

## Posters

1. Liu, J. and Suiker, A.S.J. , Multi-scale Modelling of Granular Materials. Seventeenth Engineering Mechanics Symposium, Arnhem, the Netherlands, October 28 - October 29, 2014.
2. Liu, J. and Suiker, A.S.J. , Multi-scale Modelling of Granular Materials: Micro-scale Boundary Conditions. Eighteenth Engineering Mechanics Symposium, Arnhem, the Netherlands, October 27 - October 28, 2015.
3. Liu, J., Suiker, A.S.J. and Bosco, E. , A FEM-DEM Model for Granular Materials. Nineteenth Engineering Mechanics Symposium, Arnhem, the Netherlands, October 25 - October 26, 2016.
4. Liu, J., Bosco, E. and Suiker, A.S.J. , A FEM-DEM Model for Granular Materials. Twentieth Engineering Mechanics Symposium, Arnhem, the Netherlands, October 23 - October 25, 2017.

**Bouwstenen** is een publicatiereeks
van de Faculteit Bouwkunde,
Technische Universiteit Eindhoven.
Zij presenteert resultaten van
onderzoek en andere activiteiten op
het vakgebied der Bouwkunde,
uitgevoerd in het kader van deze
Faculteit.

**Bouwstenen** en andere proefschriften van de
TU/e zijn online beschikbaar via:
https://research.tue.nl/

Kernredactie
MTOZ

Reeds verschenen in de serie
**Bouwstenen**

nr 1
**Elan: A Computer Model for Building Energy Design: Theory and Validation**
Martin H. de Wit
H.H. Driessen
R.M.M. van der Velden

nr 2
**Kwaliteit, Keuzevrijheid en Kosten: Evaluatie van Experiment Klarendal, Arnhem**
J. Smeets
C. le Nobel
M. Broos
J. Frenken
A. v.d. Sanden

nr 3
**Crooswijk:**
**Van 'Bijzonder' naar 'Gewoon'**
Vincent Smit
Kees Noort

nr 4
**Staal in de Woningbouw**
Edwin J.F. Delsing

nr 5
**Mathematical Theory of Stressed Skin Action in Profiled Sheeting with Various Edge Conditions**
Andre W.A.M.J. van den Bogaard

nr 6
**Hoe Berekenbaar en Betrouwbaar is de Coëfficiënt k in x-ksigma en x-ks?**
K.B. Lub
A.J. Bosch

nr 7
**Het Typologisch Gereedschap:**
**Een Verkennende Studie Omtrent Typologie en Omtrent de Aanpak van Typologisch Onderzoek**
J.H. Luiten

nr 8
**Informatievoorziening en Beheerprocessen**
A. Nauta
Jos Smeets (red.)
Helga Fassbinder (projectleider)
Adrie Proveniers
J. v.d. Moosdijk

nr 9
**Strukturering en Verwerking van Tijdgegevens voor de Uitvoering van Bouwwerken**
ir. W.F. Schaefer
P.A. Erkelens

nr 10
**Stedebouw en de Vorming van een Speciale Wetenschap**
K. Doevendans

nr 11
**Informatica en Ondersteuning van Ruimtelijke Besluitvorming**
G.G. van der Meulen

nr 12
**Staal in de Woningbouw, Korrosie-Bescherming van de Begane Grondvloer**
Edwin J.F. Delsing

nr 13
**Een Thermisch Model voor de Berekening van Staalplaatbetonvloeren onder Brandomstandigheden**
A.F. Hamerlinck

nr 14
**De Wijkgedachte in Nederland: Gemeenschapsstreven in een Stedebouwkundige Context**
K. Doevendans
R. Stolzenburg

nr 15
**Diaphragm Effect of Trapezoidally Profiled Steel Sheets:**
**Experimental Research into the Influence of Force Application**
Andre W.A.M.J. van den Bogaard

nr 16
**Versterken met Spuit-Ferrocement:**
**Het Mechanische Gedrag van met Spuit-Ferrocement Versterkte Gewapend Betonbalken**
K.B. Lubir
M.C.G. van Wanroy

nr 17
**De Tractaten van
Jean Nicolas Louis Durand**
G. van Zeyl

nr 18
**Wonen onder een Plat Dak:
Drie Opstellen over Enkele
Vooronderstellingen van de
Stedebouw**
K. Doevendans

nr 19
**Supporting Decision Making Processes:
A Graphical and Interactive Analysis of
Multivariate Data**
W. Adams

nr 20
**Self-Help Building Productivity:
A Method for Improving House Building
by Low-Income Groups Applied to Kenya
1990-2000**
P. A. Erkelens

nr 21
**De Verdeling van Woningen:
Een Kwestie van Onderhandelen**
Vincent Smit

nr 22
**Flexibiliteit en Kosten in het Ontwerpproces:
Een Besluitvormingondersteunend Model**
M. Prins

nr 23
**Spontane Nederzettingen Begeleid:
Voorwaarden en Criteria in Sri Lanka**
Po Hin Thung

nr 24
**Fundamentals of the Design of
Bamboo Structures**
Oscar Arce-Villalobos

nr 25
**Concepten van de Bouwkunde**
M.F.Th. Bax (red.)
H.M.G.J. Trum (red.)

nr 26
**Meaning of the Site**
Xiaodong Li

nr 27
**Het Woonmilieu op Begrip Gebracht:
Een Speurtocht naar de Betekenis van het
Begrip 'Woonmilieu'**
Jaap Ketelaar

nr 28
**Urban Environment in Developing Countries**
editors: Peter A. Erkelens
George G. van der Meulen (red.)

nr 29
**Stategische Plannen voor de Stad:
Onderzoek en Planning in Drie Steden**
prof.dr. H. Fassbinder (red.)
H. Rikhof (red.)

nr 30
**Stedebouwkunde en Stadsbestuur**
Piet Beekman

nr 31
**De Architectuur van Djenné:
Een Onderzoek naar de Historische Stad**
P.C.M. Maas

nr 32
**Conjoint Experiments and Retail Planning**
Harmen Oppewal

nr 33
**Strukturformen Indonesischer Bautechnik:
Entwicklung Methodischer Grundlagen
für eine 'Konstruktive Pattern Language'
in Indonesien**
Heinz Frick arch. SIA

nr 34
**Styles of Architectural Designing:
Empirical Research on Working Styles
and Personality Dispositions**
Anton P.M. van Bakel

nr 35
**Conjoint Choice Models for Urban
Tourism Planning and Marketing**
Benedict Dellaert

nr 36
**Stedelijke Planvorming als Co-Produktie**
Helga Fassbinder (red.)

nr 37
**Design Research in the Netherlands**
editors: R.M. Oxman
M.F.Th. Bax
H.H. Achten

nr 38
**Communication in the Building Industry**
Bauke de Vries

nr 39
**Optimaal Dimensioneren van Gelaste Plaatliggers**
J.B.W. Stark
F. van Pelt
L.F.M. van Gorp
B.W.E.M. van Hove

nr 40
**Huisvesting en Overwinning van Armoede**
P.H. Thung
P. Beekman (red.)

nr 41
**Urban Habitat:**
**The Environment of Tomorrow**
George G. van der Meulen
Peter A. Erkelens

nr 42
**A Typology of Joints**
John C.M. Olie

nr 43
**Modeling Constraints-Based Choices for Leisure Mobility Planning**
Marcus P. Stemerding

nr 44
**Activity-Based Travel Demand Modeling**
Dick Ettema

nr 45
**Wind-Induced Pressure Fluctuations on Building Facades**
Chris Geurts

nr 46
**Generic Representations**
Henri Achten

nr 47
**Johann Santini Aichel:**
**Architectuur en Ambiguiteit**
Dirk De Meyer

nr 48
**Concrete Behaviour in Multiaxial Compression**
Erik van Geel

nr 49
**Modelling Site Selection**
Frank Witlox

nr 50
**Ecolemma Model**
Ferdinand Beetstra

nr 51
**Conjoint Approaches to Developing Activity-Based Models**
Donggen Wang

nr 52
**On the Effectiveness of Ventilation**
Ad Roos

nr 53
**Conjoint Modeling Approaches for Residential Group preferences**
Eric Molin

nr 54
**Modelling Architectural Design Information by Features**
Jos van Leeuwen

nr 55
**A Spatial Decision Support System for the Planning of Retail and Service Facilities**
Theo Arentze

nr 56
**Integrated Lighting System Assistant**
Ellie de Groot

nr 57
**Ontwerpend Leren, Leren Ontwerpen**
J.T. Boekholt

nr 58
**Temporal Aspects of Theme Park Choice Behavior**
Astrid Kemperman

nr 59
**Ontwerp van een Geïndustrialiseerde Funderingswijze**
Faas Moonen

nr 60
**Merlin: A Decision Support System for Outdoor Leisure Planning**
Manon van Middelkoop

nr 61
**The Aura of Modernity**
Jos Bosman

nr 62
**Urban Form and Activity-Travel Patterns**
Daniëlle Snellen

nr 63
**Design Research in the Netherlands 2000**
Henri Achten

nr 64
**Computer Aided Dimensional Control in Building Construction**
Rui Wu

nr 65
**Beyond Sustainable Building**
editors: Peter A. Erkelens
Sander de Jonge
August A.M. van Vliet
co-editor: Ruth J.G. Verhagen

nr 66
**Das Globalrecyclingfähige Haus**
Hans Löfflad

nr 67
**Cool Schools for Hot Suburbs**
René J. Dierkx

nr 68
**A Bamboo Building Design Decision Support Tool**
Fitri Mardjono

nr 69
**Driving Rain on Building Envelopes**
Fabien van Mook

nr 70
**Heating Monumental Churches**
Henk Schellen

nr 71
**Van Woningverhuurder naar Aanbieder van Woongenot**
Patrick Dogge

nr 72
**Moisture Transfer Properties of Coated Gypsum**
Emile Goossens

nr 73
**Plybamboo Wall-Panels for Housing**
Guillermo E. González-Beltrán

nr 74
**The Future Site-Proceedings**
Ger Maas
Frans van Gassel

nr 75
**Radon transport in Autoclaved Aerated Concrete**
Michel van der Pal

nr 76
**The Reliability and Validity of Interactive Virtual Reality Computer Experiments**
Amy Tan

nr 77
**Measuring Housing Preferences Using Virtual Reality and Belief Networks**
Maciej A. Orzechowski

nr 78
**Computational Representations of Words and Associations in Architectural Design**
Nicole Segers

nr 79
**Measuring and Predicting Adaptation in Multidimensional Activity-Travel Patterns**
Chang-Hyeon Joh

nr 80
**Strategic Briefing**
Fayez Al Hassan

nr 81
**Well Being in Hospitals**
Simona Di Cicco

nr 82
**Solares Bauen: Implementierungs- und Umsetzungs-Aspekte in der Hochschulausbildung in Österreich**
Gerhard Schuster

nr 83
**Supporting Strategic Design of Workplace Environments with Case-Based Reasoning**
Shauna Mallory-Hill

nr 84
**ACCEL: A Tool for Supporting Concept Generation in the Early Design Phase**
Maxim Ivashkov

nr 85
**Brick-Mortar Interaction in Masonry under Compression**
Ad Vermeltfoort

nr 86
**Zelfredzaam Wonen**
Guus van Vliet

nr 87
**Een Ensemble met Grootstedelijke Allure**
Jos Bosman
Hans Schippers

nr 88
**On the Computation of Well-Structured Graphic Representations in Architectural Design**
Henri Achten

nr 89
**De Evolutie van een West-Afrikaanse Vernaculaire Architectuur**
Wolf Schijns

nr 90
**ROMBO Tactiek**
Christoph Maria Ravesloot

nr 91
**External Coupling between Building Energy Simulation and Computational Fluid Dynamics**
Ery Djunaedy

nr 92
**Design Research in the Netherlands 2005**
editors: Henri Achten
Kees Dorst
Pieter Jan Stappers
Bauke de Vries

nr 93
**Ein Modell zur Baulichen Transformation**
Jalil H. Saber Zaimian

nr 94
**Human Lighting Demands: Healthy Lighting in an Office Environment**
Myriam Aries

nr 95
**A Spatial Decision Support System for the Provision and Monitoring of Urban Greenspace**
Claudia Pelizaro

nr 96
**Leren Creëren**
Adri Proveniers

nr 97
**Simlandscape**
Rob de Waard

nr 98
**Design Team Communication**
Ad den Otter

nr 99
**Humaan-Ecologisch Georiënteerde Woningbouw**
Juri Czabanowski

nr 100
**Hambase**
Martin de Wit

nr 101
**Sound Transmission through Pipe Systems and into Building Structures**
Susanne Bron-van der Jagt

nr 102
**Het Bouwkundig Contrapunt**
Jan Francis Boelen

nr 103
**A Framework for a Multi-Agent Planning Support System**
Dick Saarloos

nr 104
**Bracing Steel Frames with Calcium Silicate Element Walls**
Bright Mweene Ng'andu

nr 105
**Naar een Nieuwe Houtskeletbouw**
F.N.G. De Medts

nr 106 and 107
*Niet gepubliceerd*

nr 108
**Geborgenheid**
T.E.L. van Pinxteren

nr 109
**Modelling Strategic Behaviour in Anticipation of Congestion**
Qi Han

nr 110
**Reflecties op het Woondomein**
Fred Sanders

nr 111
**On Assessment of Wind Comfort by Sand Erosion**
Gábor Dezsö

nr 112
**Bench Heating in Monumental Churches**
Dionne Limpens-Neilen

nr 113
**RE. Architecture**
Ana Pereira Roders

nr 114
**Toward Applicable Green Architecture**
Usama El Fiky

nr 115
**Knowledge Representation under Inherent Uncertainty in a Multi-Agent System for Land Use Planning**
Liying Ma

nr 116
**Integrated Heat Air and Moisture Modeling and Simulation**
Jos van Schijndel

nr 117
**Concrete Behaviour in Multiaxial Compression**
J.P.W. Bongers

nr 118
**The Image of the Urban Landscape**
Ana Moya Pellitero

nr 119
**The Self-Organizing City in Vietnam**
Stephanie Geertman

nr 120
**A Multi-Agent Planning Support System for Assessing Externalities of Urban Form Scenarios**
Rachel Katoshevski-Cavari

nr 121
**Den Schulbau Neu Denken, Fühlen und Wollen**
Urs Christian Maurer-Dietrich

nr 122
**Peter Eisenman Theories and Practices**
Bernhard Kormoss

nr 123
**User Simulation of Space Utilisation**
Vincent Tabak

nr 125
**In Search of a Complex System Model**
Oswald Devisch

nr 126
**Lighting at Work:**
**Environmental Study of Direct Effects of Lighting Level and Spectrum on Psycho-Physiological Variables**
Grazyna Górnicka

nr 127
**Flanking Sound Transmission through Lightweight Framed Double Leaf Walls**
Stefan Schoenwald

nr 128
**Bounded Rationality and Spatio-Temporal Pedestrian Shopping Behavior**
Wei Zhu

nr 129
**Travel Information:**
**Impact on Activity Travel Pattern**
Zhongwei Sun

nr 130
**Co-Simulation for Performance Prediction of Innovative Integrated Mechanical Energy Systems in Buildings**
Marija Trčka

nr 131
*Niet gepubliceerd*

nr 132
**Architectural Cue Model in Evacuation Simulation for Underground Space Design**
Chengyu Sun

nr 133
**Uncertainty and Sensitivity Analysis in Building Performance Simulation for Decision Support and Design Optimization**
Christina Hopfe

nr 134
**Facilitating Distributed Collaboration in the AEC/FM Sector Using Semantic Web Technologies**
Jacob Beetz

nr 135
**Circumferentially Adhesive Bonded Glass Panes for Bracing Steel Frame in Façades**
Edwin Huveners

nr 136
**Influence of Temperature on Concrete Beams Strengthened in Flexure with CFRP**
Ernst-Lucas Klamer

nr 137
**Sturen op Klantwaarde**
Jos Smeets

nr 139
**Lateral Behavior of Steel Frames with Discretely Connected Precast Concrete Infill Panels**
Paul Teewen

nr 140
**Integral Design Method in the Context of Sustainable Building Design**
Perica Savanović

nr 141
**Household Activity-Travel Behavior: Implementation of Within-Household Interactions**
Renni Anggraini

nr 142
**Design Research in the Netherlands 2010**
Henri Achten

nr 143
**Modelling Life Trajectories and Transport Mode Choice Using Bayesian Belief Networks**
Marloes Verhoeven

nr 144
**Assessing Construction Project Performance in Ghana**
William Gyadu-Asiedu

nr 145
**Empowering Seniors through Domotic Homes**
Masi Mohammadi

nr 146
**An Integral Design Concept for Ecological Self-Compacting Concrete**
Martin Hunger

nr 147
**Governing Multi-Actor Decision Processes in Dutch Industrial Area Redevelopment**
Erik Blokhuis

nr 148
**A Multifunctional Design Approach for Sustainable Concrete**
Götz Hüsken

nr 149
**Quality Monitoring in Infrastructural Design-Build Projects**
Ruben Favié

nr 150
**Assessment Matrix for Conservation of Valuable Timber Structures**
Michael Abels

nr 151
**Co-simulation of Building Energy Simulation and Computational Fluid Dynamics for Whole-Building Heat, Air and Moisture Engineering**
Mohammad Mirsadeghi

nr 152
**External Coupling of Building Energy Simulation and Building Element Heat, Air and Moisture Simulation**
Daniel Cóstola

nr 153
**Adaptive Decision Making In Multi-Stakeholder Retail Planning**
Ingrid Janssen

nr 154
**Landscape Generator**
Kymo Slager

nr 155
**Constraint Specification in Architecture**
Remco Niemeijer

nr 156
**A Need-Based Approach to Dynamic Activity Generation**
Linda Nijland

nr 157
**Modeling Office Firm Dynamics in an Agent-Based Micro Simulation Framework**
Gustavo Garcia Manzato

nr 158
**Lightweight Floor System for Vibration Comfort**
Sander Zegers

nr 159
**Aanpasbaarheid van de Draagstructuur**
Roel Gijsbers

nr 160
**'Village in the City' in Guangzhou, China**
Yanliu Lin

nr 161
**Climate Risk Assessment in Museums**
Marco Martens

nr 162
**Social Activity-Travel Patterns**
Pauline van den Berg

nr 163
**Sound Concentration Caused by Curved Surfaces**
Martijn Vercammen

nr 164
**Design of Environmentally Friendly Calcium Sulfate-Based Building Materials: Towards an Improved Indoor Air Quality**
Qingliang Yu

nr 165
**Beyond Uniform Thermal Comfort on the Effects of Non-Uniformity and Individual Physiology**
Lisje Schellen

nr 166
**Sustainable Residential Districts**
Gaby Abdalla

nr 167
**Towards a Performance Assessment Methodology using Computational Simulation for Air Distribution System Designs in Operating Rooms**
Mônica do Amaral Melhado

nr 168
**Strategic Decision Modeling in Brownfield Redevelopment**
Brano Glumac

nr 169
**Pamela: A Parking Analysis Model for Predicting Effects in Local Areas**
Peter van der Waerden

nr 170
**A Vision Driven Wayfinding Simulation-System Based on the Architectural Features Perceived in the Office Environment**
Qunli Chen

nr 171
**Measuring Mental Representations Underlying Activity-Travel Choices**
Oliver Horeni

nr 172
**Modelling the Effects of Social Networks on Activity and Travel Behaviour**
Nicole Ronald

nr 173
**Uncertainty Propagation and Sensitivity Analysis Techniques in Building Performance Simulation to Support Conceptual Building and System Design**
Christian Struck

nr 174
**Numerical Modeling of Micro-Scale Wind-Induced Pollutant Dispersion in the Built Environment**
Pierre Gousseau

nr 175
**Modeling Recreation Choices**
**over the Family Lifecycle**
Anna Beatriz Grigolon

nr 176
**Experimental and Numerical Analysis of**
**Mixing Ventilation at Laminar, Transitional**
**and Turbulent Slot Reynolds Numbers**
Twan van Hooff

nr 177
**Collaborative Design Support:**
**Workshops to Stimulate Interaction and**
**Knowledge Exchange Between Practitioners**
Emile M.C.J. Quanjel

nr 178
**Future-Proof Platforms for Aging-in-Place**
Michiel Brink

nr 179
**Motivate:**
**A Context-Aware Mobile Application for**
**Physical Activity Promotion**
Yuzhong Lin

nr 180
**Experience the City:**
**Analysis of Space-Time Behaviour and**
**Spatial Learning**
Anastasia Moiseeva

nr 181
**Unbonded Post-Tensioned Shear Walls of**
**Calcium Silicate Element Masonry**
Lex van der Meer

nr 182
**Construction and Demolition Waste**
**Recycling into Innovative Building Materials**
**for Sustainable Construction in Tanzania**
Mwita M. Sabai

nr 183
**Durability of Concrete**
**with Emphasis on Chloride Migration**
Przemysław Spiesz

nr 184
**Computational Modeling of Urban**
**Wind Flow and Natural Ventilation Potential**
**of Buildings**
Rubina Ramponi

nr 185
**A Distributed Dynamic Simulation**
**Mechanism for Buildings Automation**
**and Control Systems**
Azzedine Yahiaoui

nr 186
**Modeling Cognitive Learning of Urban**
**Networks in Daily Activity-Travel Behavior**
Şehnaz Cenani Durmazoğlu

nr 187
**Functionality and Adaptability of Design**
**Solutions for Public Apartment Buildings**
**in Ghana**
Stephen Agyefi-Mensah

nr 188
**A Construction Waste Generation Model**
**for Developing Countries**
Lilliana Abarca-Guerrero

nr 189
**Synchronizing Networks:**
**The Modeling of Supernetworks for**
**Activity-Travel Behavior**
Feixiong Liao

nr 190
**Time and Money Allocation Decisions**
**in Out-of-Home Leisure Activity Choices**
Gamze Zeynep Dane

nr 191
**How to Measure Added Value of CRE and**
**Building Design**
Rianne Appel-Meulenbroek

nr 192
**Secondary Materials in Cement-Based**
**Products:**
**Treatment, Modeling and Environmental**
**Interaction**
Miruna Florea

nr 193
**Concepts for the Robustness Improvement**
**of Self-Compacting Concrete:**
**Effects of Admixtures and Mixture**
**Components on the Rheology and Early**
**Hydration at Varying Temperatures**
Wolfram Schmidt

nr 194
**Modelling and Simulation of Virtual Natural Lighting Solutions in Buildings**
Rizki A. Mangkuto

nr 195
**Nano-Silica Production at Low Temperatures from the Dissolution of Olivine - Synthesis, Tailoring and Modelling**
Alberto Lazaro Garcia

nr 196
**Building Energy Simulation Based Assessment of Industrial Halls for Design Support**
Bruno Lee

nr 197
**Computational Performance Prediction of the Potential of Hybrid Adaptable Thermal Storage Concepts for Lightweight Low-Energy Houses**
Pieter-Jan Hoes

nr 198
**Application of Nano-Silica in Concrete**
George Quercia Bianchi

nr 199
**Dynamics of Social Networks and Activity Travel Behaviour**
Fariya Sharmeen

nr 200
**Building Structural Design Generation and Optimisation including Spatial Modification**
Juan Manuel Davila Delgado

nr 201
**Hydration and Thermal Decomposition of Cement/Calcium-Sulphate Based Materials**
Ariën de Korte

nr 202
**Republiek van Beelden:**
**De Politieke Werkingen van het Ontwerp in Regionale Planvorming**
Bart de Zwart

nr 203
**Effects of Energy Price Increases on Individual Activity-Travel Repertoires and Energy Consumption**
Dujuan Yang

nr 204
**Geometry and Ventilation:**
**Evaluation of the Leeward Sawtooth Roof Potential in the Natural Ventilation of Buildings**
Jorge Isaac Perén Montero

nr 205
**Computational Modelling of Evaporative Cooling as a Climate Change Adaptation Measure at the Spatial Scale of Buildings and Streets**
Hamid Montazeri

nr 206
**Local Buckling of Aluminium Beams in Fire Conditions**
Ronald van der Meulen

nr 207
**Historic Urban Landscapes:**
**Framing the Integration of Urban and Heritage Planning in Multilevel Governance**
Loes Veldpaus

nr 208
**Sustainable Transformation of the Cities:**
**Urban Design Pragmatics to Achieve a Sustainable City**
Ernesto Antonio Zumelzu Scheel

nr 209
**Development of Sustainable Protective Ultra-High Performance Fibre Reinforced Concrete (UHPFRC):**
**Design, Assessment and Modeling**
Rui Yu

nr 210
**Uncertainty in Modeling Activity-Travel Demand in Complex Uban Systems**
Soora Rasouli

nr 211
**Simulation-based Performance Assessment of Climate Adaptive Greenhouse Shells**
Chul-sung Lee

nr 212
**Green Cities:**
**Modelling the Spatial Transformation of the Urban Environment using Renewable Energy Technologies**
Saleh Mohammadi

nr 213
**A Bounded Rationality Model of Short and Long-Term Dynamics of Activity-Travel Behavior**
Ifigeneia Psarra

nr 214
**Effects of Pricing Strategies on Dynamic Repertoires of Activity-Travel Behaviour**
Elaheh Khademi

nr 215
**Handstorm Principles for Creative and Collaborative Working**
Frans van Gassel

nr 216
**Light Conditions in Nursing Homes: Visual Comfort and Visual Functioning of Residents**
Marianne M. Sinoo

nr 217
**Woonsporen: De Sociale en Ruimtelijke Biografie van een Stedelijk Bouwblok in de Amsterdamse Transvaalbuurt**
Hüseyin Hüsnü Yegenoglu

nr 218
**Studies on User Control in Ambient Intelligent Systems**
Berent Willem Meerbeek

nr 219
**Daily Livings in a Smart Home: Users' Living Preference Modeling of Smart Homes**
Erfaneh Allameh

nr 220
**Smart Home Design: Spatial Preference Modeling of Smart Homes**
Mohammadali Heidari Jozam

nr 221
**Wonen: Discoursen, Praktijken, Perspectieven**
Jos Smeets

nr 222
**Personal Control over Indoor Climate in Offices: Impact on Comfort, Health and Productivity**
Atze Christiaan Boerstra

nr 223
**Personalized Route Finding in Multimodal Transportation Networks**
Jianwe Zhang

nr 224
**The Design of an Adaptive Healing Room for Stroke Patients**
Elke Daemen

nr 225
**Experimental and Numerical Analysis of Climate Change Induced Risks to Historic Buildings and Collections**
Zara Huijbregts

nr 226
**Wind Flow Modeling in Urban Areas Through Experimental and Numerical Techniques**
Alessio Ricci

nr 227
**Clever Climate Control for Culture: Energy Efficient Indoor Climate Control Strategies for Museums Respecting Collection Preservation and Thermal Comfort of Visitors**
Rick Kramer

nr 228
**Fatigue Life Estimation of Metal Structures Based on Damage Modeling**
Sarmediran Silitonga

nr 229
**A multi-agents and occupancy based strategy for energy management and process control on the room-level**
Timilehin Moses Labeodan

nr 230
**Environmental assessment of Building Integrated Photovoltaics: Numerical and Experimental Carrying Capacity Based Approach**
Michiel Ritzen

nr 231
**Performance of Admixture and Secondary Minerals in Alkali Activated Concrete: Sustaining a Concrete Future**
Arno Keulen

nr 232
**World Heritage Cities and Sustainable Urban Development:**
**Bridging Global and Local Levels in Monitoring the Sustainable Urban Development of World Heritage Cities**
Paloma C. Guzman Molina

nr 233
**Stage Acoustics and Sound Exposure in Performance and Rehearsal Spaces for Orchestras:**
**Methods for Physical Measurements**
Remy Wenmaekers

nr 234
**Municipal Solid Waste Incineration (MSWI) Bottom Ash:**
**From Waste to Value Characterization, Treatments and Application**
Pei Tang

nr 235
**Large Eddy Simulations Applied to Wind Loading and Pollutant Dispersion**
Mattia Ricci

nr 236
**Alkali Activated Slag-Fly Ash Binders:**
**Design, Modeling and Application**
Xu Gao

nr 237
**Sodium Carbonate Activated Slag:**
**Reaction Analysis, Microstructural Modification & Engineering Application**
Bo Yuan

nr 238
**Shopping Behavior in Malls**
Widiyani

nr 239
**Smart Grid-Building Energy Interactions:**
**Demand Side Power Flexibility in Office Buildings**
Kennedy Otieno Aduda

nr 240
**Modeling Taxis Dynamic Behavior in Uncertain Urban Environments**
Zheng Zhong

nr 241
**Gap-Theoretical Analyses of Residential Satisfaction and Intention to Move**
Wen Jiang

nr 242
**Travel Satisfaction and Subjective Well-Being:**
**A Behavioral Modeling Perspective**
Yanan Gao

nr 243
**Building Energy Modelling to Support the Commissioning of Holistic Data Centre Operation**
Vojtech Zavrel

nr 244
**Regret-Based Travel Behavior Modeling:**
**An Extended Framework**
Sunghoon Jang

nr 245
**Towards Robust Low-Energy Houses:**
**A Computational Approach for Performance Robustness Assessment using Scenario Analysis**
Rajesh Reddy Kotireddy

nr 246
**Development of sustainable and functionalized inorganic binder-biofiber composites**
Guillaume Doudart de la Grée

nr 247
**A Multiscale Analysis of the Urban Heat Island Effect: From City Averaged Temperatures to the Energy Demand of Individual Buildings**
Yasin Toparlar

nr 248
**Design Method for Adaptive Daylight Systems for buildings covered by large (span) roofs**
Florian Heinzelmann

nr 249
**Hardening, high-temperature resistance and acid resistance of one-part geopolymers**
Patrick Sturm

nr 250
**Effects of the built environment on dynamic repertoires of activity-travel behaviour**
Aida Pontes de Aquino

nr 251
**Modeling for auralization of urban environments: Incorporation of directivity in sound propagation and analysis of a framework for auralizing a car pass-by**
Fotis Georgiou

nr 252
**Wind Loads on Heliostats and Photovoltaic Trackers**
Andreas Pfahl

nr 253
**Approaches for computational performance optimization of innovative adaptive façade concepts**
Roel Loonen